LATVIAN JOURNAL of PHYSICS and TECHNICAL SCIENCES

ISSN 0868 - 8257

4

(Vol. 61)

2024

CONTENTS

LATVIAN JOURNAL of PHYSICS and TECHNICAL SCIENCES

LATVIJAS FIZIKAS un TEHNISKO ZINĀTŅU ŽURNĀLS

Published six times a year since February 1964
Iznāk sešas reizes gadā kopš 1964. gada februāra

4 (Vol. 61) • 2024

RĪGA

Language Editor: O. Ivanova
Computer Designer: I. Begicevs

INDEXED (PUBLISHED) IN

www.scopus.com
www.sciendo.com
EBSCO (Academic Search Complete, www.epnet.com), INSPEC (www.iee.org.com).
VINITI (www.viniti.ru), Begell House Inc/ (EDC, www.edata-center.com).

Issuers: Institute of Physical Energetics,
Institute of Solid State Physics, University of Latvia
Registration Certificate Number: 000700221

Editorial Contacts:
14 Dzerbenes Street, Riga, LV-1006
LATVIA
tel: +371 26245896
M: +371 29363105
leo@lza.lv

sciendo

LATVIAN JOURNAL OF PHYSICS
AND TECHNICAL SCIENCES
2024, N 4

DOI: 10.2478/lpts-2024-0024

IMPLEMENTATION OF CLASSICAL MOTION CUEING ALGORITHMS FOR SERIAL MANIPULATOR BASED MOTION SIMULATOR: LARRMOS CASE STUDY

A. Stupans*, P. Maksimkins, A. Senfelds, L. Ribickis

Riga Technical University,
Institute of Industrial Electronics, Electrical Engineering and Energy,
12-1 Azenes Str., Riga, LV-1048, LATVIA
*e-mail: andrejs.stupans@rtu.lv

The study focuses on the development and evaluation of a motion control system for the Large Range Robotic Motion Simulator (LaRRMoS), which is based on a serial manipulator with 6 degrees-of-freedom. Two motion cueing algorithms (MCAs) – Classical Washout Filter (CWF) and Classical Washout Filter with Cylindrical coordinates (CYL) – are implemented and tested for simulation fidelity and LaRRMoS workspace utilization. CWF and CYL motion cueing performance gets assessed in two use cases: car simulation and luge sports simulation. The car case is a typical driving simulator application. The luge sports case is chosen for its high dynamics to assess the limits of the robot and motion cueing. Though this study uses a pre-recorded set of motion data and runs simulations in non-interactive mode, it aims for real-time interactive simulation for LaRRMoS in the future, so only MCAs capable of real-time operation are inspected. Conducted tests show that the CYL algorithm provides superior performance in highly dynamic motion replication, particularly in lateral accelerations.

Keywords: *Control, cueing, motion, robotics, simulation, serial manipulator.*

1. INTRODUCTION

Motion simulators have broad use nowadays. Simulators are used for pilot/driver training [1], entertainment, and research [2], [3]. According to the application, simulators have different control systems and motion platform types, they vary in fidelity level, motion capabilities, immersivity and operation costs [4], [5]. The equipment used in

simulators depends on its application. Pilot training simulators prioritize their ability to simulate special forces with great precision compared to real aircraft to better train pilots' situation awareness in highly controlled and safe environments. However, such precision may not be needed for the entertainment industry, where the motion of the simulator and the simulated vehicle is optimized for maximizing the user's positive experience and can be far from reality. Simulators used for research can be optimized for motion fidelity, immersivity or both according to the aim of the research.

Motion control system for simulators consists of the following main parts: Simulated vehicle dynamics, motion cueing algorithms (MCA), inverse kinematics (IK) solver, and motion platform controller. Safety mechanisms can be integrated into each part of the motion control system. Figure 1 shows the diagram with a general approach to motion control systems for simulators, but every implementation can have its own specific system architecture.

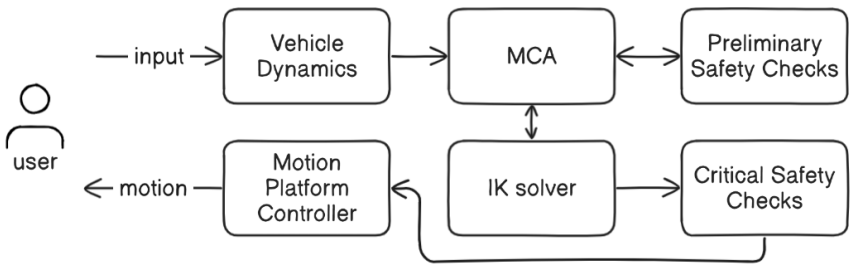

Fig. 1. General architecture of motion simulator control system.

Motion control system highly depends on the motion platform type. Stewart platform is a popular parallel-type manipulator [6]. Its main features are rigidity, precision, and dynamics [7], [8]. However, the Stewart platform is very limited in translational and rotational motion compared to serial manipulators [9]. A significantly bigger range of motion provided by serial manipulators may be more beneficial for motion simulator applications than high precision and dynamics. The hybrid-type motion platforms have the advantages of both parallel and serial manipulators, but they are of significantly increased complexity [4] and incur costs. Hybrid manipulators can have more than six degrees of freedom (DOF). Based on how much DOF a platform has, the complexity of the control system varies significantly. Advanced simulators usually have 6 DOF or more, as the motion of a body in 3D space can be fully defined with 6 DOF [4].

The aim of the research is to design a motion control system suited for a 6 DOF serial manipulator motion platform measured in terms of motion simulation fidelity and the platform workspace usage. The motion control system was tested by simulating two cases – car simulation and luge sports simulation. This study uses pre-recorded vehicle data for non-interactive simulation. The interactive simulation requires a mathematical model of vehicle dynamics that is not in the scope of the study. However, motion control system is developed to be capable of real-time closed-loop interactive simulation in the future. Motion data for both cases were recorded by a custom motion data acquisition system developed specifically to use in conjunction with the motion platform.

2. MATERIALS AND METHODS

For this study, Large Range Robotic Motion Simulator (LaRRMoS) was used as a motion platform. LaRRMoS (Fig. 2) is based on a KUKA KR600 R2830 industrial robot, equipped with a passenger cabin and all the required safety measures to carry a passenger. The control system consists of an Operator PC that runs MCA in Matlab Simulink and inverse kinematics solver in a separate process. The second PC named BEC Controller ensures that all safety systems (garage doors, motion sensors, cabin lock, and safety belt) are working properly. This functionality is provided by BEC GmbH. The Kuka KRC4 controller receives the robot position and implements the motion. Also, critical safety mechanisms are run in KRC4 via Kuka.SafeOperation. The architecture of the LaRRMoS control system used in the study is shown in Fig. 3.

Fig. 2. LaRRMoS motion platform.

The testing of the developed control system was divided into several steps. First, to generate vehicle dynamics, a body motion acquisition system was developed. Then vehicle dynamics were recorded for driving simulation and luge sport simulation. Next, two MCA algorithms were tested on LaRRMoS for both cases. The luge simulation case was chosen for extreme dynamics of motion with fast-changing orientation and high acceleration values. The car simulation was chosen as a reference to evaluate LaRRMoS performance in a typical driving simulation application. The precision of generated specific forces and the motion platform effective workspace usage were evaluated.

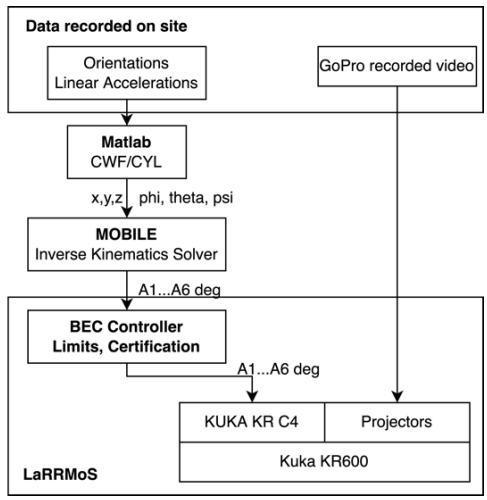

Fig. 3. LaRRMoS control system architecture used in the study.

3. VEHICLE DYNAMICS

To simulate a vehicle, its motion parameters have to be obtained first. There are multiple ways of obtaining the data. One could either develop a mathematical model of the vehicle and use the data generated by this model or obtain motion data directly from the real vehicle.

The first option can be done in game engines like Unity or Unreal using a built-in physics engine. This comes with the benefit of being integrated with advanced 3D graphics and tools for creating a virtual environment that will be used for the visual and audial part of the simulator. However, game engines are optimized for performance, and can be imprecise in physics simulations because of non-deterministic calculations as stated by [10]. The advanced simulators usually have their own mathematical model of the vehicle (e.g., DLR flight simulator by [11]) achieving high precision when simulating motion. However, this approach is a complex task on its own, developing a physics engine from scratch. There is a solution in between, using an advanced physics model as a game engine add-on, like Vehicle Physics Pro in Unity as performed in [12].

To avoid the complexity of developing and verifying the vehicle dynamic model for the time being, the second option was chosen to obtain motion data directly from a real vehicle. It goes with the disadvantage of being able to run only non-interactive simulations, where the user does not have control of a vehicle. In contrast, interactive simulation allows the user to control the simulated vehicle. To obtain vehicle motion data, it was chosen to use the custom motion parameter acquisition system proposed in [13]. This system has been developed to be a source of reliable motion data for motion cueing algorithm input.

3.1. Car Dynamics

In the case of car simulation, the physical parameters of the car should be considered. When undergoing the curve car suspension reacts to the shifting centre of mass, the car rolls to the outside of the curve, and the gravity vector generates interference on the Y-axis measured acceleration as shown in Fig. 4.

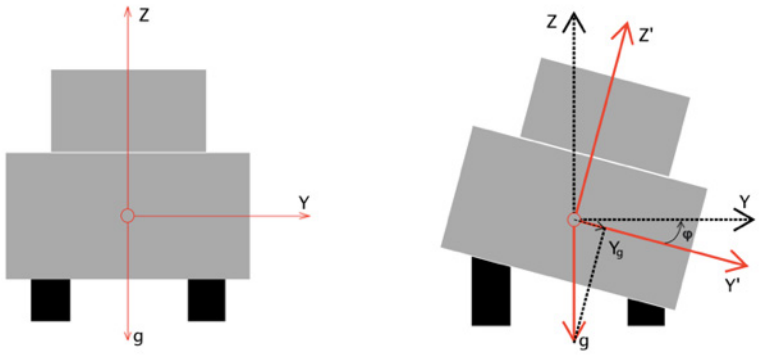

Fig. 4. Gravity vector interference during the car's turning manoeuvre [13].

The motion cueing algorithm demands the data to be free of gravity vector interference. To compensate for the gravity interference formula (1) is used:

$$\vec{a}_{compensated} = \frac{\vec{a}_{measured} - 9{,}81 * \sin(\varphi)}{\cos(\varphi)}. \quad (1)$$

To verify the proposed compensation method, the S-curve manoeuvre (also known as the reverse curve) was chosen as a test procedure shown in Fig. 5. The speed of the car was kept constant during the curve at 15 km/h. Since the velocity of the car is constant, the X-axis acceleration can be neglected. The radius of the curve was measured as 7 meters and the theoretical maximal Y-axis acceleration was calculated as $\vec{a}_{theoretical}$ using formula (2):

$$\vec{a}_{theoretical} = \frac{v^2}{R}. \quad (2)$$

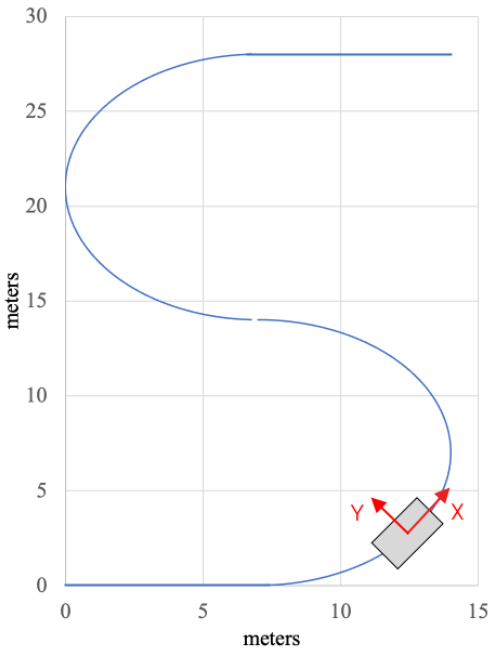

Fig. 5. S-curve manoeuvre for obtaining car dynamics [14].

3.2. Luge Dynamics

The second case is luge sports simulation. The methodology for motion data recording is kept the same as with the car simulation case. Bobsleigh track located in Sigulda, Latvia, was chosen. Its length is 1420 m and it consists of 16 curves. Athletes can reach up to 125 km/h during the track trial. Several track trials were made with the help of a skilled athlete and IMU data were recorded. GPS data was not obtained as the metal roofing of the track shielded the signal.

4. MOTION CUEING ALGORITHM

The motion cueing algorithm (MCA) transforms the simulated vehicle's motion cues into simulator motion cues. The motion of the simulator is limited in terms of workspace, speed and acceleration leading to the inability to simply replicate motions of the simulated vehicle precisely. However, it is possible to produce motion cues that are perceived by a user as real ones while operating within the motion platform limits. The method is based on features of human motion perception. A human could not distinguish a force induced by vehicle acceleration from a force induced by gravity without visual cues [15]. A human feels a specific force that is defined by formula (3). In the motion simulation context, the term specific force is often used to describe forces acting on an object excluding gravity force.

$$SF = \frac{F}{m} = a - g. \quad (3)$$

To simulate the specific force of the vehicle, the motion of a simulated vehicle is divided into three channels: Translation, Tilt Coordination and Rotation. The Translation channel simulates only high-frequency vehicle motion using short translational motion of the platform. The Tilt Coordination channel uses a slight tilt of the cabin to trick the driver's perception into feeling part of gravitational acceleration as a vehicle acceleration [16]. It produces a low-frequency part of a specific force that could not be simulated by the Translation channel. The rotation channel simulates angular speed using short rotations of the cabin. Tilt angles and rotation angles are summed up to get the final rotation of a motion platform. This approach allows to simulate specific forces of a vehicle.

The most widely used motion cueing algorithm is the Classical Washout Filter (CWF) proposed by [17]. Figure 6 shows a diagram of the CWF algorithm. The input of the filter is the simulated vehicle's linear acceleration and angular velocity ω_{IN}. Output is displacement S and tilt angles β of the motion platform end-effector. Rotation matrix ${}^{O}R_{S}$ transforms accelerations from the end-effector's reference frame to the robot base frame. Formulas for high-pass and low-pass filters are provided in [17]. Tilt coordination block transforms low-frequency accelerations into Euler angles using formula (4). Then rate of change of tilt angles is limited to prevent false rotation cues for dynamic motions. However, the limit values suggested by the [18] are for flight simulation, and this study focuses on driving and sports simulation, so the influence of the rate limiter block is also evaluated in the scope of the paper. The study [19] also states that Tilt Coordination without a rate-limiter can be acceptable for a highly dynamic Formula 1 simulator:

$$\beta_T = \begin{bmatrix} 0 & 1/g & 0 \\ -1/g & 0 & 0 \\ 0 & 0 & 0 \end{bmatrix} \cdot \begin{bmatrix} a_x \\ a_y \\ a_z \end{bmatrix}. \tag{4}$$

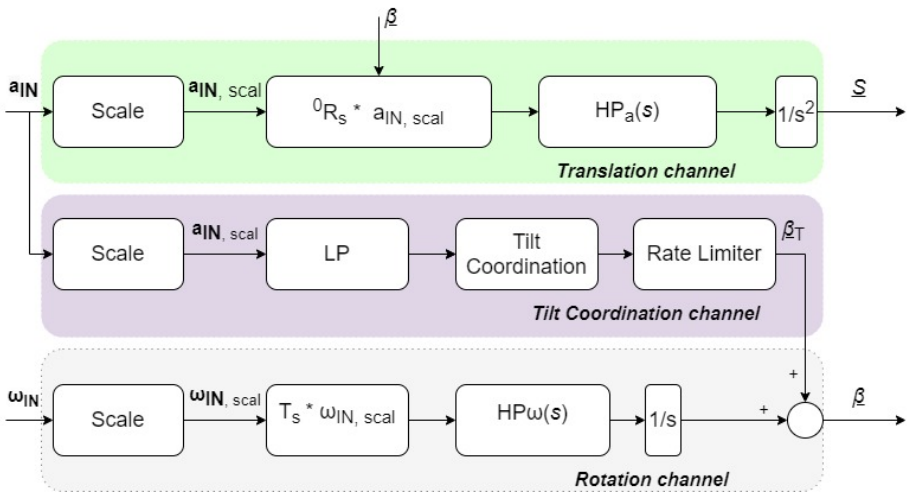

Fig. 6. Classical Washout filter (CWF) diagram [14].

CWF algorithm is simple to implement and computationally fast. However, it was designed for Stewart platform-based simulators. Therefore, it does not fit well for LaRRMoS, utilizing only a small fraction of the available workspace. To improve the effective workspace of the simulator, the CYL algorithm was implemented. The CYL

is a modified version of CWF that operates within a cylindrical coordinate system instead of a Cartesian one. The lateral motion of CWF is represented by rotational motion in CYL as shown in Fig. 7, greatly increasing the effective workspace of the simulator.

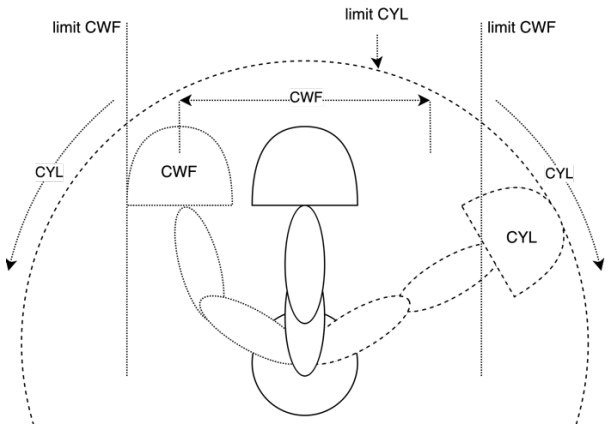

Fig. 7. Motion limits of the LaRRMoS using CWF and CYL algorithms [20].

The paper [14] describes the implementation of the CYL algorithm, suggested by [19], in LaRRMoS. Figure 8 shows a diagram of the CYL algorithm. To get cylindrical coordinates $\ddot{\xi}$ from Cartesian a_{IN}, a transformation matrix $C(\xi)$ is used with formula (5). Additional washout frame ${}^{W}R_S$ is introduced so that the axis of the gondola is always oriented with the axis of the washout filter. Besides operating in the cylindrical coordinate system, the new inertial compensation block is added. It is needed to compensate for centrifugal and Coriolis forces occurring during rotation around the A1 axis of the robot.

$$\ddot{\xi} = \begin{bmatrix} R \\ \alpha \\ Z \end{bmatrix} = C(\xi) \cdot \begin{bmatrix} a_x \\ a_y \\ a_z \end{bmatrix} = \begin{bmatrix} 1 & 0 & 0 \\ 0 & \frac{1}{R} & 0 \\ 0 & 0 & 1 \end{bmatrix} \cdot \begin{bmatrix} a_x \\ a_y \\ a_z \end{bmatrix} \quad (5)$$

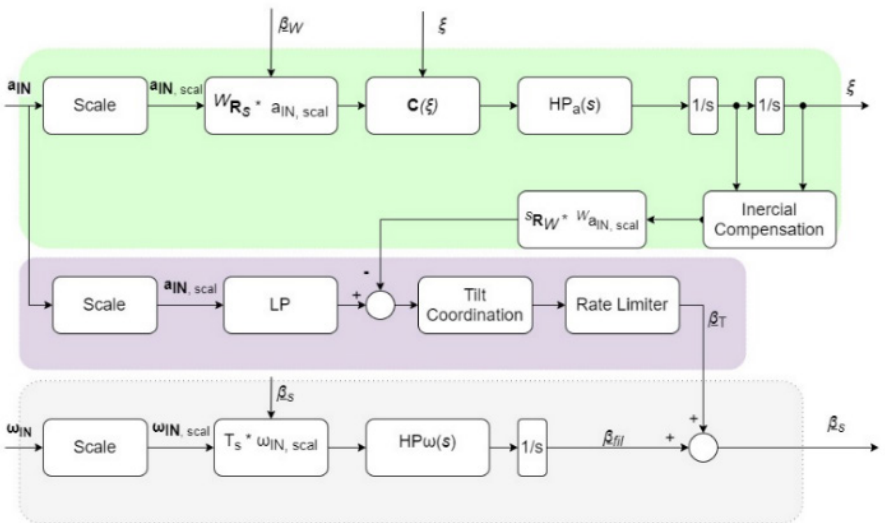

Fig. 8. Diagram of CYL algorithm [14].

There are MCAs that can achieve much better fidelity than CWF in simulating specific forces like model predictive control [21], [22], optimal [23], adaptive [24] and neural network-based [25]. However, most of them are computationally heavy, too slow or require complete knowledge of the future as stated in [26]. Though this study uses a pre-recorded set of motion data and runs simulations in non-interactive mode, it aims for real-time interactive simulation for LaRRMoS in the future, so only MCAs capable of real-time operation are inspected. Tuned parameters for CWF and CYL are presented in Table 1. The tuning process is described in detail in [14].

Table 1. Tuned Parameters for CWF and CYL Algorithms [20]

Parameter	CWF	CYL
Translation channel		
k_x	0.2	0.2
k_y	0.2	1.1
ζ_{HP}	1	1
ω_{nHP}	1	1
ω_b	1	1
Tilt Coordination		
k_{TCx}	0.5	0.5
k_{TCy}	1	1
ζ_{LP}	1.5	1.5
ω_{nLP}	8	8
Rotation channel		
k_{ROTx}	0.5	0.5
k_{ROTy}	1	1

5. TESTING METHODOLOGY

Both CWF and CYL algorithms were tested in two cases – car simulation and luge sports simulation. The car case is a typical choice for motion simulation as driving simulators are a common application. The luge sport case is chosen for its high dynamics, large roll, pitch, yaw angles, and rapidly changing accelerations. The assumption is that LaRRMoS is better suited for the simulation of highly dynamic vehicles, i.e., better in terms of motion cueing precision and effective workspace utilization. This assumption is based on research by [19], where Formula 1 simulation was developed for serial manipulator-based motion platform and also research by [27], where the same type of manipulator was used for upset recovery training of the pilots which involved manoeuvres that were not typical of classic flight simulators.

The method for examining the fidelity of the MCAs is based on a comparison of MCA input and output converted into specific forces as shown in Fig. 9. The sensation error is a measure of a user experienced difference between a real vehicle and a simulated one. The output of MCA is the robot end-effector's position and orientation. To compare it with the vehicle acceleration a_{in}, the second-order derivative of position S is calculated resulting in an acceleration a_{out}. However, to get specific force from acceleration a_{out} formula (6) is used as suggested by the [28], where θ and φ are roll and pitch angles of MCA output angles β.

$$SF = \begin{bmatrix} a_{Xout} + g \cdot sin(\theta) \\ a_{Yout} - g \cdot \sin(\varphi)\sin(\theta) \\ a_{Zout} + g \cdot \cos(\varphi)\sin(\theta) \end{bmatrix}. \quad (6)$$

For the luge simulation case, lateral acceleration a_{Yout} is represented by rotational motion, not linear. The formula changes to (7) for Y-axis acceleration, where angular acceleration $\Delta\omega/\Delta t$ of manipulator axis A1 is multiplied by radius R:

$$SF_Y = \frac{\Delta\omega}{\Delta t} \cdot R. \quad (7)$$

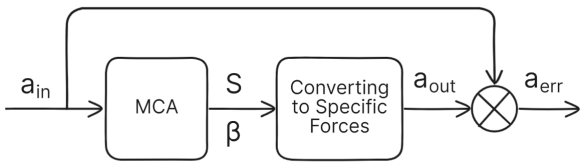

Fig. 9. MCA testing methodology.

6. RESULTS

6.1. Car Simulation Case

While theoretically, the calculated Y-axis acceleration is $2.48\frac{m}{s^2}$, recorded acceleration shows a gradual increase of the Y-axis acceleration up to $3.43\frac{m}{s^2}$, the acceleration increases because of the collapsing suspension (springs, tyres etc.). The difference between theoretical and measured (uncompensated) accelerations is $0.95\frac{m}{s^2}$. This substantial difference is caused by the gravity vector acting on a Y-axis acceleration due to the roll angle reaching up to 7.19°. Compensating Y-axis acceleration taking roll angle into account gives a Y-axis acceleration value of $2.22\frac{m}{s^2}$, thus reducing the error caused by gravity vector interference by 73 %. Additional error could be caused by imprecise measurement of the speed of the car entering the curve since the speed was measured and maintained by the speedometer of the car.

According to the proposed methodology, the output of the MCAs is compared with the car's specific force. The results are shown in Fig. 10 only for lateral acceleration. The output of CWF and CYL algorithms was acquired in two modes – with and without a tilt rate limiter. The error between the simulated acceleration and real vehicle acceleration is much more notable when the tilt rate limiter is used, compared to unrestricted tilt motion. Even without the tilt rate limiter, the additional error between a vehicle's recorded accelerations and simulated accelerations comes from frequency filter phase delay and tilt coordination angle limit of 30°. Also, an inverse kinematics solver theoretically could introduce additional error due to slight deviations of the robot path from the planned path to avoid singularities. However, in practice, the deviation measured with *Kuka.Trace* functionality was negligible [14].

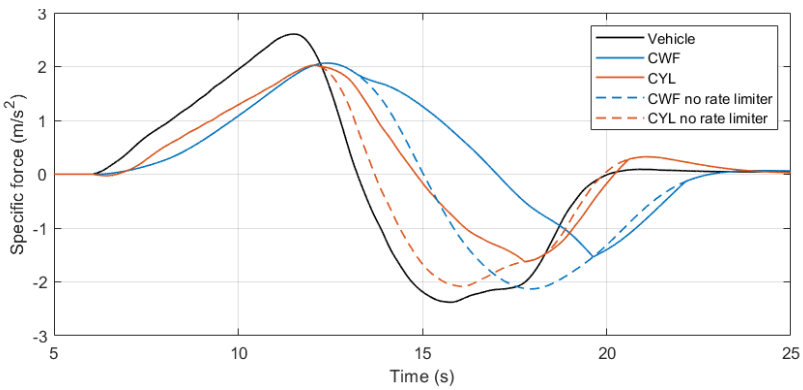

Fig. 10. MCA output compared with MCA input [14].

6.2. Luge Simulation Case

Extensive results for the luge sport case are published in a case study [20]. Recorded accelerations and orientations show high dynamics of the luge. Rapid changes in luge orientation result in both significant translational and angular accelerations. During the lap roll angle reaches $\pm 100\,°$, angular velocity reaches values up to $200\,°/s$, sustained linear accelerations reach values up to $\pm 2\,g$.

The highest accelerations appear on the Z-axis, and they are the most prolonged of all. Z-axis acceleration is a result of a luge sliding on a vertical surface of the track, so the curvature of the track generates acceleration up to $2\,g$ pushing the athlete onto the luge. The second significant acceleration arises on the Y-axis (sideways). While it changes rapidly, it is lower than the Z-axis acceleration and lies within the $\pm 1\,g$ range. The X-axis acceleration is the least aggressive and does not exceed $\pm 0.6\,g$. It appears due to the luge accelerating during straight sections of the track and decelerating on the curves.

For the luge simulation case, accelerations perceived in the simulator are compared with the desired accelerations of the luge in Fig. 11 and Fig. 12 for CWF and CYL, respectively. Target acceleration is the recorded acceleration of the luge used as an input for an MCA. Simulated acceleration is an acceleration perceived by the driver during the simulation. It consists of accelerations produced by the Translation channel (high-frequency component) and by the Tilt Coordination channel (low-frequency component).

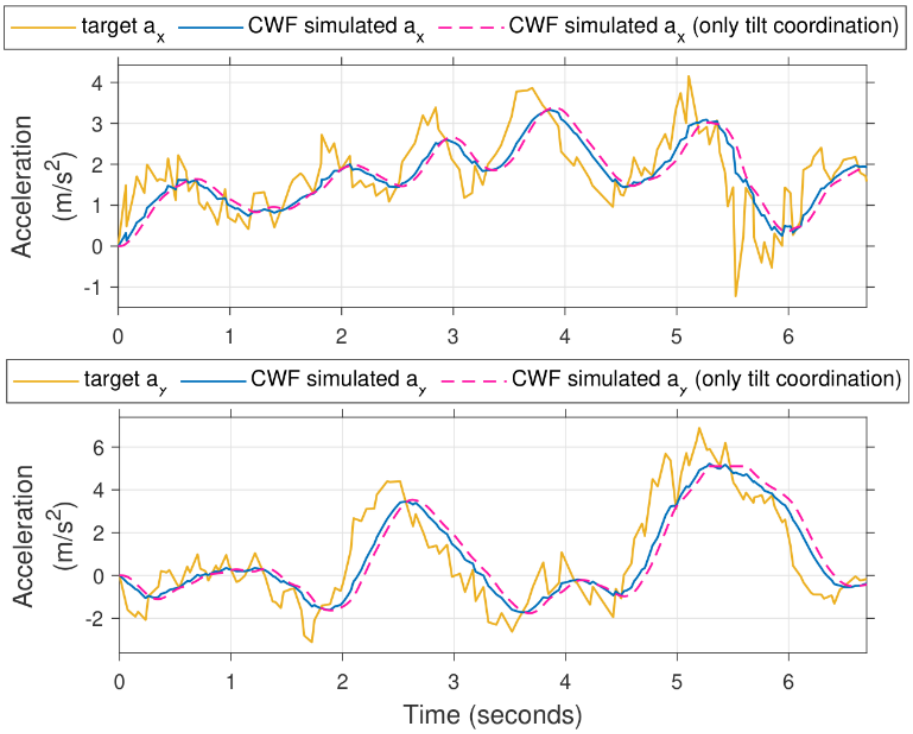

Fig. 11. CWF output compared to the input (target) [20].

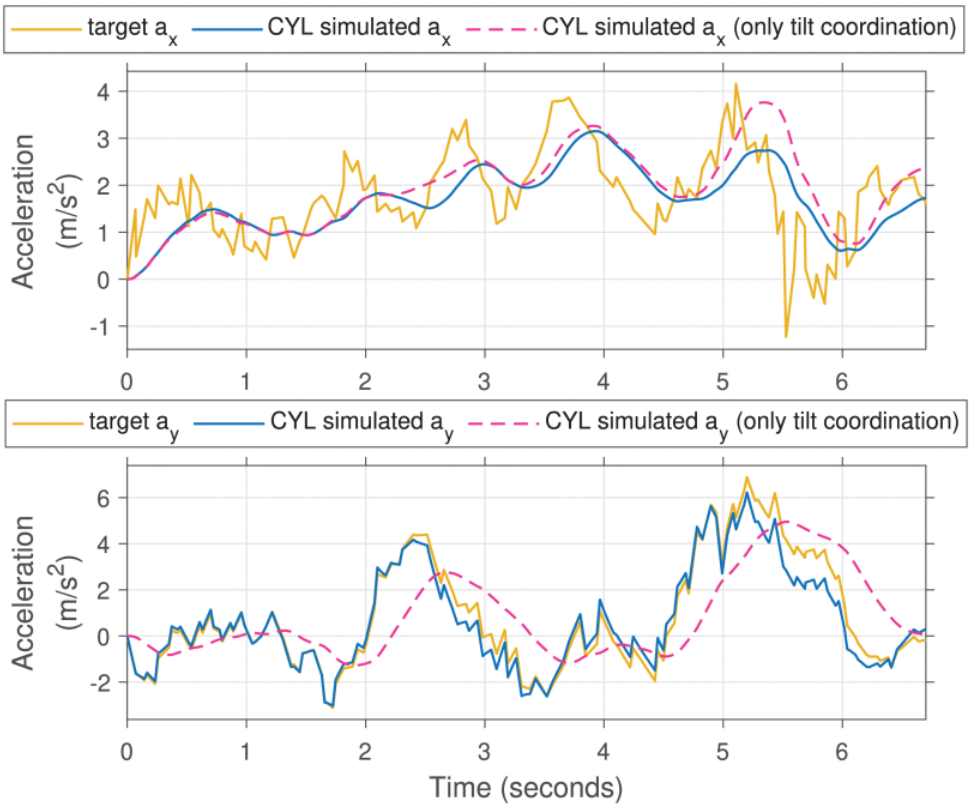

Fig. 12. CYL output compared to the input (target) [20].

In Figs. 11 and 12, the tilt coordination channel output is shown separately without translational channel output to indicate the significance of the high-frequency component. The continuous accelerations can be reproduced only using Tilt Coordination. However, the low-pass filter introduces the delay between the target and simulated acceleration. To compensate for the delay high-frequency acceleration is added. It is clearly visible in Fig. 12 where simulated acceleration matches target acceleration only when both high and low-frequency accelerations are combined.

Both MCAs produce imprecise X-axis acceleration. The reason is a double limitation – Tilt Coordination gain and the Translation channel gain are scaled down due to LaRRMoS physical limitations.

Y-axis acceleration is evidently better reproduced by the CYL algorithm, as it allows for wider and faster lateral movements. However, there are some discrepancies caused by the ±30 ° tilting limit and high-pass and low-pass filters.

7. DISCUSSION

While this paper addresses only motion cueing algorithms and vehicle dynamics acquisition, work on inverse kinematics solver feedback integration into the motion cueing algorithm, and implementation of real-time closed-loop motion control are

being conducted. Further research paper is planned to be published in the near future.

Only CWF and CYL algorithms were considered in the paper due to their computational simplicity and ability to work in real time. However, as the paper [26] states, some limited adaptive optimization can be added to the filter parameters to utilize the workspace of the robot even more efficiently. Introducing optimal filter MCA to the LaRRMoS control system will be investigated further.

Regarding the luge sport case discussed in this paper, obtaining the track geometry is essential to recreate it in a virtual environment for an interactive simulation. This will advance the training experience for athletes, improving their control of the luge during both simulation and real training. To achieve this goal, the GPS-RTK functionality could be added to the motion parameter acquisition system, as it greatly increases positioning precision. However, the lack of a stable GPS signal on a track has to be taken into account.

8. CONCLUSIONS

In this study, a motion control system for Large Range Robotic Motion Simulator has been proposed and tested. The findings prove that this system is effective in replicating provided vehicle-induced specific forces, especially for highly dynamic cases like luge sport. The motion cueing algorithms were tested in non-interactive mode with pre-recorded motion parameters using a body motion acquisition system, however, literature end experimental results show the computational simplicity of the algorithms indicating their ability to work in real-time interactive mode.

The Classical Washout Filter and its modification with the Cylindrical Coordinate System were tested for their motion cueing precision. The CYL algorithm provided better results in terms of utilizing the LaRRMoS workspace, especially for lateral accelerations. The luge simulation case highlighted the effectiveness of CYL compared to the CWF in highly dynamic motion replication. CYL algorithm is considered more effective for applications which tend to simulate more dynamic vehicles, like the luge sports examined in this study. Extrapolating on this assumption, CYL could be effectively used in racing car and motorcycle simulation or other extreme sport application. The CWF remains a viable option for simpler and less dynamic simulations.

Tilt rate limiters significantly increase motion cueing error. Removing the limiters significantly reduces the deviation between the target and simulated specific forces. The primary sources of the error are the delays produced by filtering, tilt coordination angle limits and physical limitations of LaRRMoS. The inverse kinematics solver, though, did not induce a noticeable error for the planned path of robots, thus indicating its high effectiveness in path execution.

REFERENCES

1. Nieuwenhuizen, F., Mulder, M., van Paassen, M., & Bülthoff, H. H. (2011). The Influence of motion system characteristics on pilot control behaviour. In *AIAA Modeling and Simulation Technologies Conference*, (pp. 1–15), 8–11 August 2011. Portland, Oregon, American Institute of Aeronautics and Astronautics.

2. Mohajer, N., Abdi, H., Nelson, K., & Nahavandi, S. (2015). Vehicle Motion Simulators, a Key Step towards Road Vehicle Dynamics Improvement. *Veh Syst Dyn, 53*, 1204–1226.
3. Caffò, A.O., Tinella, L., Lopez, A., Spano, G., Massaro, Y., Lisi, A., … & Bosco, A. (2020). The Drives for Driving Simulation: A Scientometric Analysis and a Selective Review of Reviews on Simulated Driving Research. *Front Psychol., 11*, 917.
4. Ghafarian, M., Watson, M., Mohajer, N., Nahavandi, D., Kebria, P.M., & Mohamed, S. M. (2023). A Review of Dynamic Vehicular Motion Simulators: Systems and Algorithms. *IEEE Access, 11*, 36331–36348.
5. Wynne, R.A., Beanland, V., & Salmon, P.M. (2019). Systematic Review of Driving Simulator Validation Studies, *Saf. Sci., 117*, 138–151.
6. Stewart, D. (1965). A Platform with Six Degrees of Freedom. *Proc. Inst. Mech. Eng., 180*, 371–386.
7. Mamoon, M., & Saifullah. (2014). Inverse kinematics and path planning of Stewart Platform using crank arm actuation system. In *Proceedings of 2014 11th International Bhurban Conference on Applied Sciences & Technology (IBCAST),* (pp. 175–181), 14–18 January 2014. Islamabad, Pakistan.
8. Khamsehei Fadaei, M.H., Hamzeh Pahnehkolaei, S.A., Hesarlou, M.J., & Torkan, Z. (2017). Dynamics modeling of a stewart platform in Simulink MSC ADAMS. In *2017 IEEE 4th International Conference on Knowledge-Based Engineering and Innovation (KBEI)*, (pp. 0294–0298).
9. Sharma, K., Haddadin, S., Minning, S., Heindl, J., Bellmann, T., Parusel, S., … & Albu-Schaeffer, A. (2013). Evaluation of human safety in the DLR Robotic Motion Simulator using a crash test dummy. In *2013 IEEE International Conference on Robotics and Automation*, 205–212.
10. Chance, G., Ghobrial, A., McAreavey, K., Pipe, T., & Lemaignan, S. (2022). On Determinism of Game Engines Used for Simulation-Based Autonomous Vehicle Verification. *IEEE Trans. Intell. Transp. Syst., 23*, 20538–20552.
11. Seefried, A., Pollok, A., Kuchar, R., Hellerer, M., Leitner, M., Schallert, C., … & Looye, G. (2019) Multi-Domain Flight Simulation with the DLR Robotic Motion Simulator. *2019 Spring Simulation Conference (SpringSim)*, 1–12.
12. Rassõlkin, A., Maksimkins, P., Stupāns, A., Rjabtšikov, V., Šenfelds, A., & Kuts, V. (2024). The Spatial Representation of a Self-Driving Vehicle for the Virtual Entity of a Digital Twin. *Computer, 57*, 58–66.
13. Maksimkins, P., Šenfelds, A., Maksimkina, J., & Ribickis, L. (2021). Development of a New Body Motion Parameters Acquisition System. In *2020 IEEE 8th Workshop on Advances in Information, Electronic and Electrical Engineering (AIEEE)*, (pp. 103–107), 22–24 April 2020. Vilnius, Lithuania.
14. Maksimkins, P., Stupāns, A., Kriviša, S., Šenfelds, A., & Ribickis, L. (2021). Implementation of a classic washout filter for robotic large range motion simulator using cylindrical coordinate system. *2021 IEEE 9th Workshop on Advances in Information, Electronic and Electrical Engineering (AIEEE)*, (pp. 1–6), 25–26 November 2021. Riga, Latvia.
15. Correia Grácio, B.J. (2013). *The Effects of Specific Force on Self-Motion Perception in a Simulation Environment.* PhD Thesis. TU Delft Repository.
16. Stahl, K., Leimbach, K.-D., Zoellner, R. D., & Meroth, A. (2015). A Washout and a Tilt Coordination Algorithm for a Hexapod Platform. *2015 IEEE 18th International Conference on Intelligent Transportation Systems*, 1196–1201.
17. Nahon, M.A., & Reid, L.D. (1990). Simulator Motion-Drive Algorithms - A Designer's Perspective. *J. Guid. Control Dyn., 13*, 356–362.
18. Reid, L., & Nahon, M. (1987). The Response of Airline Pilots to Flight Simulator Motion. *Flight Simulation Technologies Conference*. American Institute of Aeronautics and Astronautics.
19. Robuffo Giordano, P, Masone, C., Tesch, J., & Breidt, M. (2010). A Novel Framework for Closed-Loop Robotic Motion Simulation - Part II: Motion Cueing Design

and Experimental Validation. *2010 IEEE International Conference on Robotics and Automation*, 3896–3903.

20. Stupāns, A., Maksimkins, P., Šenfelds, A., & Ribickis, L. (2023). Analysis of motion cueing performance of large range robotic motion simulator: A luge sports simulator case study. In *2023 IEEE 17th International Conference on Compatibility, Power Electronics and Power Engineering (CPE-POWERENG)*, (pp. 1–6), 14–16 June 2023. Tallinn, Estonia.
21. Chalak Qazani, M.R., Asadi, H., & Nahavandi, S. (2019). A Decoupled Linear Model Predictive Control-based Motion Cueing Algorithm for Simulation-based Motion Platform with Limited Workspace. *2019 IEEE International Conference on Industrial Technology (ICIT)*, 35–41.
22. Augusto, B., & Loureiro, R. (2009). *Motion Cueing in the Chalmers Driving Simulator: A Model Predictive Control Approach.* Chalmers University of Technology. Available at https://publications.lib.chalmers.se/records/fulltext/98871.pdf
23. Chen, S.-H., & Fu, L.-C. (2010). An optimal washout filter design for a motion platform with senseless and angular scaling maneuvers. In *Proceedings of the 2010 American Control Conference*, (pp. 4295–4300). Baltimore, MD, IEEE.
24. Miunske, T., Holzapfel, C., Baumgartner, E., & Reuss, H.-C. (2019). A new approach for an adaptive linear quadratic regulated motion cueing algorithm for an 8 DoF full motion driving simulator. In *2019 International Conference on Robotics and Automation (ICRA)*, (pp. 497–503), 20–24 May 2019. Montreal, Canada.
25. Koyuncu, A.B., Erçelik, E., Comulada-Simpson, E., Venrooij, J., Kaboli, M., & Knoll, A. (2020). A novel approach to neural network-based motion cueing algorithm for a driving simulator. In *2020 IEEE Intelligent Vehicles Symposium (IV)*, (pp. 2118–2125), 20–23 October 2020. Las Vegas, USA.
26. Pham, D.A., Röttgermann, S., Flores, F.G., & Kecskemethy, A. (2015). Optimal motion cueing algorithm selection and parameter tuning for sickness-free robocoaster ride simulations. In B. Corves, E.-C. Lovasz, & M. Hüsing (Eds.), *Mechanisms, Transmissions and Applications* (pp. 127–135). Cham, Springer International Publishing.
27. Nie, Y., Bellmann, T., Seefried, A., Looye, G., Van Kampen, E.-J., & Chu, Q.P. (2015). Aircraft upset and recovery simulation with the DLR robot motion simulator. In *AIAA Modeling and Simulation Technologies Conference*, (pp. 1–10), 5–9 January 2015. Florida, American Institute of Aeronautics and Astronautics.
28. Kim, M.S., Moon, Y.G., Kim, G.D., & Lee, M.C. (2010). Partial Range Scaling Method Based Washout Algorithm for a Vehicle Driving Simulator and its Evaluation. *Int. J. Automot. Technol., 11*, 269–275.

sciendo

LATVIAN JOURNAL OF PHYSICS
AND TECHNICAL SCIENCES
2024, N 4

DOI: 10.2478/lpts-2024-0025

SMART GRID STANDARDISATION: CONTRIBUTIONS AND OPPORTUNITIES OF EU HORIZON 2020 PROJECTS

A. Mutule[1*], I. Antoskova[1], P. Carroll[2], C. Papadimitriou[3],
A. Morch[4], V. Efthymiou[5]

[1]Smart Grid Research Centre, Institute of Physical Energetics
14 Dzērbenes Str., Riga, LV-1048, LATVIA
[2] Management Information Systems Department, University College Dublin
Belfield, Dublin 4, D04 C1P1, IRELAND
[3] Electrical Engineering Department, Eindhoven University of Technology
5600 MB Eindhoven, THE NETHERLANDS
[4] Energy Systems Department, SINTEF Energy Research
Sem Sælands vei 11, 7034 Trondheim, NORWAY
[5] FOSS Research Centre for Sustainable Energy, University of Cyprus
1678 Nicosia, CYPRUS
*e-mail: amutule@edi.lv

Standards are critically important for smartening the grid because they affect the interoperability, compatibility, efficiency, and realisation of new technologies and services. In this paper we assess the contribution of EU funded Horizon 2020 projects to adapting or initiating new Smart Grid standards. We provide a comprehensive overview of the Smart Grid standardisation ecosystem and identify opportunities for researchers and innovators to participate in standardisation activities. We identify 225 Horizon 2020 Smart Grid projects and explore which have contributed to the creation or revision of Smart Grid standards. We identify the type of standardisation activities undertaken and explore the factors that influence engagement. We have found that 21 % of EU Horizon 2020 Smart Grid projects engage in some level of standardisation activities. Of these projects the majority (60 %) are involved in understanding standards, 31 % actively engage in influencing standards, while 8 % successfully participate in elaborating new standards. Our study demonstrates that despite the complexity of the Smart Grid Standardisation ecosystem, EU funded researchers and innovators play an important role in the standardisation process.

Keywords: *CENELEC, European projects, H2020, IEC, Research & Innovation, Smart Grids, standards, standardisation, standardisation ecosystem.*

1. INTRODUCTION

Climate change and the need for urgent decarbonisation of power systems in Europe and other countries around the world motivate efforts to transform energy grids into Smart Grids (SG). This transformation process must address multiple challenges, e.g., increasing electricity demand from the electrification of heat and transport, energy price escalation, electricity reliability concerns, and the wide deployment of intermittent distributed renewable energy resources (RES). The development and deployment of Smart Grids around the world is at different stages. However, many countries face a common problem – the lack of standardisation – as seen in [1] and [2].

There has been an increased recognition that more attention needs to be paid to standardisation issues. The importance of standards is emphasised by the recent Pan-European political ambitions stated in the European Green Deal [3] aiming to achieve climate neutrality by 2050 and the preceding "Clean Energy for all Europeans Package" (CEP) which pursues the goals of improving energy efficiency and locating citizens at the centre of the energy transition process [4]. In addition, sector integration [5] strategy emphasises the important directions in the green energy transition, including standardisation and market uptake of sustainable technologies and solutions across different industry sectors. In this light, interoperability becomes a necessary capability of networks and devices so that they can communicate, make sense of information, and react accordingly [6], [7]. In addition, standards developers face a challenge to be technology neutral and find a balance between setting requirements for specific technologies and keeping consistency in requirements across technologies [8].

The revised TEN-E Regulation [9] defines a Smart Grid as "an electricity network, including on islands that are not interconnected or not sufficiently connected to the trans-European energy networks, that enables cost-efficient integration and active control of the behaviour and actions of all users connected to it, including generators, consumers and prosumers, in order to ensure an economically efficient and sustainable power system with low losses and a high level of integration of renewable sources, of security of supply and of safety, and in which the grid operator can digitally monitor the actions of the users connected to it, and information and communication technologies for communicating with related grid operators, generators, energy storage facilities, and consumers or prosumers, with a view to transmitting and distributing electricity in a sustainable, cost-efficient and secure way". It extends the definition provided in the TEN-E regulation of 2013 [10] and highlights the importance of Information and Communication Technologies (ICTs) in managing the complex and dynamic nature of the electricity grid, especially in an environment that involves a high level of integration of RES.

As Smart Grids rely heavily on the use of ICTs, advanced metering infrastructure (AMI) and a huge number of various sensors, data protection and cyber security issues arise [11], [12]. This emphasises the need for standards to ensure energy systems' resilience, robustness and reliability, as well as increasing consumer confidence and acceptance of new technologies, and promoting demand-side services. In this context, Smart Grids can achieve their goals of sustainable and cost-efficient electricity distribution, while ensuring the security and privacy of user data.

Standards can provide a common framework, ensuring that the technologies and systems developed by different producers and

innovators are compatible with each other. Given the range of technologies, producers and innovators involved, communication and cooperation to ensure standards development for efficient integration are vital. This fact is acknowledged by multiple researchers and practitioners, e.g., [6], [8], [13]–[16] and others.

An interesting overview of standardisation activities through the prism of energy system functionalities is provided in [15], concluding that despite significant work within Smart Grid standardisation, more efforts are needed to ensure interoperability and seamless operation of different technologies and sectors. This can be achieved only through cooperation of different stakeholders from policy makers to researchers and industrial players. In addition, [16] uncovers a gap between the conceptual thinking of scientific researchers and the more practical point of view of industry based on real life experience in standards development. Furthermore, three ways (modes) of standardisation are distinguished in [14]: committee-based, market-based and government-based. A multi-mode approach is likely to become increasingly important in the future particularly in developing 'smart' technologies and innovating large-scale complex systems like Smart Grids. In addition, [13] captures the complexity of the standards development environment for Smart Grids in comparison with other emerging technologies considering the multiple actors and layers involved. It emphasises that public sector researchers can make significant contributions to standards development, both at the earliest stages in a technology's maturity and later in the industrial lifecycle. This implies that more attention needs to be paid to involving researchers and innovators in standards development processes, particularly through publicly funded collaborative projects.

Standards serve as the linking connection among researchers, innovators and developers by systemising and disseminating knowledge, and offering validated processes and best practices. As such, standardisation contributes to information sharing and knowledge enhancement and also saves resources. Standardisation promotes also the scalability and replication potential as seen in [17]. By sharing findings, keeping knowledge open to the research and innovation (R&I) community and promoting synergies, standardisation is the key for further development of Smart Grids.

Several studies ([18], [19]) explore the motivation for industrial players to participate in standardisation processes. Firms participating is standardisation may benefit from knowledge sourcing, influencing the regulatory framework, accelerating the route-to-market of innovative products and accordingly increasing performance what is specifically true for manufacturing industries [19]. At the same time, literature [20] highlights that for researchers the main driver is intrinsic motivations and that reputation and financial rewards are not relevant.

European projects are a space where research meets innovation, industry, policy and real-life implementation. Standardisation supports transferring R&I outcomes into practical applications and solutions that can be used by society and industry. The increasing focus of European Framework Programs (Horizon 2020, Horizon Europe) on higher Technology Readiness Levels (TRLs) requires more attention to standardisation efforts for successful commercialisation. However, early evidence [21] suggests that the Program has only made limited progress in this dimension. The untapped potential of pre-normative research in support of standardisation in EU-funded projects is also acknowledged in the new EU Strategy on Standardisation [22]. To address this issue, the Commission has launched the European Standardisation Booster [23] aiming at providing expert services to European

projects to help them increase and valorise project results by contributing to the creation or revision of standards.

The above considerations together highlight an urgent need to investigate how Smart Grid standardisation is addressed in European collaborative R&I projects. This is the research gap addressed in this paper.

The paper focuses on the role of EU R&I projects in Smart Grid standardisation. The contributions of this paper are twofold: firstly, we perform a high-level assessment of standardisation activities in dissemination, exploitation and communication (DEC) strategies of collaborative EU R&I Smart Grid projects; in addition, we estimate the contribution of R&I projects to standardisation. We put forward the following research questions:

1. What is the contribution of EU R&I projects to SG standardisation?
2. In which standardisation activities do collaborative EU R&I projects engage?
3. What are the factors influencing project engagement in standardisation process?

To answer our research questions, we analyse EU funded Smart Grid R&I projects. Our approach is described in detail in the Methodology Section. We then present an overview of the Smart Grid standardisation ecosystem to set the context of our study in Section 3. Results and Analysis are presented in Section 4, and finally conclusions and recommendations are presented in Section 5.

Although there has been significant progress in the development of Smart Grid technologies, standardisation efforts have not kept pace. Public funding plays a vital role in supporting standardisation initiatives. Promoting Standardisation efforts within EU projects, such as Horizon 2020 and Horizon Europe, is of paramount importance. Our study highlights that while there are some positive practices in including standardisation within the scope of R&I projects, there is still a need for further efforts to facilitate the involvement of R&I projects in standardisation.

2. METHODOLOGY

We focus on the Smart Grid domain in a broader understanding of the term, which includes consumer behaviour and social acceptance elements along with technical aspects. This section discusses our methodology to identify different pathways of how R&I projects could be involved in the standardisation process. Furthermore, it presents the sources used for data collection, the categories for classification of projects and limitations of the study.

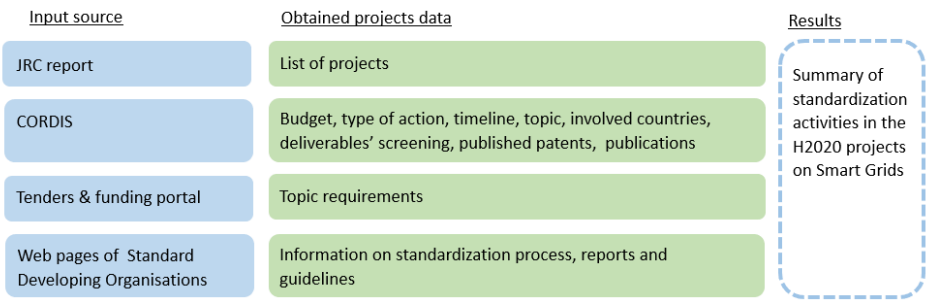

Fig. 1. Data sources used for the study.

Our analyses are based on the selection of Smart Grid projects identified in the Joint Research Centre (JRC) report [24] and complemented by additional data sources, i.e., CORDIS [25], EC Tenders & Funding Portal [26], websites of projects]specific and standardisation bodies (Fig. 1).

The JRC report [24] presents an overview of European R&I projects in the field of Smart Grid funded by the seventh EU framework programme (FP7), Horizon 2020 (H2020) and the competitiveness and innovation framework programme (CIP) in terms of funding, distribution between project domains and participating organisations. Our assessment is limited to projects funded under H2020, the project start date is between 2015 and 2020.

In order to identify projects, which included standardisation activities, we performed a manual check of relevant project results available in the CORDIS database [25] and on project specific web pages. It should be noted that some projects did not have sufficient information published for making conclusions on their activities related to standardisation, because they were at the earlier stages or for other unknown reasons. In these situations, we assumed that there was no link to standardisation activities, as generally projects tended to have references to standardisation in the first two years of project execution timeline if standardisation was a focus or key activity of the project.

To acknowledge the extent to which the projects had addressed standardisation, we defined four levels of possible contribution to standardisation activities and relevant criteria (see Table 1 inspired by [27]–[29].

Table 1. Summary of Criteria Used to Determine Project Level of Contribution to Standardisation

Level	Description	Criteria
n/a	Standardisation activities are not included in the project scope	None of the following criteria are met **or** The publicly available information on project results is insufficient
Level 1	Existing standards screening	A report on relevant standards is publicly available
Level 2	Influence ongoing standardisation	Project results are translated to the relevant TC at European or national level (national mirror group) **or** The project joined a Technical Committee through the project liaison concept **or/and** Project results are considered in standardisation document
Level 3	Elaboration of a new standard	The project initiated the development of a CENELEC Workshop Agreement (CWA) **or** The project proposed a new working item (WI)

Next, we used the EC Tenders & Funding Portal [26] for assessing requirements of relevant calls in terms of references to standardisation and necessary commitment. We anticipated that projects would demonstrate different levels of contribution to standardisation. Therefore, we proposed that the probability of a project being deeply engaged in standardisation work depended on existence of explicit requirements to do so in the relevant call.

Additionally, we gathered information on publications and intellectual property rights applications for all the projects in our selection to have an overview via other DEC options.

Results and analysis are presented in Section 4.

3. REVIEW OF THE SMART GRID STANDARDISATION

In this section, we provide a comprehensive overview of the Smart Grid Standardisation ecosystem and processes to set the context and highlight opportunities for the engagement of researchers and innovators.

3.1. Smart Grid Standardisation Ecosystem

This section highlights the complicated structure and diversity of actors in the Smart Grid Ecosystem. The ecosystem structure influences which activities researchers and innovators may engage in. Some insight into the activities of major players contributing to Smart Grid standards development and its taxonomy is provided below.

Standards are developed by different entities:

- **Formal standards** are developed by officially recognized bodies – formal Standard Developing Organisations (SDOs). Based on Regulation (EU) No 1025/2012 [30], the **European Committee for Standardisation (CEN), the European Committee for Electrotechnical Standardisation (CENELEC)** and the **European Telecommunication Standards Institute (ETSI)** are the three European Standardisation Organisations that are competent in the area of voluntary standardisation for Europe. The international equivalents of CEN and CENELEC are **the International Organization for Standardisation (ISO)** and **the International Electrotechnical Commission (IEC)** respectively. SDOs cooperate on European and global levels, some agreements allow publishing of dual logo standards, e.g., ISO/IEC 14543 series on Information technology – Home electronic system architecture.
- **Informal standards** are developed by various forums and consortia – informal SDOs, many of which are very well known and highly respected, e.g., **Institute of Electrical and Electronics Engineers Standards Association (IEEE SA).** These standards are usually initiated by industries and are based on specific technology and market needs representing probably more dynamic part of standardisation work. These standards are often voluntary and can be further ratified by formal SDOs.
- **Private or industrial standards** (sometimes referred to as proprietary) are developed, maintained and controlled by a licence agreement which is owned by a specific company or groups of companies. Proprietary standards may be free to use, but the file specification is often undisclosed. These standards can be in some cases competitive. Sometimes battles between different technologies result in de-facto standards [14].

In 2009, the European Commission (EC) and the European Free Trade Association (EFTA) mandated **CEN, CENELEC** and **ETSI** with responsibility for the development of an open architecture for utility meters involving communication protocols enabling interoperability (smart metering). In response to this request (M/441[31]), CEN, CENELEC and ETSI established the Coordination Group on Smart Meters (CG-SM). Then, in response to requests issued in March 2011 by the EC and EFTA

to develop standards for Smart Grids under EC mandate M/490 [32], CEN, CENELEC and ETSI established a Smart Grid Coordination Group (SG-CG). SG-CG worked intensively and produced several important reports. An interesting report with quite an impact [33] proposed a widely acknowledged reference architecture for Smart Grids – Smart Grids Architecture Model (SGAM) taking on board the complexity and the different layers of the Smart Grid. The SGAM framework introduced among others interoperability aspects and expanded from technical and component domains to business and ICT domains in a layer-based approach that brings all these together. Also, this entity developed a set of standards [34], supporting the wider adoption of Smart Grids in Europe. Since 2016, the firstly formulated entity changed to Coordination Group on Smart Energy Grids (CG-SEG), which took over and extended the responsibilities [35]. In addition, they have provided standardisation requirements within the framework of adoption of the Clean Energy Package (CEP) [36]. Since 2021, CG-SM was merged in CG-SEG, which continues to advise on European standardisation requirements on Smart Grids and multi-commodity smart metering standardisation, including interactions between commodity systems (e.g., electricity, gas, heat, water).

Multiple **CENELEC** Technical Committees (TCs) develop standards that help energy grids improve their safety, reliability and flexibility. TC 57 "Power systems management and associated information exchange" in collaboration with the IEC TC 57 develops key standards for Smart Grid technologies and their integration with existing power grids. Another example is TC 8X "System aspects of electrical energy supply", which developed EN 50549 series on Requirements for generating plants to be connected in parallel with distribution networks supporting the Commission Regulation 2016/631/EU [37]. These are important standards as they serve as a technical reference for connection agreements between Distribution Grid Operators (DSOs) and electricity producers. Other organisations and their area of focus are summarised in Appendix A.

Several ETSI committees are involved in standards development useful for Smart Grids. With strong support from the Commission and in close interaction with industry [16] ETSI SmartM2M TC has developed and continues to enhance the Smart Applications REFerence (SAREF) ontology, which aims at enabling semantic interoperability between solutions from different providers and within various activity sectors (i.e., energy, environment, building, smart cities, industry and manufacturing, and smart agriculture) in the Internet of Things (IoT).

On a global level, the **IEC** established a System Committee (SyC) for Smart Energy that aims at providing systems level standardisation, coordination and guidance in the areas of Smart Grids and smart energy, including interaction in the areas of heat and gas. The committee has developed and published a Smart Grid Standardisation Roadmap IEC TR 63097 that presents the standardisation requirements of a Smart Grid based on the technologies and systems that are its building blocks. Under this approach, an exhaustive list of standards is developed and they are examined under the prism of the different operations of the Smart Grids.

A number of standards have horizontal effect and are used for all operations and thus considered as core standards (IEC 61850 on power utility automation, IEC 61508 on functional safety of electrical/electronic/programmable electronic safety-related systems, IEC 61970 on common information model (CIM)/energy manage-

ment, IEC 61968 on CIM/distribution management, IEC 62056 on data exchange for meter reading, tariff and load control, IEC 62351 on security, IEC TR 62357 on reference architecture) [38].

Additionally, the IEC moved one step further by providing a visualised Smart Grid Standards map [39]. This is an online user-friendly tool that facilitates the user to spot standards as per the technologies and the different systems as these are represented into the SGAM plane. The IEC works in close collaboration with the ISO through a technical joint committee to develop standards relating to ICT that is catalytic for the Smart Grid.

ISO has set up several TCs to deal with standards that are highly relevant with the Smart Grid standardisation. For example, ISO/TC 205 "Building environment design" works on the standardisation of the holistic assessment of the energy performance of new and existing buildings taking on board also RES, energy efficiency, energy performance and different carriers as well. ISO 17800:2017, developed within this TC, provides the basis for common information exchange between control systems and end use devices. As such, it provides a baseline for energy consumers that supports a wide range of concepts that are foreseen in the Smart Grids such as demand response, load shedding, peak shaving etc.

As already mentioned, standardisation leverages voluntary work coming from the industry sector. As such, different industrial alliances, i.e., informal SDOs, developing standards highly relevant to Smart Grid have been set up. Some of recognised organisations are described further.

The **IEEE SA** is a leading global community that develops standards for different technical systems including Smart Grids. It has developed under this domain more than 100 standards [40], including 10 standards named in the Smart Electric Power Alliance (SEPA) Smart Grid Catalogue of Standards [41], which aims at serving as a useful resource for utilities, manufacturers, regulators, consumers and other stakeholders globally. Among the broad number of systems and technologies addressed by IEEE standards are cyber security (IEEE C37.240, IEEE 1711 series) distributed energy resources (DER) (IEEE 1547 series), Smart Grid interoperability (IEEE 2030 series), substation automation (such as IEEE 1815 on Distributed Network Protocol (DNP3)) and others.

Another well-known association involved in Smart Grid standardisation is the **International Telecommunication Union (ITU)** – the United Nations specialized agency for information and communication technologies (ICTs). Several ITU-T study groups (SGs) are working on Smart Grid related topics and developing international standards known as ITU-T Recommendations in the areas of IoT, Machine-to-Machine (M2M), home energy management systems, smart metering, intelligent transportation systems and others. For example, the ITU-T SG15 "Transport, Access and Home" developed standards on power line communication (ITU-T recommendations G.990x-series), which is one of the most important technologies for Smart Grid.

The Internet Engineering Task Force (IETF) is developing voluntary standards for the Internet that are often adopted by Internet users, network operators, and equipment vendors. IETF RFC 6272-2011 on Internet Protocols for the Smart Grid is listed in [41].

Open Automated Demand Response (OpenADR) standardizes Demand Response (DR) and DER related issues to enable stakeholders such as operators, aggregators and customers to cost-effectively manage and participate in related

activities. OpenADR development represents a unique experience of how standards evolved through research, pilots, commercialization, specification development, informal standard development and, finally, to establishment of the **OpenADR Alliance** to create a formal standard and certification and testing program [42]. The important contribution of OpenADR Alliance is acknowledged by the IEC. It has approved the OpenADR 2.0b Profile Specification as a full IEC standard, to be known as IEC 62746-10-1 on systems interface between customer energy management system and the power management system.

Another interesting example is **EEBus** that emerged from the E-ENERGY lighthouse project funded by Germany's Federal Ministry of Economic Affairs and Climate Actions (BMWK) to **EEBus Initiative e.V.** The EEBus Initiative e.V. is the non-profit association that manages and supports the standardisation of EEBUS. EEBUS is a protocol suite for the IoT that aims at standardising the interface between electrical consumers, producers, storage and energy management systems. The EEBus Smart Premises Interoperable Neutral Message Exchange (SPINE) specification and Use Cases are published in EN 50631-1 on household appliances network and grid connectivity. Other standardisation activities are ongoing [43].

KNX Association is a non-profit-oriented organisation which develops and promotes the KNX standard for smart home and building solutions. KNX is approved as ISO/IEC 14543 on Home Electronic Systems (HES) architecture as well as EN 50090 on Home and Building Electronic Systems and EN 13321-1 on open data communication in building automation, controls and building management.

This overview of the different bodies highlights how complex the Smart Grid standardisation ecosystem structure is, and how unclear the relations among the different standards bodies are. This compounds the inherent complexity of such a concept as the Smart Grid that touches upon different domains of technology and innovation.

3.2. Standardisation Processes

Having introduced the bodies involved in Smart Grid Standardisation, we next describe the standardisation process, the types of deliverables and the approval processes so that we can understand the opportunities for researchers and innovators to participate.

Standardisation deliverables fall into the following general categories:

- A **European Standard** provides rules, guidelines or characteristics for activities or their results, for common and repeated use and is identified by a unique reference code, which contains the letters 'EN'. The national members of CEN and CENELEC have an obligation to adopt all full European Standards as national standards and to withdraw any conflicting national standards that are in their catalogue. The development of the European Standards follows strict procedure and might take up to 36 months from an idea to publishing. Although any interested party can introduce a proposal for new work – **New Work Item** proposal, the work is usually promoted by the members. Once the proposal for a standard has been evaluated and approved, the proposal goes on to the drafting stage. When the draft standard is finalized, it is released for public comment and vote, a process known as the 'enquiry'. During this stage, everyone who has an inter-

est may comment on the draft. Then, the votes and comments on the standard are evaluated and depending on the result, the draft standard is either published or updated and subsequently submitted to 'formal vote' stage for SDOs members to submit their vote and comments. If the result of the vote is positive, the standard is finalised and published. A European Standard adopted on the basis of a request made by EC for the application of Union harmonization legislation makes a **Harmonized Standard**. The references of harmonised standards are published in the Official Journal of the European Union (OJEU).

- A **Technical Specification** is close to the full standard in terms of detail, but has not yet passed through all approval stages. It is the option for setting specifications for evolving technologies because full standardisation could be seen as premature. It is a normative document, meaning that it contains requirements which must be met in order for claims of compliance with the standard to be certified. Technical Specifications are subject to optional national adoption.
- A **Technical Report** is an informative document that provides information on the technical content of standardisation work, i.e., data, measurement techniques, test approaches, case studies and methodologies. In contrast to a technical specification it does not contain any requirements. It is approved within the relevant Technical Committee. Technical Reports are subject to optional national adoption.

The Standards deliverables are developed and published by different formal and informal SDOs using various degrees of consensus in their preparation and approval, meaning that the standards published are selected and agreed by industry and stakeholders in the area and not by the organisations themselves. In case of **formal** SDOs, the approval process usually operates through national representation, rather than through organisation or individual representation. Thus, discussions within the Technical Committees of CEN and CENELEC are based on inputs by national delegations who represent the views expressed by the related groups at the national level, the national mirror groups. These mirror groups at the national level are composed of voluntary experts and stakeholders that take direct part in the writing of the standards.

In contract, ETSI is structured differently and operates by direct participation – ETSI members are not representatives of national delegations or other bodies, but mostly represent industrial companies and organisations. ETSI standards are developed by Technical Committees or other types of working groups, made up of ETSI members.

Furthermore, CEN and CENELEC offer a possibility for organisations to apply for status of Partner or Liaison Organisation [44]. R&I projects can be granted **Liaison Organisation** status for duration of the project, providing the consortium an opportunity to participate as an entity in the TC without voting rights.

Thus, R&I projects can contribute to the development of European Standards by individual partners being involved in the work of the TC, the national mirror group or by joining relevant TC as a project liaison.

As a faster pathway into standardisation and in support of innovative technologies, CEN and CENELEC have added the **CEN and/or CENELEC Workshop Agreement (CWA)** [45] to their portfolio of publications. A CWA is developed and agreed by the participants in CEN and/or CENELEC

Workshop. Participation is open to all stakeholders. A CWA is produced quickly (up to 12 months) to address specific market requirements in areas, which are not the subject of more formal standardisation. Therefore, it might serve as a good option for R&I projects, which have to deliver results within a limited timeframe. Moreover, there is also a possibility to indicate the participants and their organisations in the CWA foreword, in this way increasing the project visibility. The CWA can be considered the first step to a European Standard. If relevant, it may be proposed for conversion into the European Standard. In case it is approved by the Technical Committee, the CWA will have to go through the full standard development process and follow the rules for the development of European Standards.

4. RESULTS AND DISCUSSION

Having described the standardisation ecosystem and identified opportunities for participation, we next identify the contribution of EU R&I projects to SG standardisation to date, uncover in which standardisation activities collaborative EU R&I projects engage, and identify the factors influencing project engagement in standardisation processes.

4.1. General Findings

Based on [24], we identified 225 projects funded under 59 topics (calls) of H2020 with a total budget of 1.89 billion EUR, which includes Coordination and Support Actions (CSA), Research and Innovation Actions (RIA) and Innovation Actions (IA) (see Fig. 2).

	CSA	RIA	IA	Totals
Number of projects	36	71	118	225
Total investment	70.46 million EUR	284.21 million EUR	1.53 billion EUR	1.89 billion EUR
EU contribution	70.35 million EUR	279.63 million EUR	1.20 billion EUR	1.89 billion EUR
Number of projects addressing standardization	0	19	29	48
Share of projects addressing standardization	0	27 %	25 %	21 %

Fig. 2. Overview of H2020 Smart Grid projects.

IAs constitute the biggest share of projects in terms of number (32 %) and in terms of funding (77 % of EU funding). IAs aim at producing plans and arrangements or designs for new, altered or improved products, processes or services and may include prototyping, testing, demonstrating, piloting, large-scale product validation, market replication and only limited research and development activities [46]. Whereas, RIAs aim at establishing new knowledge and/or to exploring the feasibility of a new or improved technology, product, process, service or solution and include basic and applied research, technology development and integration, testing and validation on a small-scale prototype in a laboratory or simulated environment and only limited dem-

onstration activities [46]. Thus, RIAs are expected to have results with lower maturity – TRL2 to TRL6 depending on a specific topic, while IAs are usually intended to produce results with higher maturity and closer to implementation – TRLs between 6 and 8.

Our general overview uncovered that out of 48 EU projects (21% from our selection of 225 addressed standardisation activities), 19 were RIAs and 29 were IAs. We note that in relative numbers – the share of projects which include standardisation related activities is similar for RIAs (27 %) and IAs (25 %). We analyse this further to understand the level of contribution to development of new standards of the IAs and RIAs projects separately.

As for CSAs, these consist of accompanying measures such as standardisation, dissemination, awareness-raising and communication, networking, coordination or support services, policy dialogues and mutual learning exercises and studies, including design studies for new infrastructure. CSAs may also include complementary activities of strategic planning, networking and coordination between programmes in different countries [46]. In our analysis, none of the CSAs addressed standardisation development or innovation.

4.2. Standardisation Related Project Outcomes

Next, we manually checked relevant deliverables of projects addressing standardisation and extracted information on the level standardisation covered. Thus, using the proposed criteria described in the Methodology Section (Table 1), we estimate the level of contribution to standardisation activities. Figure 3 summarises the obtained results.

Level of contribution to standardization	RIA	IA	Totals	RIA	IA	Totals
Level 1 – standards screening	11	18	29	58 %	62 %	60 %
Level 2 – influence ongoing standardization	7	8	15	37 %	28 %	31 %
Level 3 – elaboration of a new standard	1	3	4	5 %	10 %	8 %
Totals	19	29	48	100 %	100 %	100 %

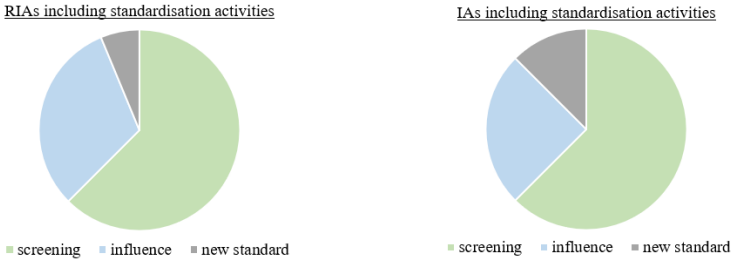

Fig. 3. Contribution to standardisation of H2020 smart grid projects.

Of the 48 projects, 29 (60 %) are involved in Level 1 “Screening”, 15 (31%) are involved in Level 2 “Influencing”, while four (8%) are involved in Level 3 “Elaborating a new standard”.

As mentioned above, the percentage of projects which include standardisation related activities is similar for RIAs and IAs

(Fig. 2). The shares of projects participating in standards development process, screening at 11/19 (or 58 %) for RIAs and 18/29 (or 62 %) for IAs are similar. Going beyond pure standards screening for project purposes and aiming to influence standards are similar both for RIAs (7 of 19 or 42 %) and IAs (8 of 29 of 38 %). This confirms that R&I projects in favourable circumstances can respond to the need for proactive standardisation at a point before the technology matures [47].

Therefore, we are curious if the level of contribution depends on the type of action. Our analysis confirms that IAs are more associated with initiating new standards development, being twice as likely (10 %) than RIAs (5 %) to be involved in Level 3 "Elaborating a new standard". This in line with expectations that the standardisation requires a certain maturity level of relevant technology.

As for project contribution to standardisation topics, we use domain definitions as introduced in [24]. We identified a single main domain for each project involved in Level 2 "Influencing" and Level 3 "Elaborating a new standard". The biggest input to standards development was made by projects focusing on Demand-side management, Smart network management and Other domains. Remaining domains, including E-mobility, Smart cities, Integration of distributed generation and storage and Integration of large-scale RES and storage, were addressed less frequently. It shall be noted that interoperability issues, including information models and relevant use cases, dominate linked standardisation activities across all domains.

4.3. PROJECT PATHWAYS TO STANDARDISATION

Table 1 summarises the contribution to standardisation activities of projects at Levels 2 and 3, which go beyond pure standards screening, highlighting the main outcomes and partner involvement. Four projects of our selection (SUCCESS, SMARTER TOGETHER, WiseGrid, InterConnect) initiated the elaboration of new standards. SMARTER TOGETHER and WiseGRID succeeded in the creation of CWAs: CWA 17381 on good practices for Smart City solutions [48], CWA 17382 on sustainable energy retrofit process management [49] and CWA 50714 on reference model for distribution application for microgrids [50]. SUCCESS initiated development of a new ETSI Technical Report [51] on smart meter security, whereas InterConnect initiated a development of preliminary Working item (PWI) on Digital Twin use cases [52]. WiseGrid was also nominated for the Standards+Innovation Awards by CENELEC in 2020 [53].

Furthermore, we identified two projects referred in European standards texts, i.e., FLEXICIENCY is referred in IEC 62325-451-10:2020 on the framework for energy market communications [54] and TDX-ASSIST is referred in IEC 61968-13:2021 on system interfaces for distribution management [55]. According to [56], including scientific papers in Standards bibliographies is not common. This highlights the significance of the contribution of the FLEXICIENCY and TDX-ASSIST projects. Furthermore, WiseGRID and TDX-ASSIST are included as best practice examples in the relevant study published by the Commission [57].

Other projects might be also refereed in the Standard's bibliography. However, bibliography analysis is not included in the scope of this study as in many cases this requires access to standardisation document data-

bases, which may incur financial costs.

We next explore how the projects engaged in the standardisation process. The vast majority of projects concentrated their effort in support of development of formal standards by contributing to the work of IEC and ETSI. Some of these provided their inputs to the IEC through the National Standardisation Bodies: The Slovenian Institute for Standardisation (SIST) (FutureFlow), Finnish National Electrotechnical Standardisation Organisation (SESKO) (DOMINOES), Croatian Standards Institute (HZN) (FLEXCoop), the Spanish Association for Standardisation (UNE) (GREENSOUL, USER-CHI and WiseGRID). UNE also participated as a project partner in WiseGRID and USER-CHI UNE. It shall be noted that only one project from our selection (PROMOTioN) used an opportunity and became a liaison partner of CENELEC TC.

Table 2. Contribution of EU Funded Horizon 2020 Smart Grid Projects to Standards Development

#	Project acronym Timeline Topic ID action type	Technical Committees / working groups of SDOs in which project partner(s) are involved	Standardisation Outcomes
Level 2 – Influence			
1	FLEXICIENCY 2015–2019 LCE-07-2014 IA	no information	Defining a common data model and communication protocol also for B2B interactions – EUropean Meter Exchange Data (EUMED) CIM [59]. Project's contribution taken on board by CG-SEG [36]. Project is referred in IEC 62325-451-10:2020 on the framework for energy market communications [54].
2	FHP 2016–2019 LCE-01-2016-2017 RIA	no information	Project participated in EEBus technical discussions trying to standardise the heat pump direct control/advice use case [60].
3	FutureFlow 2016–2019 LCE-06-2015 RIA	The Slovenian Institute for Standardisation (SIST) TC/PSE "Process systems in energy sector" [61]	Standardisation findings and amendments to the Smart Grid Reference Architecture (SGRA) presentation to SIST, contribution of Use Case descriptions and template to Smart Grid Use Cases repository through the IEC National Committee of Slovenia represented by SIST [61].
4	Storage4Grid 2016–2020 LCE-01-2016 RIA	IEEE-SA, IEC TC77/SC77A/WG9 "Power Quality measurement methods", TC38/WG 55 "Uncertainty evaluation in the calibration of Instrument Transformers", IEC SyC LVDC/OF Open Forum 1 "Platform for open exchange of technologies, innovations, challenges in LVDC", IEC SyC LVDC/WG 1 "LVDC Standards for Electricity Access", IEC TC8/JWG12 "Requirements for measurements used to control DER and loads", Portuguese national technical commission for electrotechnical standardisation (IPQ) [62]	Partners contributed to various activities within mentioned working groups [62].

5	PROMOTioN 2016–2020 LCE-05-2015 IA	IEC WGs (IEC TC88 WG27 “Wind turbines – Electrical simulation models for wind power generation” and other), IEEA-SA WGI10 “HVDC”, project became a liaison partner of CENELEC TC8X WG06 “Generic Smart Grid Requirements” [63]	Recommendations on harmonization of wind power plants (WPPs) connected to HVDC systems [64], recommendations on harmonisation of HVDC Systems [65]. Active contribution to CLC/TS 50654-1:2020 on HVDC Grid Systems and connected Converter Stations as a liaison partner of CENELEC TC8X WG06 [65].
6	CATALYST 2017–2020 EE-12-2017 IA	OpenADR Alliance, IETF, British Standards Institution [66]	Recommendations on ISO/IEC 30134 on Data Centres Sustainable Heat Exploitation (SHE) and Reuse of Waste Heat, or Heat Usage Effectiveness (HUE) KPIs standardisation [66].
7	DEFENDER 2017–2020 CIP-01-2016-2017 IA	Slovenian National Institute for Standardisation (SIST) Expert Board for standardisation in areas of electrotechnics, information technology and telecommunications [67]	Suggestions for improvements in information security standards, specifically, ISO 27000, ISO-IEC 27001, ISO-IEC 27002 on security, ISO-IEC 27019 [67].
8	TDX-ASSIST 2017–2020 LCE-05-2017 RIA	European Network of Transmission System Operators for Electricity (ENTSO-E) is one of projects partners and is a liaison partner with several of IEC TC57 WGs [68].	Recommendations on novel updates and extensions to CIM, feedback on tools used for Use Case development, contribution of a Use Case repository towards IEC SyC Smart Energy, project partners participated in some IEC meetings [69]. Project’s contribution taken on board by CG-SEG [36]. Project mentioned as best practice example in [57]. Project is referred in IEC 61968-13:2021 on Application integration at electric utilities – System interfaces for distribution management [55].
9	DOMINOES 2017–2021 LCE-01-2016-2017 RIA	Finnish National Electrotechnical Standardisation Organization (SESKO) committee SK8 “Systems aspects for electrical energy supply”, SESKO’s committee SK69 “Electrical road vehicles and industrial trucks” [70].	Project partners participated in IEC SyC LVDC, SESKO’s SK8 and SK69 meetings [70].
10	FLEXCoop 2017–2021 LCE-01-2016-2017 RIA	IEC TC 57 mirror committee of Croatian Standards Institute (HZN)[71].	Project partners participated in activities to adopt the OpenADR 2.0b within the IEC 62746 providing recommendations on standardizing the functions of flexibility infrastructure and cybersecurity [71].
11	HOLISDER 2017–2021 EE-12-2017 IA	OpenADR Alliance, IEC TC 57 - WG 21 “Interfaces and protocol profiles relevant to systems connected to the electrical grid” and WG 17 “Power system intelligent electronic device communication and associated data models for microgrids, distributed energy resources and distribution automation”, CENELEC TC205/WG18 “Smart grid, ETSI oneM2M [72]	Recommendations on IEC 61850 Series on Communication Protocols, IEC 62746 series on Systems and Interfaces between customer EMS and power management systems, Open ADR 2.0, SAREF [72].
12	EU-SysFlex 2017–2022 LCE-04-2017 IA	no information	Proposal for data exchange standards and protocols [73]. Project’s contribution taken on board by CG-SEG [36].

13	DRIMPAC 2018–2022 EE-12-2017 IA	IEC, CEN/CENELEC (working groups are not specified), OpenADR Alliance and ETSI oneM2M [74]	Planned to provide extensions to OpenADR and oneM2M [74].
14	GREENSOUL 2019–2019 EE-11-2015 RIA	Committee CNT178 “Smart Cities” of the Spanish Association for Standardisation (UNE) [75]	Contribution to the developments done with the Universal Monitoring Device and software with the NT178 WG Semantic in Smart Buildings [75].
15	USER-CHI 2020–2024* LC-GV-03-2019 IA	One of project partners – the Spanish Association for Standardisation (UNE) – is a member of CEN-CENELEC and of ISO-IEC as the National Standardisation Body [76]	Pending contribution to standardisation activities.
Level 3 – Elaboration of a new standard			
1	SUCCESS 2016–2018 DRS-12-2015 RIA	ETSI TC Cyber [77]	ETSI TR 103 644 “CYBER; Increasing smart meter security” [51].
2	SMARTER TOGETHER 2016–2020 SCC-01-2015 IA	no information	CWA 17381 “The Description and Assessment of Good Practices for Smart City solutions” [48] CWA 17382 “Sustainable Energy Retrofit Process Management for Multi-Occupancy Residential Buildings with Owner Communities” [49].
3	WiseGRID 2016–2020 LCE-02-2016 IA	One of project partners is the Spanish Association for Standardisation (UNE), which as the National Standardisation Body is a member of CEN-CENELEC and of ISO-IEC [78]	CWA 50714 “Reference model for distribution application for microgrids” [50]. Project included in [57]. Project was nominated for the Standards+Innovation Awards by CENELEC in 2020 [53].
4	InterConnect 2019–2024 * DT- ICT-10-2018-19 IA	ETSI ISG CIM, ETSI oneM2M, ETSI SmartM2M, CLC TC 59X – WG07 “Smart house”, CLC TC 205 – WG19 “Adhoc group on Energy management ontology”, CLC TC 205 – WG18 “Smart Grids”, ISO/IEC JTC1, IEC TC 69 [52]	Pending contribution to SAREF suite of ontologies (i.e., ETSI SmartM2M working items DEN/SmartM2M-123158 “SAREF Guidelines for IoT Semantic Interoperability”, DTR/SmartM2M-103781 “Study for SAREF ontology patterns and usage guidelines” and other) contribution to EN 50631 on a household appliances network and grid connectivity (primary use cases (PCUs from InterConnect German pilots), EN 50491-12-2:2022 on general requirements for Home and Building Electronic Systems (HBES) and Building Automation and Control Systems (BACS), ISO/IEC 21823-3 on IoT [52]. PWI JTC1-SC41-6 “Guidance for IoT and Digital Twin use cases” [52].

* The project is not finished, analysis is based on publicly available deliverables at the time of the study.

In summary, projects tend to engage in standardisation activities by being involved in ETSI TCs, IEC WGs or national mirror groups. This entails engaging in the standardisation process itself. Elaborating a CWA seems to be the easiest way for ini-

tiating a new standard. Meanwhile, becoming a liaison partner seems to require more resources and is underused by EU projects.

4.4. FACTORS FOR ENGAGEMENT IN STANDARDISATION

Next, we explored how the need of Smart Grid standardisation is addressed in funding calls and how these expectations are incorporated into project activities. We checked topic texts in order to understand if these included any references or explicit requirements to include standardisation activities in the project scope. We analysed projects funded under 59 different topics of H2020. It should be noted that 19 of these topics included references to standardisation using different wording, e.g., "solutions should be compatible with open standards", "include a detailed analysis of current standards", "explore the need for further standardisation", "demonstrate a good knowledge available or emerging standards", "demonstrate interoperability (e.g., through standards, protocols, regulatory framework)", etc.

In total, 70 projects were funded under these specific topics and 39 projects (56 %) included in their scope standardisation activities according to our identified criteria (Table 1). On the other hand, we identified only nine projects addressing standardisation out of 155 projects funded under other topics, which highlights that unless standardisation is explicitly included in the call, it is unlikely to be addressed in the proposals or funded projects.

Results are presented in Fig. 5. Hence, it seems that projects are more likely to include standardisation activities if it is mentioned in the call text. However, deeper contribution might be expected in case of explicit requirements in the call.

	Calls with reference to standardization	Calls with no reference to standardization
Total number of calls	19	40
Total number of funded projects	70	155
Total number of projects including standardization activities	39	9
Number of projects including elaboration of a new standard	3	1

Fig. 5. Overview of H2020 Smart Grid related funding calls and related projects in terms of refrence to standardisation.

Additionally, we conducted a concise analysis of project budgets. Due to the substantial variation in budgets across different projects, including factors such as the type of action, call requirements, scale of demonstrations, and technologies involved, it is challenging to draw definitive conclusions regarding the financial aspect. Nonetheless, our objective was to gain a high-level understanding of the financial allocations. We noticed that projects, which involved activities resulting in the elaboration of a

new standard, tended to have higher than average budgets (the average budget of all analysed RIAs was 4 million EUR, whereas the average budget of IAs was 12.98 million EUR). Involvement in the standardisation process might require additional resources, which should be foreseen during the planning stage of a European project. Therefore, potential project participants should evaluate the efforts needed as well as be aware of the benefits the project might get by being actively involved in the standardisation process.

Finally, we examined the geographic distribution of participants involved in the projects, which included active involvement in standardisation, i.e., at Levels 2 and 3 influencing or elaborating a new standard (Annex A). For the purpose of our analysis, we adopted the definition of "participation" as provided in [24], wherein it is defined as the involvement of a single organisation in a single project.

The geographical distribution of participations revealed differences between countries, with Spain, Italy and Germany emerging as the frontrunners in terms of the number of participations in Smart Grid projects showcasing good examples of addressing standardisation (Fig. 6). The same countries are identified as leaders in Smart Grid related projects in terms of both participation and shares of EU contribution in [24]. Hence, it seems that more successful countries in H2020 tend to demonstrate more involvement in standardisation activities in the frame of European projects.

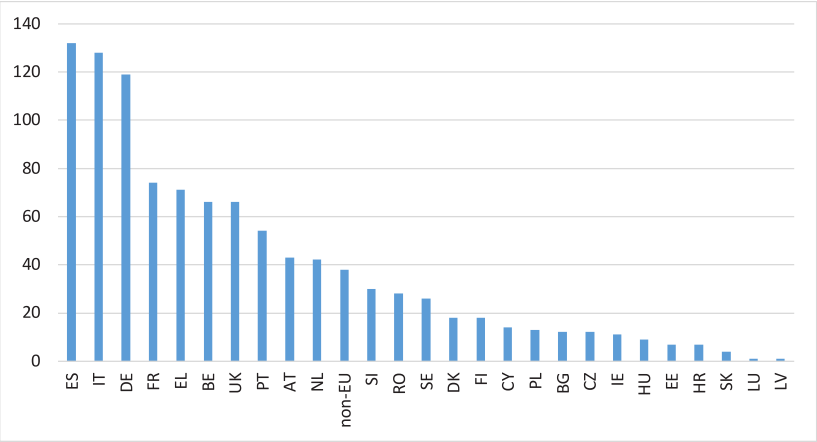

Fig. 6. Geographical distribution of participations.

Moreover, 10 of 19 projects demonstrating active involvement in standardisation are coordinated by organisations from the above-mentioned three countries – Spain, Italy and Germany. Typically, when project activities included engagement with National Standardisation Bodies, the coordinator often hailed from the same country as the respective National Standardisation Body. This alignment highlights the role of project coordinator in facilitating effective communication and collaboration between the project and standardisation organisations.

Standardisation can be seen as a means of implementing and disseminating the research results. For example, ref. [58] defines publishing, patenting and standardisation as alternative forms of knowledge disclosure practices and looks into

interlinks between these. It concludes that publishing and patenting, and patenting and developing standards, are substitutes, whereas there are no tensions between publishing and standardisation [58]. In this light, we also briefly examined how deeply Smart Grid projects are involved in publishing and patenting.

Projects from our selection produced in total 3953 publications, 1034 of which are peer-reviewed (almost five peer reviewed publications per project in average). As for Intellectual Property Rights (IPR) applications, so far, a limited number of IPRs are attributable to our selection of projects, i.e., according to CORDIS [25] data, eight patents have been granted until now. However, the number is not final, as the patenting process might take longer time. Thus, it seems that despite several good practices of capitalising on standardisation related activities, this pathway to valorise project results is not fully exploited.

5. CONCLUSION

A multi-mode approach is needed to facilitate the development of Smart Grid standards that connects researchers to industry practitioners. As shown in our analysis, EU funded public sector researchers can make and have made significant contributions to standards development through all stages of a technology maturity and industrial lifecycle. In this study, we have identified 21 % of EU Horizon 2020 Smart Grid projects that actively contributed to Smart Grid standardisation at different levels of understanding, influencing and elaborating new standards. We have identified which standardisation activities and smart grid domains such projects engage in, and explored the factors influencing engagement of such projects in Smart Grid standardisation processes.

Our study highlights the complexity of the Smart Grid standardisation ecosystem and shows that there are practical opportunities for funded research project partners to contribute to Smart Grid standardisation in a meaningful way. Our analysis also shows that specifying standardisation issues in the topic description can be a useful mechanism to ensure that standardisation needs and requirements are included into the project content and activities. We recommend such an action to ensure this opportunity is not missed.

REFERENCES

1. Zhang, Y., Chen, W., & Gao, W. (2017). A Survey on the Development Status and Challenges of Smart Grids in Main Driver Countries. *Renew. Sustain. Energy Rev.*, *79*, 137–147. doi: 10.1016/j.rser.2017.05.032
2. Tuballa, M. L., & Abundo, M. L. (2016). A Review of the Development of Smart Grid Technologies. *Renew. Sustain. Energy Rev.*, *59*, 710–725. doi: 10.1016/j.rser.2016.01.011
3. European Commission. (2019). *Communication from the Commission to the European Parliament, the European Council, the Council, the European Economic and Social Committee and the Committee of the Regions. The European Green Deal*. Available at https://eur-lex.europa.eu/legal-content/EN/TXT/?uri=COM%3A2019%3A640%3AFIN

4. European Commission Directorate-General for Energy. (2019). *Clean energy for all Europeans.* Publications Office of the European Union, 2019. Available at https://data.europa.eu/doi/10.2833/9937
5. European Commission. (2019). C*ommunication from the Commission to the European Parliament, the Council, the European Economic and Social Committee and the Committee of the Regions. Powering a Climate-Neutral Economy: An EU Strategy for Energy System Integration.* Available at https://eur-lex.europa.eu/legal-content/EN/ALL/?uri=COM:2020:299:FIN
6. Widergren, B. S., Melton, R., & Nordman, B. (2019). The Plug-and-Play Electricity Era: Interoperability to Integrate Anything, Anywhere, Anytime. *IEEE Power Energy Mag.*, *17* (5), 47–58. doi: 10.1109/MPE.2019.2921742
7. Gopstein, A., Nguyen, C., O'Fallon, C., Hastings, N., & Wollman, D. (2021). *NIST Framework and Roadmap for Smart Grid Interoperability Standards, Release 4.0, Special Publication (NIST SP).* Gaithersburg, MD, 2021. Available at https://www.nist.gov/publications/nist-framework-and-roadmap-smart-grid-interoperability-standards-release-40
8. MacDowell, J., Wang, Y., Quint, R., Chi, Y., Ernst, B., Saylors, S., … & Robinson, L. (2019). A Journey through Energy Systems Integration. *IEEE Power Energy Mag.*, *17* (6), 79–88. doi: 10.1109/MPE.2019.2933282
9. The European Parlament and the Council. (2022). *Regulation (EU) 2022/869 of the European Parliament and of the Council of 30 May 2022 on Guidelines for Trans-European Energy Infrastructure, Amending Regulations (EC) No 715/2009, (EU) 2019/942 and (EU) 2019/943 and Directives 2009/73/EC and (EU) 2019/94.* Official Journal of the European Union, L 152, 45–102. Available at http://data.europa.eu/eli/reg/2022/869/oj
10. The European Parlament and the Council. (2013). *Regulation (EU) No 347/2013 of the European Parliament and of the Council of 17 April 2013 on Guidelines for Trans-European Energy Infrastructure and Repealing Decision No 1364/2006/EC and Amending Regulations (EC) No 713/2009, (EC) No 714/2009 and (EC) No 715/2009.* Official Journal of the European Union, L 115, 228–264. Available at https://eur-lex.europa.eu/eli/reg/2013/347/oj
11. Hasan, M. K., Habib, AKM. A., Shukur, Z., Ibrahim, F., Islam, S., & Razzaque, Md. A. (2023). Review on Cyber-Physical and Cyber-Security System in Smart Grid: Standards, Protocols, Constraints, and Recommendations. *J. Netw. Comput. Appl.*, *209*, 103540, 2023, doi: 10.1016/j.jnca.2022.103540.
12. Gunduz, M. Z., & Das, R. (2020). Cyber-Security on Smart Grid: Threats and Potential Solutions. *Comput. Networks*, *169*, 107094. doi: 10.1016/j.comnet.2019.107094
13. O'Sullivan, E., & Brévignon-Dodin, L. (2012). *Role of Standardisation in Support of Emerging Technologies. A Study for the Department of Business, Innovation & Skills (BIS) and the British Standards Institution (BSI).* Institute for Manufacturing. University of Cambridge.
14. Wiegmann, P. M., De Vries, H. J., & Blind, K. (2017). Multi-Mode Standardisation: A Critical Review and a Research Agenda. *Res. Policy*, *46* (8), 1370–1386. doi: 10.1016/j.respol.2017.06.002
15. Mutule, A., Antoskova, I., Papadimitriou, C., Efthymiou, V., & Morch, A. (2021). Development of smart grid standards in view of energy system functionalities. In *2021 6th International Conference on Smart and Sustainable Technologies (SpliTech)* (pp. 1–6). doi: 10.23919/SpliTech52315.2021.9566337
16. Daniele, L., Den Hartog, F., & Roes, J. (2015). Created in Close Interaction with the Industry: The Smart Appliances REFerence (SAREF) Ontology. In *Formal Ontologies Meet Industry: 7th International Workshop, FOMI 2015,* (pp.100–112). 5 August 2015. Berlin, Germany. doi: 10.1007/978-3-319-21545-7
17. Sigrist, L., May, K., Morch, A., Verboven, P., Vingerhoets, P., & Rouco, L. (2016). On Scalability and Replicability of Smart Grid Projects — A Case Study. *Energies*, *9* (3), 19. doi: 10.3390/en9030195

18. Blind, K., & Mangelsdorf, A. (2016). Technovation Motives to Standardize : Empirical Evidence from Germany. *Technovation*, *48–49*, 13–24. doi: 10.1016/j.technovation.2016.01.001
19. Wakke, P., Blind, K., & Ramel, F. (2016). The Impact of Participation within Formal Standardization on Firm Performance. *J. Product. Anal.*, *45* (3), 317–330. doi: 10.1007/s11123-016-0465-3
20. Blind, K., Pohlisch, J., & Zi, A. (2018). Publishing, Patenting, and Standardization: Motives and Barriers of Scientists. *Res. Policy*, *47* (7), 1185–1197. doi: 10.1016/j.respol.2018.03.011
21. European Commission Directorate-General for Research and Innovation. (2017). I*nterim Evaluation of Horizon 2020: Commission Staff Working Document.* Publications Office of the European Union. doi: https://data.europa.eu/doi/10.2777/220768
22. European Commission. (2022). *Communication from the Commission to the European Parliament, the Council, the European Economic and Social Committee and the Committee of the Regions. An EU Strategy on Standardisation Setting Global Standards in Support of a Resilient, Green and Digital.* Available at https://eur-lex.europa.eu/legal-content/EN/TXT/?uri=CELEX%3A52022DC0031
23. HSbooster. (n.d.). *The European Standardisation Booster.* Available at https://www.hsbooster.eu/
24. Vasiljevska, J., Gangale, F., Covrig, L., & Mengolini, A. (2021). *Smart Grids and Beyond: An EU Research and Innovation Perspective*. Publications Office of the European Union, Luxembourg.
25. CORDIS. (n.d.) *CORDIS Brings You the Results of EU Research and Innovation*. Available at https://cordis.europa.eu/
26. EU Funding and Tenders Portal. (n.d.). Available at https://ec.europa.eu/info/funding-tenders/opportunities/portal/screen/opportunities/topic-search
27. European Committee for Standardization and European Committee for Electrotechnical Standardization. (2022). *CEN-CENELEC Guide 39. The Role of Standards in Support of Technology Transfer.* Available at https://www.cencenelec.eu/media/Guides/CEN-CLC/cenclcguide39.pdf
28. Hatto, P. (2013). *Standards and Standardisation: A Practical Guide for Researchers*. Luxembourg: Publications Office of the European Union. doi: 10.2777/10323
29. Standards + Innovation. (n.d.). Available at https://www.standardsplusinnovation.eu/
30. The European Parliament and the Council. (2012). *Regulation (EU) No 1025/2012 of the European Parliament and of the Council of 25 October 2012 on European Standardisation, Amending Council Directives 89/686/EEC and 93/15/EEC and Directives 94/9/EC, 94/25/EC, 95/16/EC, 97/23/EC, 98/34/EC, 2004/22/EC, 2007/23/EC, 2009/23/EC and 2009/105/EC*. Official Journal of the European Union, L 316. Available at https://eur-lex.europa.eu/eli/reg/2012/1025/oj
31. European Commission Directorate General for Energy. (2009). *Mandate M441 for Smart Meters*. Available at https://energy.ec.europa.eu/mandate-m441-smart-meters-march-2009_en
32. European Commission Directorate General for Energy. (2011). *Standardization Mandate to European Standardisation Organisations (ESOs) to Support European Smart Grid Deployment.* Available at https://energy.ec.europa.eu/mandate-m490-smart-grids-march-2011_en
33. CEN-CENELEC-ETSI Smart Grid Coordination Group. (2012). *Smart Grid Reference Architecture*. Available at https://www.cencenelec.eu/media/CEN-CENELEC/AreasOfWork/CEN-CENELEC_Topics/Smart Grids and Meters/Smart Grids/reference_architecture_smartgrids.pdf
34. CEN-CENELEC-ETSI Smart Grid Coordination Group. (2012). *First Set of Standards*. Available at https://www.cencenelec.eu/media/CEN-CENELEC/AreasOfWork/CEN-CENELEC_Topics/Smart Grids and Meters/Smart Grids/smartgrids_firstsetofstandards.pdf

35. CEN-CENELEC-ETSI Coordination Group on Smart Energy Grids. (2017). *SEGCG/ M490/ Smart Grid Set of Standards*. Available at https://www.cencenelec.eu/media/CEN-CENELEC/AreasOfWork/CEN-CENELEC_Topics/Smart Grids and Meters/Smart Grids/cgseg_sec_0042_report1.pdf
36. CEN-CENELEC-ETSI Coordination Group on Smart Energy Grids. (2019). *Final Report of the Working Group Clean Energy Package (WG-CEP).* Available at https://www.cencenelec.eu/media/CEN-CENELEC/AreasOfWork/CEN-CENELEC_Topics/Smart Grids and Meters/Smart Grids/finalreportwg-cep_2019.pdf
37. European Comission. (2016). *Regulation (EU) 2016/631 of 14 April 2016 Establishing a Network Code on Requirements for Grid Connection of Generators*. Official Journal of the European Union, L112. Available at https://eur-lex.europa.eu/legal-content/EN/TXT/?uri=CELEX%3A32016R0631
38. International Electrotechnical Commission. (2018). *Bringing Intelligence to the Grid*. Available at https://www.iec.ch/basecamp/bringing-intelligence-grid
39. International Electrotechnical Commission. (n.d.). *Smart Grid Map*. Availale at https://mapping.iec.ch/#/maps/1
40. Institute of Electrical and Electronics Engineers. (n.d.). *IEEE Approved & Proposed Standards Related to Smart Grid.* Available at https://smartgrid.ieee.org/about-ieee-smart-grid/standards/ieee-approved-proposed-standards-related-to-smart-grid
41. Smart Electric Power Alliance. (n.d.). *Catalogue of Standards*. Available at https://sepapower.org/knowledge/catalog-of-standards/catalog-of-standards-complete-list-of-entries/
42. Ghatikar, G., & Bienert, R. (2011). Smart grid standards and systems interoperability: A precedent with OpenADR. In *Proceedings of the Grid Interop Forum*, (pp. 1–7).
43. EEBUS E.V. (n.d.). *EEBUS Standrdization.* Available at https://www.eebus.org/our-work/#standarization
44. European Committee for Standardization and European Committee for Electrotechnical Standardization. (2021). *CEN-CENELEC Guide 25. The concept of Cooperation with European Organizations and Other Stakeholders.* Available at https://www.cencenelec.eu/media/Guides/CEN-CLC/cenclcguide25.pdf
45. European Committee for Standardization and European Committee for Electrotechnical Standardization. (2020). *CEN-CENELEC Guide 29. CEN/CENELEC Workshop Agreements – A Rapid Way to Standardization.* Available at https://www.cencenelec.eu/media/Guides/CEN-CLC/cenclcguide29.pdf
46. European Commission. (2019). H*ORIZON 2020 Work Programme 2018-2020, General Annexes.* Available at https://ec.europa.eu/research/participants/data/ref/h2020/other/wp/2018-2020/annexes/h2020-wp1820-annex-ga_en.pdf
47. Albers, E. (2014). Growth through partnerships and licensing technologies. In *ISO-CERN Conference Proceedings*, (pp. 84–92). Available at https://www.iso.org/files/live/sites/isoorg/files/store/en/PUB100404.pdf
48. European Committee for Standardization and European Committee for Electrotechnical Standardization. (2019). *CWA 17381. The Description and Assessment of Good Practices for Smart City Solutions.* Available at https://www.cencenelec.eu/media/CEN-CENELEC/CWAs/RI/cwa17381_2019.pdf
49. European Committee for Standardization and European Committee for Electrotechnical Standardization. (2020). *CWA 17382. Sustainable Energy Retrofit Process Management for Multi-Occupancy Residential Buildings with Owner Communities*. Available at https://www.cencenelec.eu/media/CEN-CENELEC/CWAs/RI/cwa17382_2020.pdf
50. European Committee for Standardization and European Committee for Electrotechnical Standardization. (2020). CWA 50714. Reference Model for Distribution Application for Microgrids. Available at https://www.cencenelec.eu/media/CEN-CENELEC/CWAs/RI/cwa50714_2020.pdf

51. European Telecommunications Standards Institute. (2019). *ETSI TR 103 644 CYBER. Increasing Smart Meter Security.* Available at https://www.etsi.org/deliver/etsi_tr/103600_103699/103644/01.01.01_60/tr_103644v010101p.pdf
52. Fiege, M., Georgakopoulos, A., Stavroulak, V., Skalidi, A., Daniele, L., Wijbrandi, W., … & Ferreira, A. (2021). *InterConnect D9.1 Standards and Regulatory Bodies Impact Plan.* Available at https://cordis.europa.eu/project/id/857237/results
53. European Committee for Standardization and European Committee for Electrotechnical Standardization. (2020). *List of Nominees 2020*. Available at https://www.cencenelec.eu/get-involved/research-and-innovation/cen-and-cenelec-activities/s-i-awards/list-of-nominees-2020/
54. International Electrotechnical Commission. (2020). *EC 62325-451-10:2020 Framework for Energy Market Communications - Part 451-10: Profiles for Energy Consumption Data* (My Energy Data). Available at https://webstore.iec.ch/publication/61111
55. International Electrotechnical Commission. (2021). *IEC 61968-13:2021 Application Integration at Electric Utilities - System Interfaces for Distribution Management - Part 13: Common Distribution Power System Model Profiles.* Available at https://webstore.iec.ch/publication/34213
56. Blind, K., & Fenton, A. (2022). Standard - Relevant Publications: Evidence, Processes and Influencing Factors. *Scientometrics*, *127* (1), 577–602. doi: 10.1007/s11192-021-04210-8
57. European Commission Directorate-General for Research and Innovation. (2022). *Scoping Study for Supporting the Development of a Code of Practice for Researchers on Standardisation: Final Report.* Publications Office of the European Union. Available at https://data.europa.eu/doi/10.2777/567608
58. Blind, K., Krieger, B., & Pellens, M. (2022). The Interplay between Product Innovation, Publishing, Patenting and Developing Standards. *Res. Policy*, *51* (7), 104556. doi: 10.1016/j.respol.2022.104556
59. FLEXICIENCY. (2019). *FLEXICIENCY Final Report D11.6.* Available at https://cordis.europa.eu/project/id/646482/results
60. Caerts, C., Johansson, C., & Ectors, D. (2017). *FHP D5.4 Report on Dissemination and Standardization Activities.* Available at https://cordis.europa.eu/project/id/731231/results
61. FutureFlow. (2019). *FutureFlow Deliverable 7.3 Actions Initiated with Standardization Organizations.* Available at https://cordis.europa.eu/project/id/691777/results
62. Albu, M., Sanduleac, M., Sturzeanu, M., & Delgado-Gomes, V. (2020). *Storage4Grid D7.6 - Report on the Contribution to Standardization.* Available at https://cordis.europa.eu/project/id/731155/results
63. Sørensen, P. (2019). *PROMOTION Deliverable 11.1 Harmonization Catalogue*. Available at https://cordis.europa.eu/project/id/691714/results
64. Sørensen, P. (2020). *PROMOTION Deliverable 11.3 Harmonization of Wind Power Plants Connected to HVDC Systems*. Available at https://cordis.europa.eu/project/id/691714/results
65. Brantl, C. (2020). *PROMOTION Deliverable 11.2 Report on Harmonisation of HVDC Systems.* Available at https://cordis.europa.eu/project/id/691714/results
66. Mammina, M., Booth, J., Anghel, I., Velivassaki, T., Out, E., & Piatek, W. (2020). *CATALYST Dissemination & Standardization Activities V3.* Available at https://cordis.europa.eu/project/id/768739/results
67. Kandzic, A., Caleta, D., Drosos, N., Gasparini, T. & Giunta, G. (2020). *DEFENDER Dissemination & Standardization Activities V3.* Available at https://cordis.europa.eu/project/id/740898/results/fr
68. International Electrotechnical Commission. (n.d.). *ENTSO-E: List of TC/SCs Liaisons.* Available at https://www.iec.ch/dyn/www/f?p=103:46:0::::FSP_ORG_ID:3384
69. TDX-ASSIST. (2020). *Update IEC Proposals.* Available at https://cordis.europa.eu/project/id/774500/results

70. Annala, S. (2021). *DOMINOES D6.11 Standardization proposals – Year 3*. Available at https://cordis.europa.eu/project/id/771066/results
71. Keko, H. (2021). *D8.14 – FLEXCoop Standardization Punch-list and Promotion Activities - Final Version.* Available at https://cordis.europa.eu/project/id/773909
72. Stluka, P. (2018). *HOLISDER D4.1 – Analysis of EU-Wide interoperability Standards and Data Models and Harmonization Requirements.* Available at https://cordis.europa.eu/project/id/768614/results
73. Kukk, K. (2021). *EU-SysFlex D5.5 Proposal for Data Exchange Standards and Protocols.* Available at https://cordis.europa.eu/project/id/773505/results
74. Andreadou, N. (2021). *DRIMPAC D5.1 Report on Activities for the Definition and Promotion of DRIMPAC Standardization Punch-List.* Available at https://cordis.europa.eu/project/id/768559.
75. Ávila, J. M. (2019). *GREENSOUL D7.09. Standardization Report*. Available at https://cordis.europa.eu/project/id/696129/results
76. López, J., & Aranda, M. Á. (2021). *USER-CHI Contribution to Standardisation.* Available at https://cordis.europa.eu/project/id/875187/results
77. Panagiotis, P. (2018). *SUCCESS Report on Standardisation and Policies, V3.* Available at https://cordis.europa.eu/project/id/700416/results
78. Zambrano, A. (2020). *D21.5 WiseGRID Contribution to Standardization V2*. Available at https://cordis.europa.eu/project/id/731205/results

sciendo

LATVIAN JOURNAL OF PHYSICS
AND TECHNICAL SCIENCES
2024, N 4

DOI: 10.2478/lpts-2024-0026

INVESTIGATION OF CENOSPHERE-BASED LIGHTWEIGHT CERAMIC MATRIXLESS SYNTACTIC FOAM THROUGH SPARK PLASMA SINTERING

T.V. Eiduks, R. Drunka, V. Abramovskis, I. Zalite,
P. Gavrilovs, J. Baronins, V. Lapkovskis

Faculty of Natural Sciences and Technology,
Riga Technical University
3 Paula Valdena Str., Riga, LV-1048, LATVIA
*e-mail: vjaceslavs.lapkovskis@rtu.lv

The current study introduces porous ceramic materials fabricated from cenospheres through spark plasma sintering. The investigation delves into the impact of sintering temperature, mould diameter (20 and 30 mm), and cenosphere size on the resulting material properties. Notably, sample shrinkage initiates at 900 °C and demonstrates an upward trend with temperature escalation, while a larger mould diameter contributes to sample shrinkage. Elevated sintering temperature leads to increased apparent density across various sample series, such as CS 63–150 μm in a 20 mm mould (0.97 to 2.3 g/cm³ at 1050–1300 °C), CS 150–250 μm in a 20 mm mould (0.93 to 1.96 g/cm³ at 1050–1200 °C), and others in different mould sizes. Total porosity decreases from 61.5 % to 3.9 % with a rising sintering temperature (1050 to 1250 °C), while open porosity starts decreasing at lower temperatures. Closed porosity peaks in samples sintered at 1150 °C. Furthermore, an increase in sintering temperature from 1050 to 1300 °C boosts the compressive strength of CS 63–150 samples in a 20 mm mould from 11 MPa to 312 MPa. These findings align with the Rice model, illustrating an exponential relationship between compressive strength, material porosity, and fully dense material compressive strength.

Keywords: *Cenospheres, porosity, porous ceramics, shrinkage, spark plasma sintering.*

1. INTRODUCTION

In the contemporary industrial landscape, there is a pressing need to innovate and produce lightweight and durable materials. This dual objective allows for creating more structurally efficient objects, necessitating reduced material usage and enabling compact designs, thus leading to economic benefits. In the context of vehicles, these benefits bring about energy conservation during their operation.

When developing a composite material, it becomes feasible to combine the distinctive properties of various materials into one [1]. To guarantee a high level of strength in the composite, it is important to incorporate a material inherently to have high strength [2], [3]. One of the promising components of lightweight materials is cenospheres (CS). These cenospheres are derived from the residue generated by coal-burning thermal power plants. A substantial quantity of ash, comprising cenospheres, is formed during coal combustion. The separation of cenospheres from the ash contributes to a reduction in waste produced by thermal power stations. It offers an opportunity to harness these unique ceramic particles for composite material development.

Cenospheres, derived from coal combustion residues, are available at a low cost as a component of fly ash from coal-fired power plants. They are characterised as chemically inert [4] and resistant to high temperatures, making them a successful type of hollow ceramic microbead for use as filler particles. These cenospheres have proven suitability, even with high-temperature processes [5]. The apparent density of cenospheres ranges from 0.4 to 0.8 g/cm^3, although depending on the definition, i.e. whether cenospheres are described as particles with an apparent density below that of water or as hollow particles, the maximum density will approach that of an alloy, i.e., about 2–2.6 g/cm^3 [6]. This happens because gas bubble is trapped in the centre of the particles, despite higher density of the material forming the cenosphere, which has a composition similar to that of flue gases, and also due to the fact that for different particle sizes, the ratio of diameter to wall thickness is constant at around 20–30 [7]. The diameter of the cenospheres ranges from 5 μm to over 600 μm, although most of the particles are between 20 μm and 300 μm in diameter [8].

Employing the CS, it is possible to synthesise lightweight composites called syntactic foams (SF) with enhanced mechanical properties and reduced weight [9]. SF synthesis typically uses matrix materials that are combined hollow spherical spheres (or microspheres) like glass hollow microbaloons [10], ceramic hollow spheres [11]–[13] or CS. Past decade CS was actively studied for a new SF design [14], [15], using various matrices: polymer [16]–[18], ceramic [19], [20], glass [21], [22], metals [23]–[25], natural ceramics (clay) [26], [27], cement [28], [29], hybrid materials [30], [31] and natural source matrix [10], [32]. However, a new version of SF, a matrix-less SF, was introduced. In this approach, CS was coated by metal using physical vapour deposition [33] and sintered by spark plasma sintering (SPS) to obtain single-piece material [34].

Spark plasma sintering stands out for its ability to control microstructure and adapt heating parameters through pulsed direct current and pressure. In the case of conductive materials, the formation of inter-particle contacts includes local melting. When employed as a furnace, SPS facilitates

high-rate heating for pre-consolidated specimens. Additionally, the utilisation of space holders in SPS allows for precise control over the structure of pore walls. Like other sintering techniques, SPS enables the creation of porous materials through methods such as partial densification, sintering hollow or porous particles, utilising decomposing pore formers, or employing space holders that are extracted during post-sintering (Fig. 1) [35].

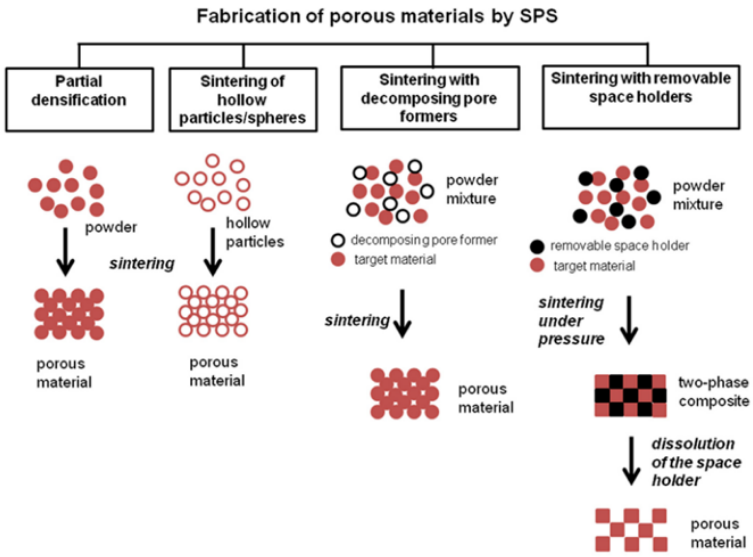

Fig. 1. Methods for creating porous materials using spark plasma sintering [35].

The spark plasma sintering method has proven instrumental in producing advanced ceramics such as nanostructural ceramics, functionally graded materials (FGMs), ceramic matrix composites, and nanocomposites. It proves to be an effective, non-conventional sintering method, ensuring the attainment of fully dense materials while preserving nanostructure features [36], [37]. SPS can achieve homogenous, highly dense sintered compacts at faster rates and lower temperatures, resulting in finer microstructures than conventional sintering methods [37]. Besides, SPS can be used to produce compact samples with high porosity (65–80 %), which is higher than using traditional methods (porosity limit – 50 %) for analogical materials [38], [39] and at the same time it is possible to produce corrosion-resistant fibres [40] and demonstrate notably low thermal diffusivity, making them appealing for applications in thermal management [41]. SPS of porous materials is a rapidly advancing field, holding great promise for developing energy-absorption materials, bioimplants, high-temperature filters, fuel cells, and thermoelectric materials [35].

In the current study, we explore the CS compaction and sintering without a matrix to determine behaviour, distinguish the main sintering stages, dependences and characterise material properties. For the first time, this study examines CS compaction behaviour in the SPS process. This study focuses on designing and characterising matrix-less SF foam containing CS only. The influence of sintering temperature, mould diameter (20 and 30 mm diameter), and the size of cenospheres on the properties of sintered

material is investigated. This primary data are essential for designing lightweight and thermally stable (up to 1000 °C) composite materials.

2. EXPERIMENTAL

The sintering material used in the study was the CS2 63–150 μm and CS1 150–250 μm fractions produced by burning coal from the Donetsk coal mine. The resulting fly ash of CS1 and CS2 was floated in a mixture of distilled water and ethanol, dried at 105 °C for 12 h, heat treated at 1100 °C for 30 min and fractionated into the above fractions by sieving. In CS1 and CS2, 46 % and 44 % of open volume fractions were observed in the burials of the prepared materials, respectively [8].

The chemical composition (Table 1) of cenospheres is directly related to the inorganic composition of the material burned, as these particles can only be formed from material left over from the combustion process.

Table 1. Chemical Composition of Cenospheres [6], [42]–[52]

	SiO_2	$Al\ O_{23}$	$Fe\ O_{23}$	CaO	$K\ O_2$	MgO	TiO_2	$At\ About_2$	$P\ O5_2$	SO_3
W_m, %	32.12-64.64	13.82-40.7	1-14.55	0.5-24.49	0.4-4.4	0.32-3.6	0.13-1.79	0.02-1.1	0.03-0.89	0.01-12.03

The samples were sintered in SPS sintering machine 'Dr. Sinter SPS825'. The machine is designed for sintering materials at temperatures up to 2400 °C with a sintering force of up to 250 kN. However, in this study, cenospheres were sintered from 1050 °C to 1300 °C at a material sintering force of approximately 0.6 kN using 20 mm, 30 mm, and 50 mm dies. These settings were chosen with the relative brittleness of the material to be sintered, the cenospheres, compared to homogeneous, dense raw materials and the need to produce low-density ceramics.

The samples were prepared for sintering in the SPS machine by lining a 20.7 mm graphite die with 0.35 mm graphite paper, inserting a 20x30 mm bottom plunger and lining its surface in contact with the material to be sintered with 0.35 mm graphite paper, rubbing in 7 grams of 63–150 μm cenospheres, compacting the material to be sintered by gently shaking the die, placing a cylindrical 0.35 mm thick graphite paper on top of the sample to be sintered and inserting the upper graphite plunger into the die. The outside of the die was covered with a 4.5 mm thick carbon fibre thermal insulating material and secured with a carbon fibre cord. The prepared die was placed in the vacuum chamber of the SPS machine with three cylindrical graphite discs of the appropriate size on each side between the plungers of the die and the electrodes of the SPS machine, with 0.35 mm thick graphite paper between the largest of these discs and the electrodes of the machine. The die was placed in a position where the axis of the pyrometer used to measure the temperature coincided with the temperature observation bore so that the temperature was closer to the material to be sintered than to the surface of the die.

The die was inserted into the SPS machine, electrodes adjusted, and clamping force applied (0.6 kN). This pressure, equivalent to 1.9 MPa on a 20 mm die, compressed the sample for 10 minutes. Shrink-

age was measured and held for 20 minutes under reduced atmospheric pressure (6 Pa) until vacuum-related shrinkage ceased. SPS sintering used consistent temperature rise programs, gradually reaching sintering temperature to prevent overheating and sample heterogeneity. Post-sintering, vacuum cooling for 20 minutes ensued until the sample hit around 300 °C. Opening the vacuum chamber accelerated cooling, and 10 minutes later, the sample was extracted. A similar tailored process was applied to samples with diverse cenosphere sizes and die dimensions, adjusting plunger size and material amount accordingly.

2.1. Determination of the Quantity of Collapsed Cenospheres

Cenosphere collapse during sample compression and vacuuming in the SPS machine was assessed experimentally. The process involved weighing the material in a mould using an Acculab VIC-612 balance. The material was then placed in a container, covered with deionized water (at least 5 cm thick), mixed, and left to settle for an hour. Floating particles were removed, water was decanted, and the sinking material was transferred to a smaller container. After drying, the mass of collapsed cenospheres was determined.

The apparent density of the sintered samples was determined according to Formula 2.3 using an Acculab VIC-612 balance to determine the weight of the sample.

$$\rho_{\text{apparent}} = \frac{\pi d^2 h}{4m}, \quad (1)$$

where
d – diameter of the sintered sample;
h – height of the sintered sample;
m – mass of the sintered sample.

To assess open porosity, post-sintering materials were sanded to remove graphite paper, dried at 70 °C for four hours, and weighed using an AND GR-200 analytical balance. Boiling in distilled water for four hours saturated open pores. Weight in the water-immersed state was determined using an AD-1653 kit after surface drying. Open porosity, closed porosity, and the ratio of open and closed pore volumes to aluminosilicate volume were calculated. Compressive strength was measured with a Toni Technik ToniNORM model 2020 tester, applying progressively increasing force until a 1.2 % force drop indicated specimen collapse.

XRD analysis employed a Rigaku Ultima+ with a copper cathode X-ray tube (40 kV voltage, 5 mA current). Diffraction images were taken between 5 and 80 ° 2θ at a 4 °/min scan rate. MDI Jade 9 software and electronic ICDD databases PDF-4+ 2023 and PDF-4 Organics were used for phase analysis. Diffraction image preparation in Origin 2023b included noise reduction using an FFT filter with a 5 data point window.

Magnetic fractions of CS 63–150 µm and CS 150–250 µm particles were isolated from the sinterable material. A 30 g layer of the material was spread on paper, and a cylindrical neodymium magnet was moved near the surface. Adhering particles were periodically removed and transferred to a separate container. Fractions were weighed, and the magnetic fraction percentage was calculated using a formula below.

$$W_{mag} = \frac{m_{mag}}{m_{mag} + m_{nonmag}}, \quad (2)$$

where
mm_{ag} – mass of the magnetic fraction of the cenospheres;
m_{nonmag} – mass of the non-magnetic fraction of cenospheres.

3. RESULTS AND DISCUSSION

3.1. Particle Destruction before the SPS Process

Shrinkage results indicate significant pre-sintering shrinkage in the samples during compression force and vacuum application in the SPS chamber. Approximately 9.7 % and 24.5 % of the initial height of the sample in the die occurred at the time of compression force and vacuum generation, respectively. This initial shrinkage is attributed to cenosphere collapse, validated by the flotation of non-sintered cenospheres in water after force and vacuum application, revealing 21 % and 20 % of collapsed cenospheres, respectively, based on the initial material mass. In a 50 mm die with lower compression force, pressing-induced shrinkage was 0.88 mm, and vacuuming caused no further shrinkage, reducing broken cenospheres to 3 %. The reduced pressure in a larger die likely contributed to this outcome. Testing 150– 250 µm cenospheres in a 20 mm die showed more significant destruction, with 23 % being destroyed after force application and an additional 37 % after vacuuming, surpassing the smaller particle fraction.

3.2. Sample Shrinkage during the SPS Process

Figure 2 illustrates that with increasing sintering temperature, the sample height decreases, indicating enhanced particle compaction and softening. This results in reduced open and closed porosity, facilitating more material shrinkage. The data show a trend of reaching a specific shrinkage value at higher temperatures, sharply dropping to zero. This suggests less effective sintering at lower temperatures, with the apparent density approaching that of unsintered particles. Contrary to expectations, attempting to sinter at 1000 °C did not yield cohesive material, as evident in Figs. 3 and 4, where shrinkage started at 900 °C. However, temperature rise reveals a notable difference between measured and sample temperature due to die thermal inertia.

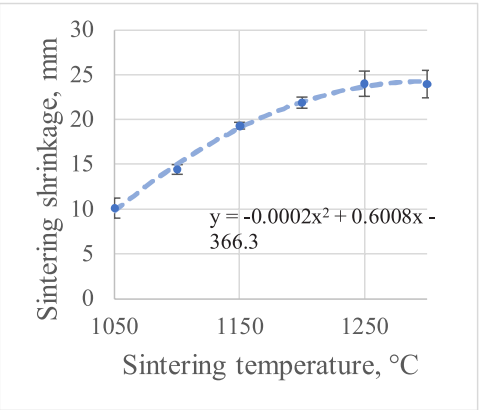

Fig. 2. Shrinkage of CS 63–150 µm samples sintered in a 20 mm die during the SPS process as a function of sintering temperature.

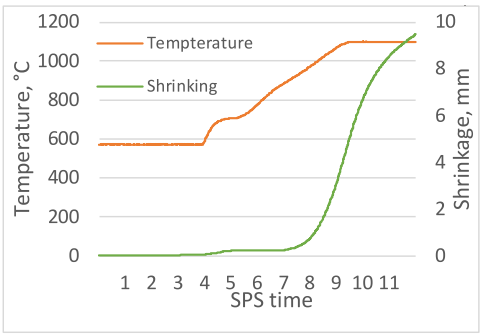

Fig. 3. Sintering process data for CS 63–150 µm sample sintered at 1050 °C.

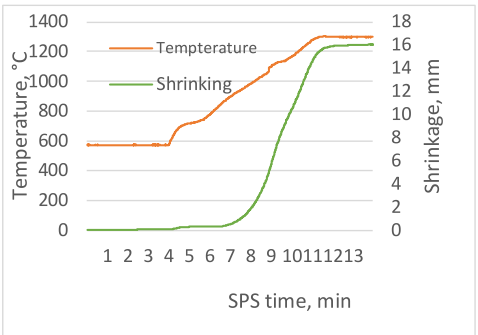

Fig. 4. Sintering process data for CS 63–150 µm sample sintered at 1300 °C.

Examining the sintering data in Figs. 3 and 4 reveals that at lower temperatures, the process halts before complete sample shrinkage, indicating incomplete particle sintering. Conversely, at higher temperatures, shrinkage stops shortly after reaching the sintering temperature due to cenosphere softening, expediting equilibrium attainment at the same compression force. Comparing shrinkage at different stages of sample formation exposes peculiarities. Figure 5 indicates that samples from the 150–250 µm cenosphere fraction exhibit less shrinkage during the SPS process, a distinction diminishing with rising sintering temperature. Thicker walls of these particles potentially explain this variance. However, as temperature increases, softening diminishes the impact of thicker walls on mechanical strength. Specimens sintered in 30 mm dies experience reduced shrinkage during pressing and vacuuming due to lower surface pressure from their larger diameter. Yet, their sintering shrinkage is notably higher, likely due to particle breakage or deformation at elevated temperatures, in contrast to samples in 50 mm dies with even lower pressure.

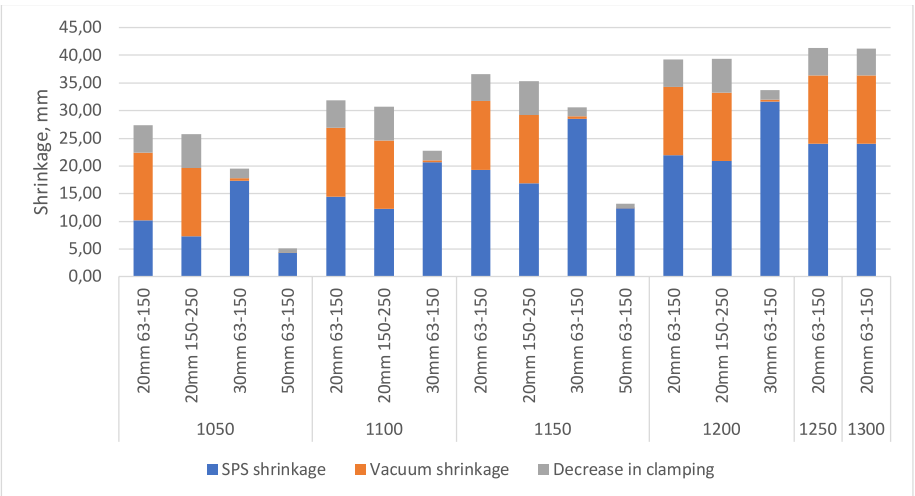

Fig. 5. Shrinkage of specimens after squeezing, vacuum and SPS processes, depending on sintering temperature, material used and die diameter.

3.3. The Apparent Density of the Resulting Materials

Figure 6 illustrates an increase in the apparent density of sintered cenosphere samples with higher sintering temperatures. However, this relationship is non-linear within the data range. At 1050 °C, complete sintering between particles is inadequate, while at 1300 °C, particles soften and compress. Extending the temperature range for sintering could reveal a trend towards the density of the material in the cenosphere burial at lower temperatures and the proper density of the material forming the cenosphere at higher temperatures. Despite achieving an R2 value of 0.989, a third-order polynomial in non-linear regression analysis may not yield an appropriate function for predicting the data due to these complexities.

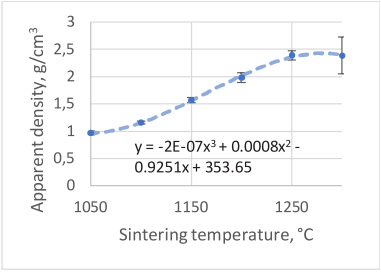

Fig. 6. The apparent density of CS 63– 150 μm samples sintered in a 20 mm die as a function of sintering temperature.

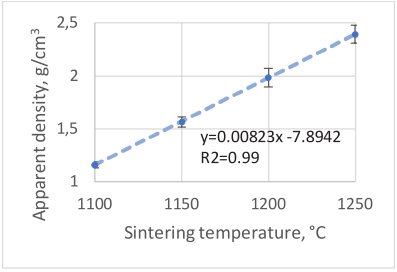

Fig. 7. The apparent density of sintered CS 63–150 μm samples versus sintering temperature from 1100 °C to 1250 °C.

In the temperature range of 1100 °C to 1250 °C, a distinct linear increase in density with sintering temperature is evident, depicted in Fig. 7 with R2 = 0.99. The linear regression analysis yields the function ρ=0.0082xT-7.89. This implies that, within these sintering conditions, predicting the apparent density of resulting materials is reliable based on the known sintering temperature.

However, when considering the entire set of samples and individual batches, there is no linear relationship between sample shrinkage and apparent density, contrary to expectations from the apparent density formula. Consequently, estimating this relationship is challenging, but a more feasible approach involves establishing the connection between the measured apparent density and the predicted apparent density derived from observed sample shrinkage.

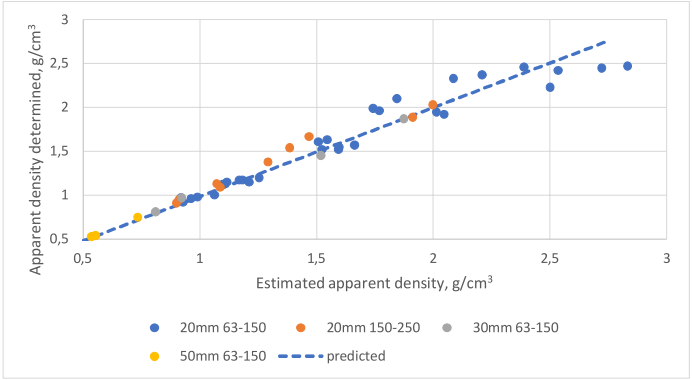

Fig. 8. Relationship between predicted and observed apparent density of samples.

Figure 8 reveals an approximately linear relationship between predicted and determined apparent densities. This suggests that knowing the sample shrinkage at all process stages, its initial mass and height, and the internal diameter of the die allows predicting the apparent density of a sintered sample. The data also indicate minimal mass loss during sintering. However, increased scatter in the higher predicted apparent densities results from errors in determining apparent densities, attributed to reduced sample volume and slight material bleed between the die and its plunger at elevated sintering temperatures.

3.4. Porosity of the Resulting Materials

The open porosity of the samples, depicted in Fig. 9, diminishes with rising sintering temperature, resulting in samples displaying open porosity ranging from 0.28 % to 43 %. This relationship is nonlinear, with the most pronounced decrease occurring between 1100 °C and 1150 °C. This likely happens because cenosphere particles become soft, allowing for slight deformation and more efficient packing, thereby reducing inter-ionospheric space and closing some open pores. The slowdown in open porosity decrease at higher sintering temperatures is attributed to the increasing difficulty in denser particle packing.

Figure 9 shows that the closed porosity of the sintered materials peaks between 1100 °C and 1200 °C. This is explained by the significant difference in the rate of closed and open pore volume reduction in this temperature range (see Fig. 10). The closed pore volume reduction rate is highest between 1150 °C and 1250 °C, in contrast to 1100 °C and 1150 °C for open pores. This suggests the possibility of producing cenospheric ceramics with a specific open-to-closed pore volume ratio if required.

The total porosity of the sintered samples diminishes with increasing sintering temperature, displaying a strongly linear decrease between 1100 °C and 1250 °C, consistent with the expected trend from apparent density changes with sintering temperature. This alignment supports the reliability of the porosity determination, indicating the absence of gross errors.

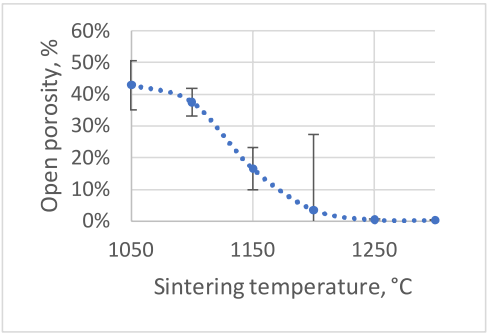

Fig. 9. Open porosity of sintered CS 63–150 µm samples as a function of sintering temperature.

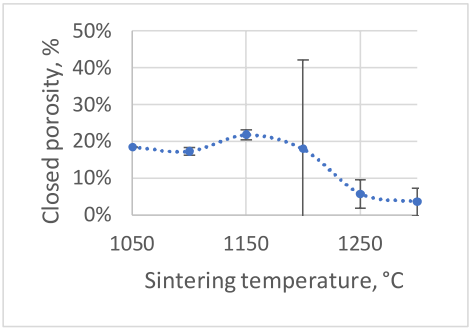

Fig. 10. Closed porosity of sintered CS 63–150 µm samples as a function of sintering temperature.

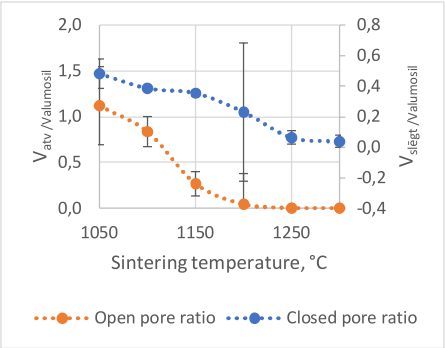

Fig. 11. The ratio of closed and open pore volumes of sintered CS 63–150 µm samples to the volume of aluminosilicate as a function of sintering temperature.

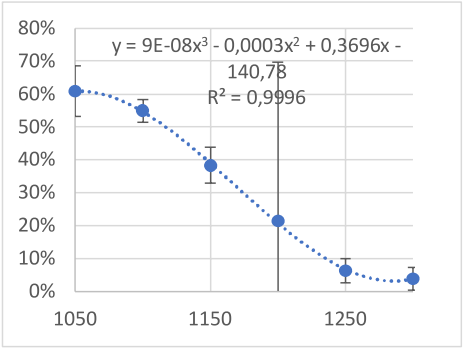

Fig. 12. Total porosity of CS 63–150 µm samples sintered in a 20 mm die as a function of sintering temperature.

3.5. Morphology of the Resulting Materials

The optical microscopy image in Fig. 13, depicting a CS sample sintered at 1050 °C, reveals that most cenospheres at this temperature remained intact, indicating that the softening point was not reached. Fusion bridges between some cenospheres were observed, but their quantity was visually minimal, contributing to the lower mechanical strength compared to samples sintered at higher temperatures. At this magnification, no notable structural difference was observed between edge and centre regions, suggesting a uniform temperature and compressive force gradient during sintering, similar to sample SPS-944. Some undestroyed cenospheres exhibit translucent bubbles, likely resulting from epoxy partial penetration during sample impregnation, indicating holes in these particles. These holes could stem from cenospheres being too small for water filling during flotation, cracks in walls during pressing or vacuuming, or internal stresses during sample cooling post-sintering.

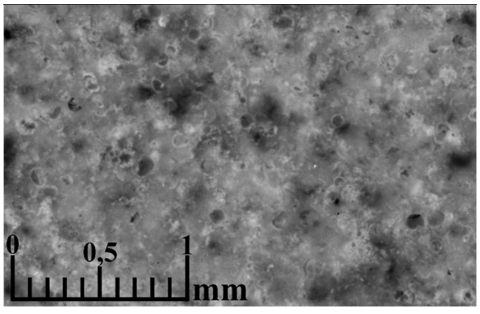

Fig. 13. Optical microscopy image of CS 63–150 µm sample SPS-886 sintered at 1050 °C, perpendicular to the squeeze axis.

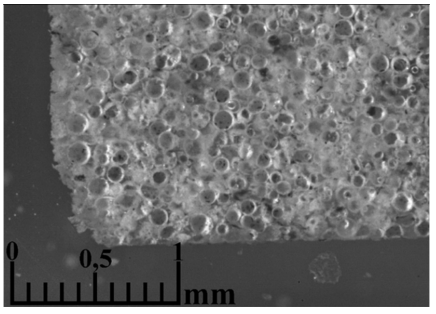

Fig. 14. Optical microscopy image of CS 63–150µm sample SPS-944 sintered at 1200 °C, perpendicular to the squeeze axis.

In the sample sintered at 1200°C (Fig. 14), cenosphere deformation indicates soft melting during sintering, contributing to the formation of compacted regions. Some hollow particles softened enough for the applied compressive force to flatten them, creating

dense material regions. This aligns with the high shrinkage during sintering, increasing with temperature. Magnetic cenospheres, appearing darker in the images, melted and formed higher magnetite content regions in the fused material. Apart from undestroyed cenospheres, numerous plhenospheres are present. Their outer walls melted, but the inner particles largely retained their shape, distinguishing them from the bulk material.

The sample sintered at 1250 °C (Fig. 15) exhibits few closed pores, mainly formed by deformed particles within cenospheres and plhenospheres, resembling the sample sintered at 1200 °C. In Fig. 16, a dense 100 μm thick alloy material layer forms at the die-material interface near the plungers but it is not observed at greater distances. Deeper regions within the material exhibit better sintering, likely due to preferential current flow channels formed during the process. Figure 17 highlights significantly poorer sintering in the sample centre, where the material remains slightly red, indicating potential temperature non-uniformity. This may result from the low electrical and thermal conductivity of the particle, causing outer heating. Addressing this could involve extending the sample curing time for complete heating. However, if incomplete sintering in the sample centre is due to uneven force distribution during SPS, solutions may require increased squeezing force, intensifying shrinkage and apparent density, or a reduction in the h/d ratio, limiting material thickness.

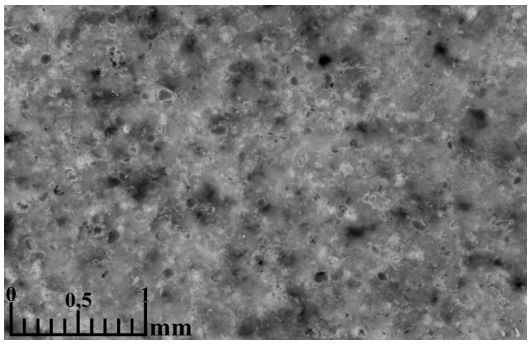

Fig. 15. Optical microscopy image of CS 63– 150 μm sample SPS-948 sintered at 1250 °C, perpendicular to the squeeze axis.

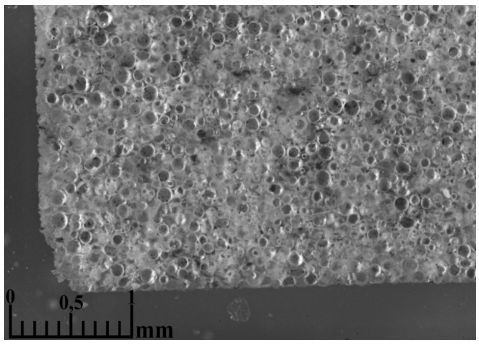

Fig. 16. Optical microscopy image of a 50 mm die sintered CS 63–150 μm sample SPS-951 at 1050 °C, parallel to the die axis, close to the material-die boundary.

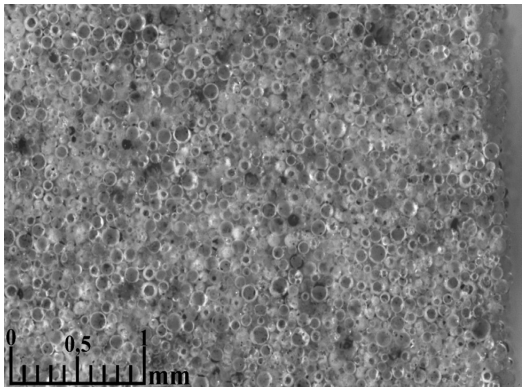

Fig. 17. Optical microscopy image of a 50 mm die sintered CS 63–150 μm sample SPS-951 at 1050 °C, parallel to the press axis at the centre of the specimen.

3.6. Compressive Strength of the Resulting Materials

All specimens tested exhibit brittleness, which is characterised by spontaneous collapse without significant formation of large cracks or deformation. However, at the highest temperatures, small ceramic pieces detached in some cases due to insufficient sample homogeneity or non-uniform contact surfaces with the testing apparatus. In Fig. 18, compressive strength of the samples increases at higher sintering temperatures. This is likely attributed to enhanced binding between cenospheric particles, particularly noticeable at lower sintering temperatures where particle binding is relatively weak. Additionally, the correlation between density and mechanical strength in high-porosity materials contributes to the observed effect.

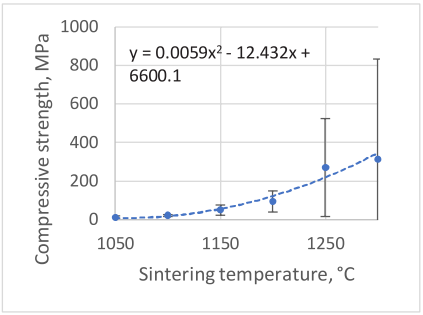

Fig. 18. Compressive strength of sintered cenospheric specimens as a function of sintering temperature.

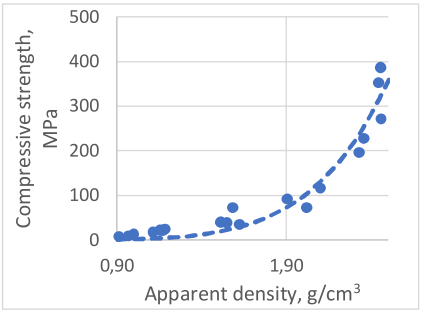

Fig. 19. Dependence of compressive strength on apparent density of sintered specimens.

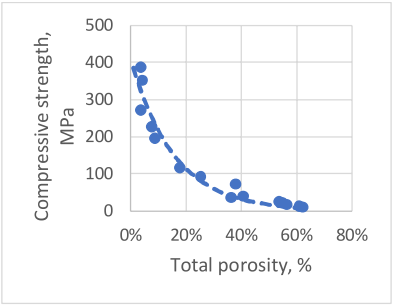

Fig. 20. Dependence of compressive strength on total porosity of sintered samples.

The Gibson-Ashby model for predicting the properties of lath-type and porous materials, which is reducible to a power function, does not allow for a conclusive correlation between the compressive strength results obtained for the specimens, giving R^2 =0.93. An additional problem is the lack of reliable data on which to base the compressive strength and density of a fully compacted, sintered cenospheric sample. This means that the model cannot be used in this case. The model put forward by Rice gives a visually and mathematically better agreement with R^2 =0.94. In addition, this model also gives a reliable value for the compressive strength of a dense material σ_s =411.1 MPa since, as mentioned above, these values are not known.

3.7. Composition of the Crystalline Phases of the Starting Materials and Samples

Figure 21 indicates no significant phase composition differences between the unsintered material and the sample sintered at 1050 °C. Mullite and an X-ray amorphous phase, likely originating from the amorphous part of the cenospheres predominantly composed of SiO2, are the main components in the range of 18°–27° 2θ. The sample sintered at 1300 °C introduces an additional phase consistent with cristobalite, possibly formed from the partial melting and subsequent crystallization of amorphous cenosphere regions due to slower cooling. Despite confirming the presence of a magnetic phase in some sinterable particles through interaction with an external magnetic field, this crystalline phase is not observed in the XRD results, possibly due to its relatively low content. Weak interaction of the sintered samples with an external magnetic field suggests either retention of some magnetic phase during the SPS process or the generation of another magnetic phase.

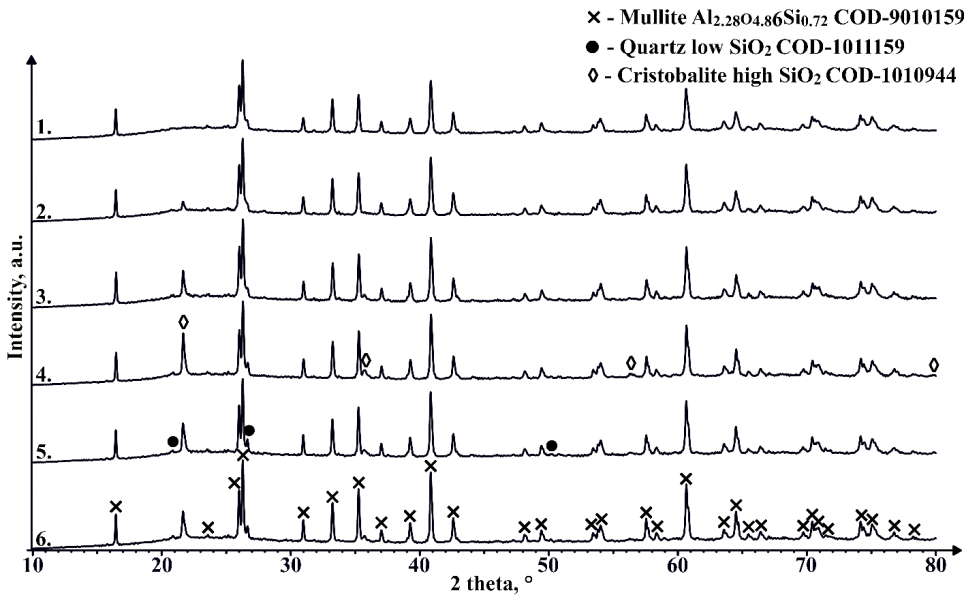

Fig. 21. 1050 °C (1), 1100 °C (2), 1150 °C (3), 1200 °C (4), 1250 °C (5) un 1300 °C (6) XRD results of samples sintered in a 20 mm die at 2 min.

4. CONCLUSIONS

The sample shrinkage before the beginning of the sintering process decreases with increasing mould diameter, which is caused by decreasing breaking of cenospheres, which can be explained by decreased pressure on the material.

The sample shrinkage during the sintering process began at 900 °C, which shows that using the SPS method, the sintering of cenosphere particles starts between 900 and 1000 °C. Shrinkage of samples during sintering increases with increasing temperature

and decreases with increasing mould diameter.

Increasing sample sintering temperature increases the apparent density of all sample series – CS 63–150μm in 20 mm mould from 0.97 to 2.3 g/cm^3 at 1050–1300 °C, in 30 mm mould from 0.81 to 1.87g/cm^3 at 1050–1200 °C, in 50 mm mould from 0.54 to 0.75g/cm^3 at 1050–1150 °C, while CS 150–250 μm in 20 mm mould from 0.93 to 1.96g/cm^3 at 1050– 1200 °C.

Total porosity decreases from 61.5 % to 3.9 %, increasing the sintering temperature from 1050 to 1250 °C, while open porosity starts to decrease at lower temperatures, closed porosity becomes the highest in samples sintered at 1150 °C.

Increasing the sintering temperature from 1050 to 1300 °C, the compressive strength of CS 63–150 samples made in 20 mm mould increases from 11 MPa to 312 MPa. These results correlate with the Rice model, which describes exponential compressive strength dependence on material porosity and completely dense material compressive strength.

The XRD pattern of a sample sintered at 1300 °C temperature reveals a phase not in the unsintered material – cristobalite.

ACKNOWLEDGEMENTS

The research has been funded by VPP AIPP project No. VPP-AIPP-2021/1-0015 "Combined Lightweight, High-Temperature Resistant Hybrid Composite for Combined Protection of Drones from Direct Energy Weapon". The article has been published with financial support from the Research Support Fund of Riga Technical University.

REFERENCES

1. Nielsen, L. F. (2005). *Composite Materials*. Springer Berlin Heidelberg. https://doi.org/10.1007/978-3-540-27680-7
2. Qin, Q. H. (2015). Introduction to the composite and its toughening mechanisms. In *Toughening Mechanisms in Composite Materials* (pp. 1–32). Elsevier. https://doi.org/10.1016/B978-1-78242-279-2.00001-9
3. Barbero, E. J. (2010). *Introduction to Composite Materials Design*. CRC Press. https://doi.org/10.1201/9781439894132
4. Shishkin, A., Mironovs, V., Lapkovskis, V., Treijs, J., & Korjakins, A. (2014). Ferromagnetic Sorbents for Collection and Utilization of Oil Products. *Key Engineering Materials*, *604*. https://doi.org/10.4028/www.scientific.net/KEM.604.122
5. Shishkin, A., Mironovs, V., Zemchenkov, V., Antonov, M., & Hussainova, I. (2016). Hybrid Syntactic Foams of Metal-Fly Ash Cenosphere-Clay. *Key Engineering Materials*, *674*. https://doi.org/10.4028/www.scientific.net/KEM.674.35
6. Acar, I., & Atalay, M. U. (2016). Recovery Potentials of Cenospheres from Bituminous Coal Fly Ashes. *Fuel*, *180*, 97–105. https://doi.org/10.1016/j.fuel.2016.04.013
7. Ranjbar, N., & Kuenzel, C. (2017). Cenospheres: A Review. *Fuel*, *207*, 1–12. https://doi.org/10.1016/J.FUEL.2017.06.059
8. Shishkin, A., Abramovskis, V., Zalite, I., Singh, A. K., Mezinskis, G., Popov, V., & Ozolins, J. (2023). Physical, Thermal, and Chemical Properties of Fly Ash Cenospheres Obtained from Different Sources. *Materials*, *16* (5). https://doi.org/10.3390/ma16052035

9. Weise, J., Lehmhus, D., Baumeister, J., Kun, R., Bayoumi, M., & Busse, M. (2014). Production and Properties of 316l Stainless Steel Cellular Materials and Syntactic Foams. *Steel Research International*, *85* (3), 486–497. https://doi.org/10.1002/srin.201300131
10. Yashas Gowda, T. G., Sanjay, M. R., Subrahmanya Bhat, K., Madhu, P., Senthamaraikannan, P., & Yogesha, B. (2018). Polymer Matrix-Natural Fiber Composites: An Overview. *Cogent Engineering*, *5* (1). https://doi.org/10.1080/23311916.2018.1446667
11. Zhang, J., Gong, M., Tian, C., & Wang, C.-A. (2016). Facile Synthesis of Well-Defined CeO2 Hollow Spheres with a Tunable Pore Structure. *Ceramics International*, *42* (5), 6088–6093. https://doi.org/10.1016/j.ceramint.2015.12.166
12. Ozcivici, E., & Singh, R. P. (2005). Fabrication and Characterization of Ceramic Foams Based on Silicon Carbide Matrix and Hollow Alumino-Silicate Spheres. *Journal of the American Ceramic Society*, *88* (12), 3338–3345. https://doi.org/10.1111/j.1551-2916.2005.00612.x
13. Thijs, I., Luyten, J., & Mullens, S. (2003). Producing Ceramic Foams with Hollow Spheres. *Journal of American Ceramic Society, 72* (186975), 2002–2004.
14. Biju-Duval, P. (2007). *A New Porous Material Based on Cenospheres*. Georgia Institute of Technology.
15. Długosz, P., Darłak, P., Purgert, R.M., & Sobczak, J.J. (2011). Synthesis of Light Composites Reinforced with Cenospheres. *Composites, 11* (4), 288–293.
16. Gupta, N. (2007). A Functionally Graded Syntactic Foam Material for High Energy Absorption under Compression. *Materials Letters*, *61* (4–5), 979–982. https://doi.org/10.1016/j.matlet.2006.06.033
17. Gupta, N. (2006). Hollow Particle Filled Composites. *TMS Annual Meeting*, *2006*, 3–13. http://www.scopus.com/inward/record.url?eid=2-s2.0-33646503473&partnerID=tZOtx3y1
18. Lin, T. C., Gupta, N., & Talalayev, A. (2008). Thermoanalytical Characterization of Epoxy Matrix-Glass Microballoon Syntactic Foams. *Journal of Materials Science*, *44* (6), 1520–1527. https://doi.org/10.1007/s10853-008-3074-3
19. Shao, Y., Jia, D., & Liu, B. (2009). Characterization of Porous Silicon Nitride Ceramics by Pressureless Sintering Using Fly Ash Cenosphere as a Pore-Forming Agent. *Journal of the European Ceramic Society*, *29* (8), 1529–1534. https://doi.org/10.1016/j.jeurceramsoc.2008.09.012
20. Wang, C., Liu, J., Du, H., & Guo, A. (2012). Effect of Fly Ash Cenospheres on the Microstructure and Properties of Silica-Based Composites. *Ceramics International*, *38* (5), 4395–4400. https://doi.org/10.1016/j.ceramint.2012.01.044
21. Ren, S., Tao, X., Ma, X., Liu, J., Du, H., Guo, A., … & Ge, J. (2018). Fabrication of Fly Ash Cenospheres-Hollow Glass Microspheres/Borosilicate Glass Composites for High Temperature Application. *Ceramics International*, *44* (1), 1147–1155. https://doi.org/10.1016/j.ceramint.2017.10.089
22. Ren, S., Tao, X., Xu, X., Guo, A., Liu, J., Fan, J., … & Liang, J. (2018). Preparation and Characteristic of the Fly Ash Cenospheres/Mullite Composite for High-Temperature Application. *Fuel*, *233*, 336–345. https://doi.org/10.1016/j.fuel.2018.06.058
23. Sankaranarayanan, S., Nguyen, Q. B., Shabadi, R., Almajid, A. H., & Gupta, M. (2016). Powder Metallurgy Hollow Fly Ash Cenospheres' Particles Reinforced Magnesium Composites. *Powder Metallurgy*, *59* (3), 188–196. https://doi.org/10.1080/00325899.2016.1139339
24. Luong, D., Lehmhus, D., Gupta, N., Weise, J., & Bayoumi, M. (2016). Structure and Compressive Properties of Invar-Cenosphere Syntactic Foams. *Materials*, *9* (2), 115. https://doi.org/10.3390/ma9020115
25. Weise, J., Lehmhus, D., Baumeister, J., Kun, R., Bayoumi, M., & Busse, M. (2014). Production and Properties of 316L Stainless Steel Cellular Materials and Syntactic Foams. *Steel Research International*, *85* (3), 486–497. https://doi.org/10.1002/srin.201300131

26. Rugele, K., Lehmhus, D., Hussainova, I., Peculevica, J., Lisnanskis, M., & Shishkin, A. (2017). Effect of Fly-Ash Cenospheres on Properties of Clay-Ceramic Syntactic Foams. *Materials*, *10* (7). https://doi.org/10.3390/ma10070828

27. Wang, M.-R., Jia, D.-C., He, P.-G., & Zhou, Y. (2011). Microstructural and Mechanical Characterization of Fly Ash Cenosphere/Metakaolin-Based Geopolymeric Composites. *Ceramics International*, *37* (5), 1661–1666. https://doi.org/10.1016/j.ceramint.2011.02.010

28. Baronins, J., Setina, J., Sahmenko, G., Lagzdina, S., & Shishkin, A. (2015). Pore Distribution and Water Uptake in a Cenosphere-Cement Paste Composite Material. *IOP Conference Series: Materials Science and Engineering*, *96* (1), 012011. https://doi.org/10.1088/1757-899X/96/1/012011

29. Adesina, A. (2020). Sustainable Application of Cenospheres in Cementitious Materials – Overview of Performance. *Developments in the Built Environment*, *4*, 100029. https://doi.org/10.1016/j.dibe.2020.100029

30. Shishkin, A., Mironov, V., Zemchenkov, V., Antonov, M., & Hussainova, I. (2016). Hybrid Syntactic Foams of Metal – Fly Ash Cenosphere – Clay. *Key Engineering Materials*, *674*, 35–40. https://doi.org/10.4028/www.scientific.net/KEM.674.35

31. Tatarinov, A., Shishkin, A., & Mironovs, V. (2019). Correlation between Ultrasound Velocity, Density and Strength in Metal-Ceramic Composites with Added Hollow Spheres. *IOP Conference Series: Materials Science and Engineering*, *660* (1). https://doi.org/10.1088/1757-899X/660/1/012040

32. Irtiseva, K., Lapkovskis, V., Mironovs, V., Ozolins, J., Thakur, V. K., Goel, G., … & Shishkin, A. (2021). Towards Next-Generation Sustainable Composites Made of Recycled Rubber, Cenospheres, and Biobinder. *Polymers*, *13* (4), 574. https://doi.org/10.3390/polym13040574

33. Shishkin, A., Drozdova, M., Kozlov, V., Hussainova, I., & Lehmhus, D. (2017). Vibration-Assisted Sputter Coating of Cenospheres: A New Approach for Realizing Cu-Based Metal Matrix Syntactic Foams. *Metals*, *7* (1), 16. https://doi.org/10.3390/met7010016

34. Shishkin, A., Drozdova, M., Kozlov, V., Hussainova, I., & Lehmhus, D. (2017). Vibration-Assisted Sputter Coating of Cenospheres: A New Approach for Realizing Cu-Based Metal Matrix Syntactic Foams. *Metals*, *7* (1). https://doi.org/10.3390/met7010016

35. Dudina, D. V., Bokhonov, B. B., & Olevsky, E. A. (2019). Fabrication of Porous Materials by Spark Plasma Sintering: A Review. *Materials*, *12* (3). MDPI AG. https://doi.org/10.3390/ma12030541

36. Saheb, N., Iqbal, Z., Khalil, A., Hakeem, A. S., Al Aqeeli, N., Laoui, T., … & Kirchner, R. (2012). Spark Plasma Sintering of Metals and Metal Matrix Nanocomposites: A Review. *Journal of Nanomaterials*. https://doi.org/10.1155/2012/983470

37. Tokita, M. (2021). Progress of Spark Plasma Sintering (SPS) Method, Systems, Ceramics Applications and Industrialization. *Ceramics*, *4* (2). https://doi.org/10.3390/ceramics4020014

38. Weise, J., Lehmhus, D., Baumeister, J., Kun, R., Bayoumi, M., & Busse, M. (2014). Production and Properties of 316l Stainless Steel Cellular Materials and Syntactic Foams. *Steel Research International*, *85* (3). https://doi.org/10.1002/srin.201300131

39. Peroni, L., Scapin, M., Lehmhus, D., Baumeister, J., Busse, M., Avalle, M., & Weise, J. (2017). High Strain Rate Tensile and Compressive Testing and Performance of Mesoporous Invar (FeNi36) Matrix Syntactic Foams Produced by Feedstock Extrusion. *Advanced Engineering Materials*, *19* (11). https://doi.org/10.1002/adem.201600474

40. Klymenko, V. M. (2019). Spark Plasma Sintering of Porous Materials Made of 1Kh18N9T Corrosion-Resistant Steel Fibers. *Powder Metallurgy and Metal Ceramics*, *58* (1–2), 23–28. https://doi.org/10.1007/s11106-019-00043-6

41. Manukyan, K. V., Yeghishyan, A. V., Shuck, C. E., Moskovskikh, D. O., Rouvimov, S., Wolf, E. E., & Mukasyan, A. S. (2018). Mesoporous Metal - Silica Materials: Synthesis, Catalytic and Thermal Properties. *Microporous and Mesoporous Materials*, *257*. https://doi.org/10.1016/j.micromeso.2017.08.044
42. Vassilev, S. V., Menendez, R., Diaz-Somoano, M., & Martinez-Tarazona, M. R. (2004). Phase-Mineral and Chemical Composition of Coal Fly Ashes as a Basis for their Multicomponent Utilization. 2. Characterization of Ceramic Cenosphere and Salt Concentrates. *Fuel*, *83* (4–5), 585–603. https://doi.org/10.1016/J.FUEL.2003.10.003
43. Jung, J., Kim, S. H., Kang, J. H., Park, J., Kim, W. K., Lim, C. Y., & Park, Y. H. (2022). Compressive Strength Modeling and Validation of Cenosphere-Reinforced Aluminum–Magnesium-Matrix-Based Syntactic Foams. *Materials Science and Engineering A*, *849*. https://doi.org/10.1016/j.msea.2022.143452
44. Yu, J., Li, X., Fleming, D., Meng, Z., Wang, D., & Tahmasebi, A. (2012). Analysis on Characteristics of Fly Ash from Coal Fired Power Stations. *Energy Procedia*, *17*, 3–9. https://doi.org/10.1016/j.egypro.2012.02.054
45. Yoriya, S., Intana, T., & Tepsri, P. (2019). Separation of Cenospheres from Lignite Fly Ash Using Acetone-Water Mixture. *Applied Sciences (Switzerland)*, *9* (18). https://doi.org/10.3390/app9183792
46. Jiang, F., Zhang, L., Mukiza, E., Qi, Z., & Cang, D. (2018). Formation Mechanism of High Apparent Porosity Ceramics Prepared from Fly Ash Cenosphere. *Journal of Alloys and Compounds*, *749*, 750–757. https://doi.org/10.1016/j.jallcom.2018.03.303
47. Rugele, K., Lehmhus, D., Hussainova, I., Peculevica, J., Lisnanskis, M., & Shishkin, A. (2017). Effect of Fly-Ash Cenospheres on Properties of Clay-Ceramic Syntactic Foams. *Materials*, *10* (7). https://doi.org/10.3390/ma10070828
48. Nithyanandam, A., & Deivarajan, T. (2021). Development of Fly Ash Cenosphere-Based Composite for Thermal Insulation Application. *International Journal of Applied Ceramic Technology*, *18* (5), 1825–1831. https://doi.org/10.1111/ijac.13767
49. Kristombu Baduge, S., Mendis, P., San Nicolas, R., Nguyen, K., & Hajimohammadi, A. (2019). Performance of Lightweight Hemp Concrete with Alkali-Activated Cenosphere Binders Exposed to Elevated Temperature. *Construction and Building Materials*, *224*, 158–172. https://doi.org/10.1016/j.conbuildmat.2019.07.069
50. Kolay, P. K., & Singh, D. N. (2001). Physical, Chemical, Mineralogical, and Thermal Properties of Cenospheres from an Ash Lagoon. *Cement and Concrete Research, 31*, 539– 542.
51. Anshits, N. N., Mikhailova, O. A., Salanov, A. N., & Anshits, A. G. (2010). Chemical Composition and Structure of the Shell of Fly Ash Non-Perforated Cenospheres Produced from the Combustion of the Kuznetsk Coal (Russia). *Fuel*, *89* (8), 1849–1862. https://doi.org/10.1016/j.fuel.2010.03.049
52. Patel, S. K., Majhi, R. K., Satpathy, H. P., & Nayak, A. N. (2019). Durability and Microstructural Properties of Lightweight Concrete Manufactured with Fly Ash Cenosphere and Sintered Fly Ash Aggregate. *Construction and Building Materials*, *226*, 579–590. https://doi.org/10.1016/j.conbuildmat.2019.07.304

sciendo

LATVIAN JOURNAL OF PHYSICS
AND TECHNICAL SCIENCES
2024, N 4

DOI: 10.2478/lpts-2024-0027

CHARACTERISATION OF HYBRID PHOTODETECTOR SIGNALS FOR SATELLITE LASER RANGING APPLICATION

K. Salmins*, J. Kaulins

Institute of Astronomy, University of Latvia,
3 Jelgavas Str., Riga, LV-1004, LATVIA
*e-mail: kalvis.salmins@lu.lv

The hybrid photodetector (HPD) is a photomultiplier tube combined with the semiconductor device within the vacuum. The photoelectrons emitted from the photocathode directly hit the semiconductor enabling efficient electron multiplication with low noise and symmetric output pulse. These properties make a hybrid photodetector a good solution for photon-counting applications. At the Satellite Laser Ranging Station of the Institute of Astronomy at the University of Latvia, the hybrid photodetector characteristics were evaluated for SLR applications, including multiphoton mode and time-walk compensation.

Keywords: *Photodetectors, satellite laser ranging, time walk.*

1. INTRODUCTION

Satellite Laser Ranging (SLR) is a space geodesy technique that measures distances to the satellites by sending short laser pulses to the satellite, detecting reflected photons, and measuring the round-trip time with extremely high accuracy. SLR uses several different types of detector that capture the reflected light from the target. The basic criteria for the detector for SLR are a single-photon sensitivity, picosecond level timing resolution, high quantum efficiency at applicable wavelength, low dark noise, and time-walk characteristics. Time walk is an amplitude and signal rise time-dependent shift in the timing measurements. SLR typically uses a 532 nm laser wavelength, but for certain tasks, particularly for the space debris ranging, a wavelength of 1064 nm is also used. The most widely used detectors are Photomultiplier Tube (PMT), Multi-Channel Plates (MCP), and Compensated Single Photon Avalanche Diode (CSPAD). The main difference between CSPAD and Single Photon Avalanche Diode (SPAD) is

a time-walk compensation electronics built into the CSPAD. Recently, a superconducting nanowire (SNSPD) operating at wavelength of 1064 nm has also been tested. Another potential detector type is a silicon photomultiplier (SiPM).

Each of these detectors has its own advantages and disadvantages in SLR applications. PMT typically has a large-area photocathode, which makes it easy to install and align, and cause relatively low dark noise. This type of detector has been known for almost 100 years, the technologies involved are well researched and widely used in different applications, including SLR. It is characterised by a relatively small quantum efficiency of 10–35 % depending on the photocathode type and a typically lower timing resolution at the single-photon level than other detector types now used in SLR. Higher quantum efficiency in the case of PMT also results in a lower timing resolution mostly due to the photocathode thickness [1].

CSPAD type detectors now are widely used in SLR in the single-photon detection mode. Detectors of this type have a better time resolution, less than 100 ps, and quantum efficiency, reaching up to 60 %. CSPAD detectors have a built-in diode cooling down to -60 °C to reduce noise and time-walk compensating electronics (time walk is also a function of temperature). The small size of the sensitive area (0.05mm–0.2mm) complicates the alignment of the system and requires high accuracy and stability for satellite pointing and tracking.

Superconducting nanowire detectors (SNSPDs) have even higher quantum efficiency, in some cases approaching 100 %, and have very low dark noise, but the sensing element dimensions are similar to SPADs or smaller and detector operation requires cryogenic temperatures, which complicates setup. Therefore, their use in SLRs currently is limited at the experimental level.

Multi-Channel Plate (MCP), which is a variation of the PMT, offers high QE, has a timing resolution and quantum efficiency comparable to CSPAD. Due to it is design, it is hard to detect if the system operates in a single- or multiphoton mode. This knowledge is important for the signal processing and later analysis.

In this paper, we will review some of the characteristics of hybrid photodetector (HPD). The hybrid photodetector combines the characteristics of PMT and SPAD. It has applications in nuclear physics experiments, fluorescence spectroscopy, fluorescence microscopy, optical tomography, and photon counting applications with high time-resolution requirements. However, to the best of our knowledge, so far it has not been used in regular SLR operations, although it was indicated as a prospective SLR detector as early as 2014 [2]. While HPD performance in a single or few-photon mode is known, its performance and timing properties, when the signal varies from single photon to mulitphoton reaching hundreds of photon per pulse, as in the case of SLR station in Riga, are unknown.

In the hybrid detector, the output signal is formed in three stages. First, photon-to-electron conversion takes place, which generally corresponds to the classical photocathode (d = 3–6 mm) with an operating voltage of -8 kV. Electrons accelerate in a vacuum over a distance of a few millimetres and their number multiplies when the electron hits the semiconductor surface (amplification approx. 1500). After that, these electrons reach a p-n junction operated in avalanche mode (UR = +390V), where another 80-fold amplification is obtained. The key difference from the PMT is that there are no multiple dynodes. As a result, HPD has a good amplitude resolution but

a low output signal amplitude. The market offers ready-made modules that combine the photosensor itself with a cooler, a high-speed preamplifier and a power supply unit [3]–[5]. All these modules use the family of HPD modules from Hamamatsu [6].

The small spatial dimension of the physical processes taking place in the sensor allows for obtaining a very short output signal, for some models the FWHM is less than 18 ps. The noise level depends on the photocathode type and size, ranging from less than 100 cps up to a few thousand cps. For our selected model, PicoQuant PMA-40 with GaAsP photocathode, measured dark count is less than 100 cps with trigger level set at -50 mV.

2. EXPERIMENTAL

The primary intended use of the HPD in our case was for the space debris laser ranging, but we also evaluated its eventual application in SLR where timing accuracy is paramount. Therefore, we decided to check whether the detector could also be used for the SLR needs, as there were no published data available, with particular interest in the detector time-walk characteristics and detector performance with multi-photon signals.

The existing detector unit of laser ranging telescope LS-105 was modified to accommodate the second detector. New design allows working with both detectors – PMT, Hamamatsu H11901 and HPD PicoQuant PMA-40. Detector unit layout is demonstrated in Fig. 1. The detector unit makes it easy to switch between both detectors as needed. All optomechanical components of the detector, including switching detector channels, can be controlled remotely from the operator's computer. The main parameters of both detectors used, as provided by the manufacturers, are presented in Table 1.

Table 1. Detector Parameters

Parameter	**PMT Hamamatsu H11901-20**	**HPD PicoQuant PMA-40 [5]**
QE_{max} at 532 nm, %	18	44
Spectral band at QE>10 %, nm	300–850	300–720
Size of the sensitive area, mm	8	3
Dark count, Hz	600–1000	<80
$F_{count., max}$, MHz	≈200	80 (10 recommended)
Rise time, ps	570	400

The focal diaphragm F defines the detector field of view and is positioned in the focal plane of the main optical system.

To evaluate signal parameters, we used an internal calibration chain, shown in Fig. 2. Internal calibration uses variable attenuator to reduce laser pulse to the strength comparable with the returned signal from the satellite allowing one to simulate signals from single photoelectron to hundreds of photoelectrons. The attenuated laser pulse is redirected via optical fibre into the receiver channel. We use this setup to make an assessment of the HPD parameters. The laser is Ekspla SL-312. For the SLR operations and detector testing laser pulse energy is set to 100 mJ at a wavelength of 532 nm, pulse length FWHM is 130 ps.

The outgoing laser pulse is split into two parts by a dielectric mirror, directing the main part of the signal to the main telescope optics and, accordingly, to the satellite or corner cube retroreflector if the external calibration is performed. External calibration takes place by installing a retroreflector at the exit of the telescope tube or on one of the external target piers near the telescope.

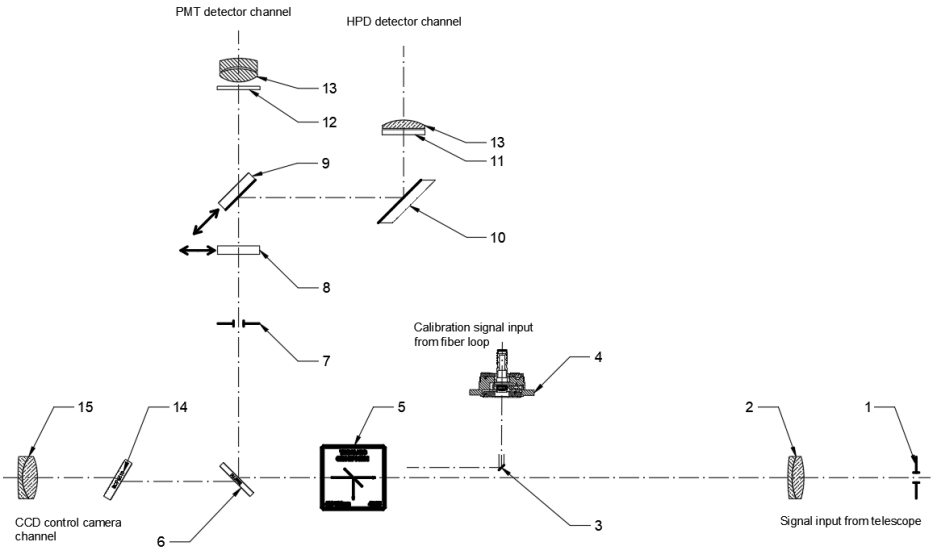

Fig. 1. Multi-channel detector unit using HPD and PMT: an optical scheme.

1 – input (focal) diaphragm, 2 – collimator lens, 3 – reflective prism, 4 – fibre port, 5 – pellicle beamsplitter (removable, for adjustment only), 6 –540 nm longpass dichroic mirror, 7 – diaphragm-attenuator, 8 – 0.15 nm ultra-narrow band interference filter (optional), 9 – movable diagonal mirror for channel switching, 10 – diagonal mirror, 11, 12 – 2 nm narrow band interference filters, 13 – detector lenses, 14 – compensator plate, 15 – alignment control camera lens.

The signal coming from the laser falls on the Nd:YAG laser line dielectric mirror for the 532 nm line of the second harmonic of the Nd-YAG laser. Most of the signal enters the telescope, which redirects it to the target. Approximately 0.3–0.4 % of the light passes through the dielectric mirror and forms the measurement start and calibration signals. The signal is further attenuated by the neutral filter before entering the beam splitter. The start signal is generated by a high-speed photodiode, the signal of which is inverted to suit the input of the constant fraction discriminator (CFD). From the CFD, the signal is fed to the ET input, which is also the real start signal to start the time interval measurement. In internal calibration mode, shutter 1 is closed and shutter 2 is open. The straight part of the beam passes through an adjustable optical attenuator (see Fig. 2), which consists of rotating linear polarizers.

Behind them, the beam enters the single mode optical fibre with a precisely known length of 25.008 m, the other end of which is located in the detector block (see Fig. 1). The calibration mode is necessary to determine the system delay times and to obtain the signal amplitude correction curve by changing the optical attenuation. This setup can also be used to evaluate detector and measurement electronics.

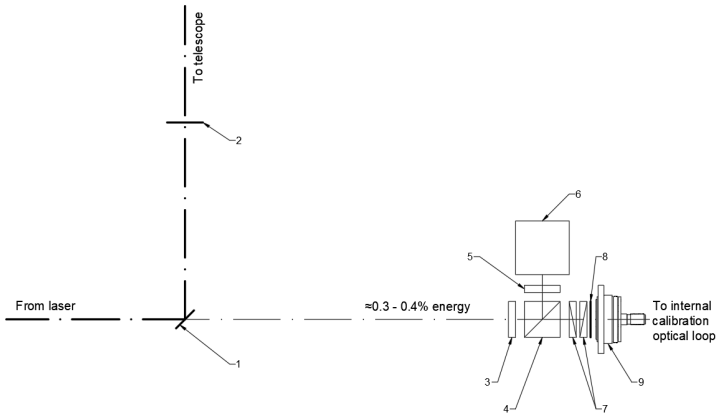

Fig. 2. Variable attenuator for internal calibration.

1 – Md:YAG laser line mirror 532 nm, 2 – shutter 1, 3 and 5 – neutral filters, 4 – beamsplitter, 6 – start signal diode, 7 – the pair of polarizers (variable attenuator), 8 – shutter 2, 9 – fibre port.

The HPD module contains a built-in preamplifier, but the PMT uses a high-speed external Hamamatsu C5658 preamplifier. The detector lens focuses light on the photocathodes to minimize the transit time spread (TTS) influence. The preamplifiers are connected to the signal processing devices by low-loss delay cables to compensate event timer RTS 2006 dead-time, which is 90 ns. The time selector is located on the input of the time selector/amplitude-to-interval-converter (TS/ATIC) [7] input of the signal pre-processing unit and is driven by the gate signal from the event timer RTS 2006 [8]. TS/ATIC operates as a leading edge discriminator and converts each incoming pulse to the pair of NIM logic signals. The first pulse gives time interval measurement, the second pulse serves as time interval measurement. The time interval between the TS/ATIC output pulses is directly proportional to the amplitude of the signal. This time interval serves as information for signal amplitude compensation using the calibration curve to compensate for detector time walk. Time-walk compensation is performed in the post-processing software.

The block diagram of the hardware is shown in Fig. 3. The diagram also shows the places where signal parameters are measured. For this purpose, a Tektronix DPO7254 oscillograph with a bandwidth of 2.5 GHz was used.

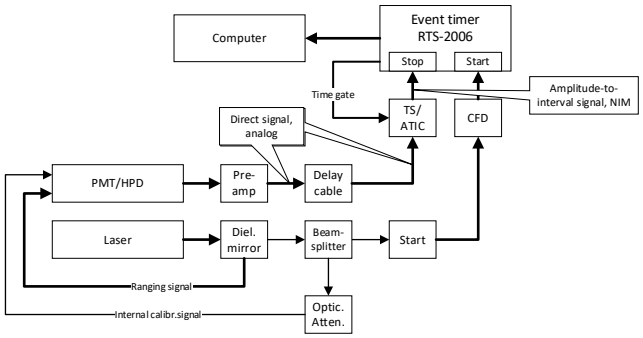

Fig. 3. Ranging and internal calibration scheme.

TS/ATIC – Time Selector and Amplitude – Time Converter. Note: PMT and HPD each have a separate individually tuned TS/ATIC unit.

2.1. Time-Walk Measurements

Time-walk measurements for the HPD are shown in Fig. 4. For the comparison, the time-walk chart for the PMT is shown in Fig. 5. The measurements are obtained by periodically changing laser pulse strength with attenuator in the calibration loop in the full range from the minimal to the maximal available value. The signal waveforms were checked with the Tektronix DPO 7254C at different amplitude values to check when the waveform becomes distorted and unusable for the measurement of the signal amplitude with TS/ATIC. Single photon mode was controlled by monitoring a return rate. When the return rate is 10 % or less, we assume that we have a single-photon mode. Independently it was verified by checking the signal waveform with an oscilloscope. Each time-walk measurement set contains 6000 data points. Each data point includes measurement epoch, measured distance in picoseconds, and amplitude expressed in nanoseconds. Experiments show that the HPD dynamic range is approximately 20 % smaller than that of PMT.

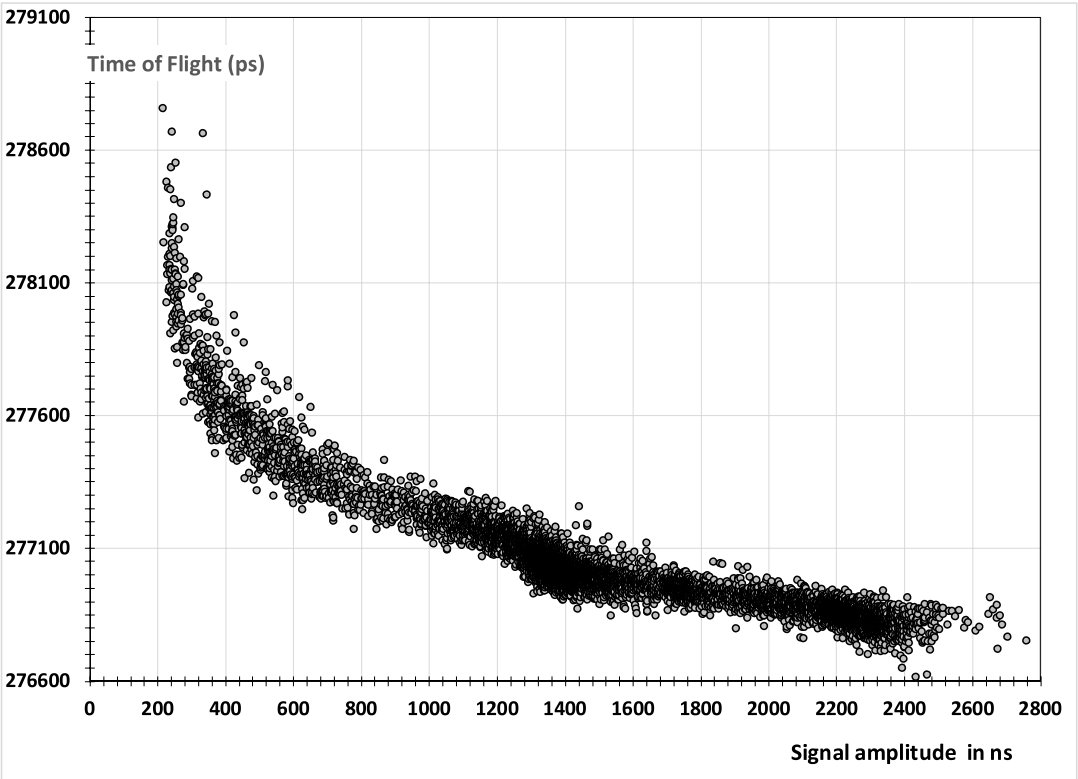

Fig. 4. HPD time walk. The x-axis is the signal amplitude converted to the time interval in ns, and the Y-axis denotes the calibration loop total length in ps.

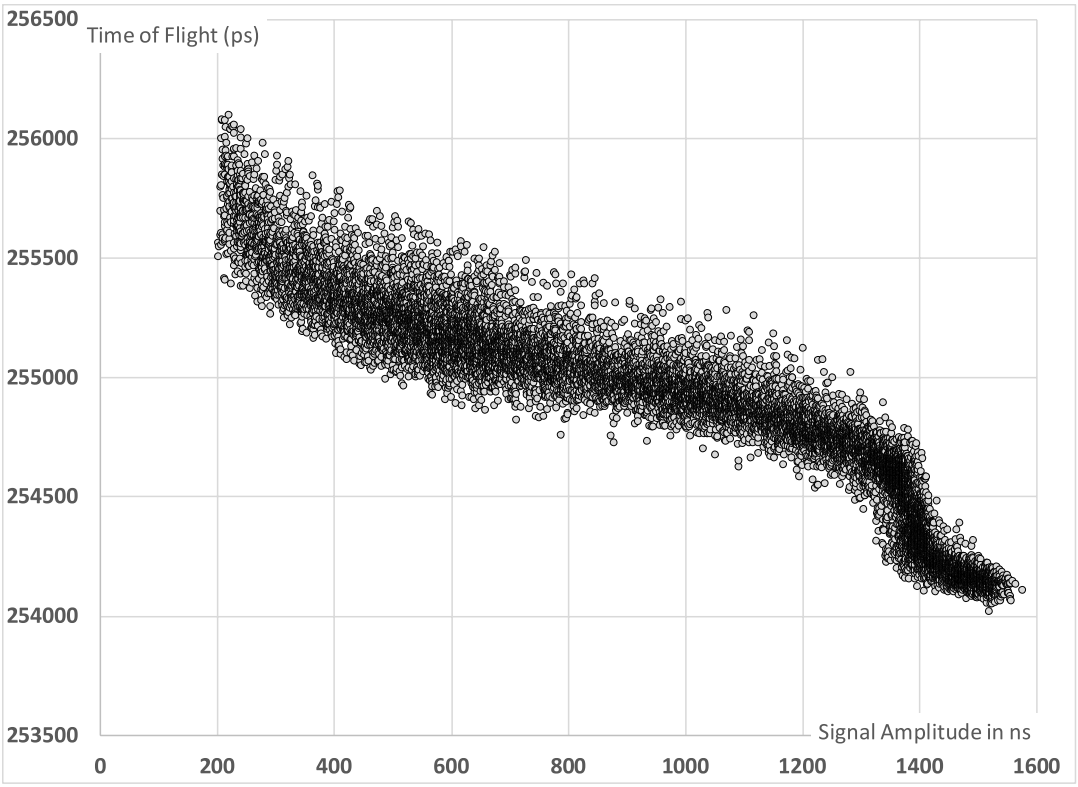

Fig. 5. PMT time walk. The x-axis is the signal amplitude converted to the time interval in ns, and the Y-axis denotes the calibration loop total length in ps.

The difference in distance measurements between HPD and PMT is caused by the geometric difference in optical path length between the HPD and PMT locations in the detector unit. At a fixed amplitude, charts indicate measurement uncertainty, which is a sum from the detector TTS, laser pulse width, and summary measurement error, including all electronics. The correction uncertainty for HPD is smaller reflecting a smaller TTS value.

3. CONCLUSIONS

In the single-photon operating mode, a good correspondence of the pulse shape and amplitude was observed with that found in the detector manufacturer's documentation. In the single to a few photon mode amplitude changes are proportional to the number of photons and maintaining this proportionality up to approximately 5–6 photons per pulse. When the pulse amplitude reaches 1200 mV–1250 mV, a signal becomes unusable for the precise amplitude measurements and time-walk compensation. It should be noted that the signal still can be used to measure distances, but the result will be with a lower accuracy due to uncertainties in the amplitude measurements induced

by the signal waveform distortion.

HPD seems to be a viable alternative in SLR applications to the already existing types of photodetectors, with the following remarks. For daylight tracking, an alkali type with a lower quantum efficiency should be chosen to improve a life time and timing resolution. 10 %–15 % QE should be sufficient for the cooperative target tracking. The alkali photocathode types also offer a better time resolution TTS <50s compared to 120 ps for the high sensitivity GaAsP photocathode used in our experiments. We measured the time-walk characteristics of the HPD detector and found the usable amplitude interval. The dynamic range is lower than PMT due to higher QE but this raises the issue only with a very strong multiphoton. To achieve the best accuracy, we have to discard multiphoton signals outside the usable range. Experiments show that the time-walk compensation algorithm using leading edge discriminator works well with HPD using the same approach as PMT in actual SLR experiments [9]. For the space debris laser ranging HPD detector version with the high QE, where the timing accuracy is less demanding, HPD with its larger sensitive area and low noise can be considered a cost effective alternative to CSPAD or MCP detector types. To make time-walk compensation measurements more accurate, especially in one to a few photon mode, more precise optical laser pulse attenuation control is required and existing setup has to be modified to make optical attenuation more precise and repeatable.

ACKNOWLEDGEMENTS

The study has been supported by the ERDF funded project "Technology for High-Precision Time-Amplitude Analysis of Event Flow" (TIME AMP) No. 1.1.1.1/20/A/076.

REFERENCES

1. Taguchi, T., & Nakamura, M. (2013). New Gated MCP-PMTs and their Performances in Comparison with Semiconductor Type Detectors for SLR Applications. *International Workshop on Laser Ranging, 3-Po28*. Available at https://ilrs.gsfc.nasa.gov/lw18/docs/papers/Posters/13-Po28-Taguchi.pdf
2. Sadovnikov, M. A., & Shargorodskiy, V. D. (2014). The New Generation SLR Station for Time Transfer with the Subnanosecond Accuracy and Laser Ranging with the Submillimeter Accuracy in the Daytime and at Night. 19th International Workshop on Laser Ranging 2014 Annapolis, USA, Annapolis, USA. Available at https://cddis.nasa.gov/lw19/docs/2014/Presentations/3025_Sadovnikov_presentation.pdf
3. Edinburgh Instruments. (n.d.). *High-Speed Hybrid Photodetector (HS-HPD).* Available at https://www.edinst.com/us/high-speed-hybrid-photodetector-hs-hpd/
4. Becker & Hickl GmbH (n.d.). *Hybrid Single-Photon Detectors*. Available at https://www.becker-hickl.com/products/hybrid-photo-detectors/
5. PicoQuant. (n.d.). *PMA Hybrid Series Hybrid Photomultiplier Detector Assembly.* Available at https://www.picoquant.com/products/category/photon-counting-detectors/pma-hybrid-series-hybrid-photomultiplier-detector-assembly#documents

6. Hamamatsu Photonics. (n.d.). *Hybrid Photo Detectors (HPDs)*. Available at https://www.hamamatsu.com/eu/en/product/optical-sensors/pmt/hpd.html
7. Bespal'ko, V., Burak, I., & Salmins, K. (2019). Estimating the Precision of a Leading-Edge Discriminator with Amplitude Correction. *Instruments and Experimental Techniques, 62* (6), 788–793. https://doi.org/10.1134/S0020441219060022
8. Artyukh, Y., Bespal'ko, V., Lapushka, K., & Rybakov, A. (2006). Event timing system for Riga SLR station. In *Proceedings of the 15th International Workshop on Laser Ranging*. 16–20 October 2006, Canberra, Australia. http://edi.lv/media/uploads/UserFiles/event_timing/Publication/EventTimingSystem4Riga.pd
9. Salmins, K., del Pino, J., & Kaulins, J. (2023). Hybrid Photodetector as Sensor for SLR: First Results. In *23rd International Workshop on Laser Ranging*, held virtually, 16 October 2023. https://ilrs.gsfc.nasa.gov/lw23/Program/index.html#sess02

sciendo

LATVIAN JOURNAL OF PHYSICS
AND TECHNICAL SCIENCES
2024, N 4

DOI: 10.2478/lpts-2024-0028

EXPERIMENTAL STUDY OF A SOLAR TRIGENERATION SYSTEM PROTOTYPE

A. Snegirjovs*, G. Klavs

Institute of Physical Energetics,
14 Dzerbenes Str., Riga, LV-1006, LATVIA
*e-mail: dr.snegirjovs@gmail.com

A prototype solar trigeneration system was built in a new private single-family residential house for experimental purposes. The prototype system was designed to supply the building with the required thermal energy and cooling to a full extent. In addition, one of the conditions is that the thermal and the electrical energy generated by the solar systems should be used for the needs of the building to a maximum extent. The prototype system provides an opportunity to recover thermal energy both during the heating and the cooling season.

This article describes the prototype configuration, the first results of testing, analysis of the results obtained, and the operational features and shortcomings of the open system, as well as the possibilities for its improvement.

Keywords: *Prototype system, single-family residential houses, solar trigeneration.*

1. INTRODUCTION

The information available on electrically operated solar trigeneration systems (S3G) is limited. International literature mainly provides information on the Building Integrated Management (BIM) system descriptions of large office or factory buildings. However, even in these descriptions, there are only general references to the algorithmic management and operational routines without an in-depth analysis. On the other hand, information on the use of S3G for private houses is scarcely available. Literature describes visions of the potential existence of equivalent systems and the smart management they require. At the start of this study, it has been clear that separately operated heating, cooling and electricity systems are widely used in households, but they have weak connectivity: the separate systems operate completely independently of each other, excluding the possibility to optimize the energy supply. Consequently, the aim of the study is to combine the separate heat supply, cooling, electricity con-

sumption and solar photovoltaic systems into a single S3G system with a common control unit. Solar inverter manufacturers tend to think in terms of taking into account the yield of solar electrical energy and the consumer demand for electricity. It can be assumed that this is mainly about controlling the large power-consuming devices, like switching on the washing machine, or charging electric cars, or switching on electric heaters. An in-depth study of such control systems shows that they function on a fairly primitive level. Producers are aware of this behaviour and are actively working on improvements.

Smart control units are becoming increasingly prevalent, primarily, to make sure that electricity storage accumulators are charged during the off-peak hours when the market prices of electricity are low and that the accumulators are discharged when the prices on electricity are high. Some experimental systems are able to take into account connection to a solar power plant. As shown by experience, the control algorithm of such systems tends not to be openly published, and, unfortunately, these control units are not very widespread globally.

There is, certainly, a lot of interest in S3G systems on the part of solar energy researchers and engineers. This study analyses S3G technology, which uses low-power components to meet the domestic heating, cooling and electricity needs of single family homes by using solar and geothermal energy. The public grid is used to compensate for insufficient electricity and to transport excess electricity. One of the aims of the study is to achieve minimum electricity import for household use.

2. METHODOLOGY

The main sources of energy in this household energy supply system are solar energy and geothermal heat. The main components of the system are: flat vacuum solar collectors with a total capacity of 11.5 kW, a 13kW heat pump, a ventilation installation unit with a recuperator and air conditioning units; two accumulating heat storage tanks: a heat storage tank with an actual volume of 0.788 m^3, and a low temperature (up to 25 ºC) heat storage tank; solar photovoltaic panels 32 pcs. at 405 W each, 12.96 kW in total; and an 11.1 kW inverter, 3 phases, 16A; several control units based on Technea Alternative and additional Siemens components combined in a single control system. The system was equipped with the sensors required for controlling the system itself and additional sensors for the in-depth study of the system operation.

The prototype system was installed in a private residential house. The house was already equipped with a heat pump system. The additional installations were: solar collectors, a free cooling unit, solar panels and and an inverter, and automated control. The prototype system was equipped with numerous performance sensors, providing for the required aggregation of system performance indicators for further analysis.

The private house is a 2-storey building with a heated area of 200 m^2. The building is well insulated: the walls are built from aerated concrete blocks with mineral wool thermal insulation, the attic and the roof are separated from the structure and insulated with mineral wool, the windows have triple glazing, and the entrance door is a double door. Thus, the building has low specific heat consumption amounting to 36.6 kwh/m^2/per year.

The building has warm floor heating

and heat ventilation. Heat accumulation takes place both in the main/basic storage tank (filled with technical water) and in an additional storage tank (filled with a mixture of bioethanol with a freezing point down to -17 °C). The basic storage tank serves as a heat accumulation and distribution unit. The upper part of the storage tank is intended for household hot-water preparation and is maintained at a temperature above +50 °C; the middle part is intended for heating and it is maintained at a temperature that exceeds the temperature required for heating by a few degrees; the bottom part is intended for preheating hot water with the heat generated by solar collectors.

3. RESULT AND DISCUSSION

At the pre-design stage of the S3G system, the system was modelled with Polysun software, including simulation. The types of the system components, and their basic parameters, and sizes were selected through multiple modelling iterations. In each iteration, one of the basic elements was changed by one step in size with due regard to the sizes of the equipment widely available on the market. The components were optimized with the purpose of minimizing the amount of imported electricity (from the grid). In the next step (re-optimization), the entire optimization process was repeated. In total, we performed one base optimization and three re-optimizations. The difference in the amount of imported electricity as a result of the second and third re-optimization was 0.4 %. This leads to a conclusion that further re-optimization would hardly result in a significant reduction of imported electricity. On the other hand, real-world testing of the prototype and the results obtained showed that there was room for improving the control algorithm.

The prototype system is equipped with flat vacuum solar collectors. Flat vacuum solar collectors do not have mineral thermal insulation, and reduction of heat loss is ensured with air expanded almost to vacuum. Such solar collectors can also operate in a low temperature range without condensation and without corrosion in the solar collectors themselves. With sufficient solar radiation, the solar collectors heat up the storage tank through two snake-shaped solar heat exchangers in the basic storage tank. If the temperature in the solar collectors is higher than the temperature in the upper part of the basic storage tank, a 3-way control valve diverts the heat for heating, initially, through the upper solar heat exchanger and, next, through the lower solar heat exchanger. Thus, the accumulating heat storage tank gets the maximum amount of heat while maintaining the heat stratification in the tank. If the temperature of the solar collectors is lower than the temperature in the upper part of the accumulating heat storage tank but higher than the temperature in the bottom part of the storage tank, the heat transfer fluid from the solar collectors is transferred only to the lower heat exchanger of the basic storage tank. Thus, the upper part of the accumulating tank is not cooled. On the other hand, if there is insufficient solar radiation, the heat produced by the solar collectors is transferred to the additional storage tank. In the solar collector circuit, the heat transfer fluid is monopropylene glycol for solar systems, while in the additional storage tank, the heat transfer fluid is the same as in the ground circuit, i.e., a mixture of bioethanol. Therefore, the transfer of heat from the solar circuit to the additional storage tank

also takes place through a heat exchanger. The heat transfer fluid from the additional storage tank is mixed with the heat transfer fluid from the ground circuit and is transferred to the heat pump.

The heat pump in the building works with variable capacity: the heat capacity is in the range of 2.5 kW to 13 kW. The heat pump produces heat for both heating and hot water preparation. The heat pump, using the heat transfer fluid from the additional storage tank (in the temperature range from 5 °C to 25 °C), brings up the temperature of the heat transfer fluid in the heating circuit (from 30 °C to 55 °C) and goes on to heat the basic storage tank, from where the heat is redirected to be consumed by the building. Due to the installed heat recovery hydrounit, it was possible to use the heat energy obtained from indoor air for hot water preparation by increasing the heat transfer fluid temperature with the help of the heat pump.

The free cooling unit, on the other hand, permitted transfer of excess energy into the ground circuit. The heat transferred to the ground circuit is more than sufficient for ensuring the cooling capacity of the building, and no additional cold generation or refrigeration equipment is required. When using the free cooling mode, with energy transferred to the ground, operation of the heat pump is not required. This results in significant energy savings.

The basic heating takes place through the warm floors, and fresh air is fed into the building through the ventilation installation. The ventilation installation is equipped with an air recuperator, a low-temperature heat unit and a cooling unit. Heat is transferred to the ventilation unit from the middle part of the basic storage tank. The cooling unit is connected to the ground circuit through the free cooling unit.

Fig. 1. Solar collectors and photovoltaic panels on the roof of the building.

Fig. 2. Prototype heat generation and heat distribution unit.

Fig. 3. Solar inverter and control unit.

Before handing over the prototype for autonomous operation, the control algorithm was adapted to the energy consumption. The S3G simulation and prototype performance parameters were compared and calibrated. From the very first months of testing, data showed that heat, hot water and electricity consumption depended significantly on a variety of factors, including consumer behaviour.

The lifestyle of the residents of the particular house includes long holidays and events with a large number of guests. Such a lifestyle has a significant impact on energy consumption. In particular, the two heat storage tanks are able to stabilize hot water consumption. On the other hand, fluctuations in electricity consumption had a significant impact on the amount of electricity imported from the grid and transferred to the grid.

The prototype system was tested for over a year. This is certainly not long enough for testing prototypes and obtaining in-depth results. Such a study would take several years, but in our case that would exceed the duration of the research project.

The data obtained as a result of the testing were checked, filtered from errors, and aggregated. For easier reading, they were aggregated and reflected in an energy consumption distribution schedule by month and by service types (see Fig. 2).

Since the prototype testing took place in the Baltic region, there is a clear difference in the type and amount of energy consumption during the winter and summer seasons. As a result, the S3G system operates in completely different modes during these seasons.

In the cold winter months, the consumption of thermal energy is significantly higher. The system operates in the heating mode almost without interruptions. Thanks to the heat pump ability to operate with variable capacity, heat production is sufficiently efficient. Thanks to heat storage tanks, which act both for heat stratification and as heat energy buffers, they are generally able to reduce the peaks in heat consumption.

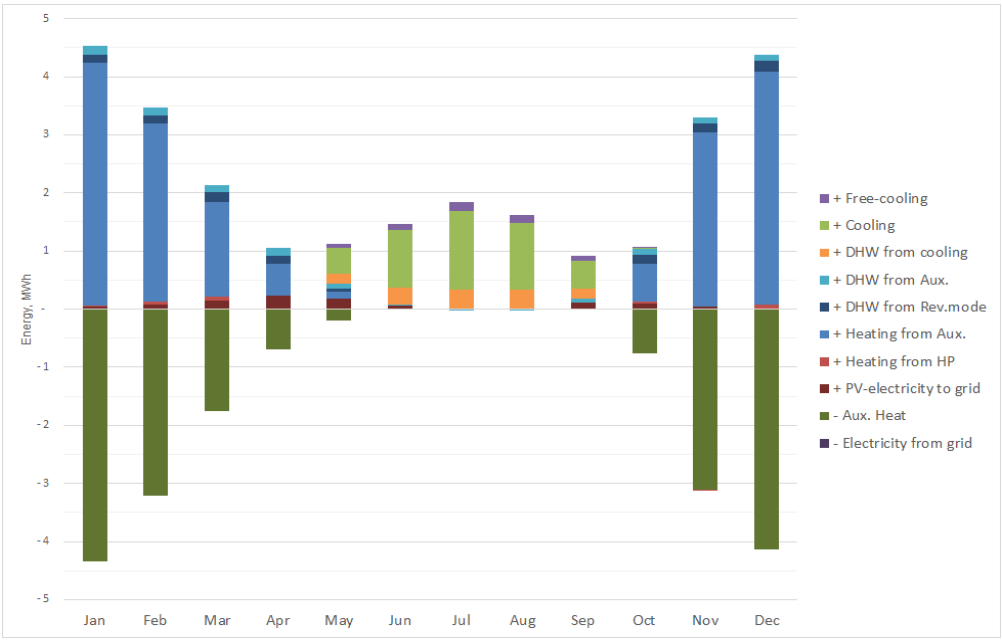

Fig. 4. Distribution of energy consumption in solar trigeneration systems by month.

Running the prototype in real-world conditions showed that hot water consumption peaks could be significant, especially for a family of four who all tend to take their shower on a daily basis during the evening hours. As a result, all the accumulated heat for hot water is spent. At that point, the system switches to high-temperature heating in the nighttime. In this case it is not possible to use solar energy. There are at least three different solutions for optimizing the system. The first option is to use larger accumulating storage tanks for hot water. The disadvantage of such a solution is higher heat loss from a larger storage tank. The second option is to store electricity in batteries, which accumulate the electricity generated by solar PV for later use. There is also the third option – to have a control algorithm for checking and incorporating the weather forecasts for the next day, so that a sunny forecast for the next day would mean the ability to generate enough heat from solar energy for the peak of water consumption on that day. Admittedly, this option is difficult to implement because of the high degree of risk, but this would be a way of maximizing savings in imported energy. If none of the optimization options are implemented, heat can still be produced from cheaper nighttime grid electricity.

4. CONCLUSION

A prototype solar trigeneration system was built in a new private single-family residential house for experimental purposes. The prototype system fully covers needs of house with the required thermal energy and cooling. The thermal and the electrical energy generated by the solar systems is used for the needs of the building to a maximum extent. The prototype system provides an opportunity to recover ther-

mal energy both during the heating and the cooling season. Information about the prototype configuration selection, analysis of the results have been presented in the study. Operational features and shortcomings of the open system, as well as the possibilities for its improvement have been described.

ACKNOWLEDGEMENTS

The research has been worked out by co-financial support of the European Regional Development Fund for post-doctoral project "Solar Trigeneration" No 1.1.1.2./VIAA/3/19/419.

REFERENCES

1. SMA. (2023). *AC/DC Inverter Manufactory – SMA Solar Technology*. Available at www.sma.de
2. Ban-Weiss, G., Wray, C., Ly, P., & Delp, W. (2013). Electricity Production and Cooling Energy Savings from Installation of a Building-Integrated Photovoltaic Roof on an Office Building. *Energy and Buildings, 56*, 210–220.
3. Zehnder Group AG. (2023). *Cooling Ceiling Manufactory*. Available at www.zehnder-systems.com
4. Covenant of Mayors. (2015). *The Emission Factors*, Technical Document. Geneva, Switzerland: The Intergovernmental Panel on Climate Change.
5. European Parliament and of the Council. (2009). *Directive 2009/28/EC of the European Parliament and of the Council of 23 April 2009 on the promotion of the use of energy from renewable sources and amending and subsequently repealing Directives 2001/77/EC and 2003/30/EC.* Official Journal of the European Union, L140/16.
6. Energy Balances of OECD Countries. (2015). Paris, France: International Energy Agency.
7. Fritsche, U. R., & Gress, H. W. (2015). *Development of the Primary Energy Factor of Electricity Generation in the EU-28 from 2010-2013 prepared for the European Heat Pump Association.* Darmstadt, Germany: EHPA.
8. Green, M. A. (2009). The Path to 25 % Silicon Solar Cell Efficiency: History of Silicon Cell Evolution. *Progress in Photovoltaics, 17* (3), 183–189.
9. American Society of Heating, Refrigerating and Air-Conditioning Engineers, Inc. (2008). *Handbook – Heating and Ventilating, and Air-Conditioning Systems and Equipment*. IP Edition. Atlanta, USA.
10. Hening, H. M., Mota, M., & Mugnier, D. (2013). *Solar Cooling Handbook*. Vienna, Austria: Ambra.
11. International Energy Agency, Solar Heating & Cooling Programme. (2023). *Task 53: New Generation Solar Cooling & Heating Systems*. Available at www.task53.iea-shc.org
12. Jakob, U., & Saulich, S. (2008). Development and investigation of solar cooling systems based on small-scale sorption heat pumps. In *1st International Congress on Heating, Cooling and Buildings* (pp. 1–7). Lisbon, Portugal: Eurosun.
13. Kim, M. H., Kim, H., Kim, D. R., & Lee, K.-S. (2016). A Novel Louvered Fin Design to Enhance Thermal and Drainage Performances during Periodic Frosting/Defrosting Conditions. *Energy Conversion and Management, 110*, 494–500.
14. Kühn, A. (2013). *Thermally Driven Heat Pumps for Heating and Cooling*. Berlin, Germany: Universitätsverlag der TU.

15. Kippzonen. (2023). *Manufactory of Measurement Instrument of Solar Radiation.* Available at www.kippzonen.com
16. Masson, G., Orlandi, S., & Rekinger, M. (2014). *Global Market Outlook for Photovoltaics 2014–2018.* Brussels, Belgium: European Photovoltaic Industry Association.
17. Mouchot, A. (1987). *Die Sonnenwärme und ihre industriellen Anwendungen*. Oberbözberg, Switzerland: Olynthus-Verlag.
18. Mugnier, D. (2013). *New Generation Solar Cooling & Heating Systems*. Task Description and Work Plan. IEA Solar Heating & Cooling Program.
19. The International Renewable Energy Agency. (2015). *Renewable Energy Target Setting*. Available at https://www.irena.org/-/media/Files/IRENA/Agency/Publication/2015/IRENA_RE_Target_Setting_2015.pdf
20. European Technology Platform on Renewable Heating and Cooling. (2011*). Common Vision for the Renewable Heating & Cooling Sector in Europe*. Brussels, Belgium. Available at https://www.globalccsinstitute.com/archive/hub/publications/155918/common-vision-renewable-heating-cooling-sector-europe-2020-2030-2050.pdf
21. Tagliabue, L. C., Maistrello, M., & Del, P. C. (2012). Solar Heating and Air-Conditioning by GSHP Coupled to PV System for a Cost Effective High Energy Performance Building*. Energy Procedia, 30*, 683–692.
22. Treberspurg, M., Djalili, M., & Staller, H. (2011). *New Technical Solutions for Energy Efficient Buildings*. State of the Art Report, Solar Heating & Cooling. Available at https://solarthermalworld.org/sites/default/files/SOTA_solar_heating___cooling.pdf
23. Vougiouklakis, Y., Theofilidi, M., & Korma, E. (2008). *Report on Market Situation & Trends about Small Scale Chillers.* WP2: Market Analysis. Pikermi Attiki, Greece: Centre for renewable energy sources.
24. World Renewable Energy Congress. (n.d.). Available at www.wrenuk.co.uk

sciendo

LATVIAN JOURNAL OF PHYSICS
AND TECHNICAL SCIENCES
2024, N 4

DOI: 10.2478/lpts-2024-0029

A TECHNICAL AND ECONOMIC STUDY OF SUSTAINABLE POWER GENERATION BACKUP

A. Backurs[1,2], L. Zemite[3*], L. Jansons[3,4]

[1]Latvian Hydrogen Association,
1 Akademijas Square, Riga, LV-1050, LATVIA
[2]Latvia University of Life Sciences and Technologies,
Faculty of Engineering,
5 J. Cakstes Blvd., Jelgava, LV-3001
[3]Riga Technical University,
Faculty of Computer Science, Information Technology and Energy,
Institute of Power Engineering,
12-1 Azenes Str., Riga, LV-1048, LATVIA
[4]Riga Technical University,
Faculty of Engineering Economics and Management,
6 Kalnciema Str. 210, Riga, LV-1048, LATVIA
*e-mail: laila.zemite@rtu.lv

This study focuses on overview and general economic viability evaluation of four types of portable electric generators: diesel and petrol internal combustion engines, batteries/accumulators and inverter systems (especially lithium polymer and lithium-ion battery systems), hydrogen fuel cell systems and combination (hybrid) of the latter. It does not include the rarely used, inefficient forms of energy conversion, such as steam turbines, as well as energy generators that are difficult to adjust with consumption and supply variations (variable forms of RES like wind and solar energy). The main targets of the study are battery/inverter systems, hydrogen fuel cell systems, and hybrid battery/inverter and hydrogen fuel cell systems, with hydrogen fuel cell systems being the thematic core.

Keywords: *Battery/inverter systems, economic evaluation, electric generators, hydrogen fuel cell systems, NPV.*

1. INTRODUCTION

Electric generators have become a remarkable technological achievement that provides energy at times when it is not available through conventional sources – electricity distribution grids. If there is no electricity, but it is necessary to operate tools, machinery or lighting equipment, a viable solution and permanent energy source – a generator, is available. Its popularity is due to sustainable performance, operational stability and frequently – compact size. Therefore, during the last century, electric generators have gained wide recognition not only in construction, but also other sectors of the national economy, such as the military and healthcare [1].

Two general types of generators are mostly used worldwide – stationery and portable ones [2]. These generators are popular due to the availability of fuel and infrastructure. Stationary electric generators are larger, significantly heavy, usually very powerful and are used when large amounts of electricity are needed for extended periods of time. They are chosen for various projects, especially in energy intensive phases of construction [3]. Portable electric generators, on the other hand, are lighter and quieter: the characteristics that allow them to be used even in residential areas, for example, in case of a short-term power outages [4].

In Latvia, the following information was obtained from rentals, construction and electrical engineering companies regarding possession and availability of high-power electric generators (100 kilowatts (kW) or above). About 3000 100 kW generators are owned by construction and electrical engineering companies alone for provision of backup power, and about 2000 generators are readily available through rentals. Most of these generators are used in construction and industrial facilities. The information regarding low and medium power electric generators is problematic to obtain, because they are widely used throughout the country and mostly utilized by small businesses and private owners.

However, portable electric generators tend to be domineering entity in the Latvian generator market due to their availability, modest price and large numbers. They are very useful but have both advantages and disadvantages. Among advantages, the following points should be brought forward:

- mobility: portable generators can be easily moved and used in different locations;
- compactness: these generators are relatively small, so their installation takes up little space;
- uninterrupted power supply: capable of providing continuous power supply – does not react to external conditions;
- autonomous energy supply: the ability to work autonomously, in case of accidents and network outages, even completely off-grid.

Their disadvantages, on the other hand, include:

- limited power: portable generators are usually of low power, so they can only run the most essential electrical appliances;
- high cost: some portable generators, such as inverter generators, can be expensive. The cost of the obtained electricity is higher than for stationary high-power generators;
- safety issues: mobile generators can cause injuries, burns, and even carbon monoxide poisoning if used improperly, especially in enclosed spaces [5] – [6].

They can provide a stable and steady supply of electricity, which makes them ideal and especially useful in extreme conditions such as storms or other unforeseen circumstances when the standard power supply is interrupted. However, at the same time, most of these generators still produce carbon dioxide (CO_2) emissions and, to a certain degree, are harmful to the environment. Moreover, electric generators, including portable ones, produce a considerable share of CO_2 emissions in areas like ports, airports, customs, etc. [7]–[10]. In this regard, therefore, it is very important to analyse available avenues of decarbonisation of the stationary and portable generator sectors and provide a long-term solution for the pollution problem they cause.

2. THE STUDY DESCRIPTION

A study was carried out regarding the implementation of maximally CO_2 emission free portable electric generators, which can be divided by power, the type of energy conversion, and by the type of primary energy use. Division by power includes low power generators (up to 5 kW; they are suitable for households, small businesses or emergency situations), medium power generators (from 5 to 50 kW; they can provide more power, and often used in places of business and country houses or small hotels) and high power generators (over 50 kW; they are suitable for large businesses, factories or other large facilities like schools and hospitals).

At the same time, division by type of energy conversion includes mechanical drive-based generators (wind generators etc., conversion of renewable energy resources (RES)), afterburners like steam turbines, Stirling engines, etc., internal combustion engine drives (various fuels – liquid, gaseous, both fossil and RES), solar photovoltaic converters – solar panel/inverter systems, electrochemical batteries/accumulators and inverter systems, and electrochemical process – fuel cells (fuel–hydrogen, methane, etc.).

The study focuses on comparison of internal combustion engine drives, batteries/accumulators and inverter systems (especially lithium polymer and lithium-ion battery systems), hydrogen fuel cell systems and combination of latter two. It does not include the rarely used, inefficient forms of energy conversion, such as steam turbines, as well as energy generators that are difficult to adjust with consumption and supply (variable forms of RES like wind and solar energy). The main targets of the study are battery/inverter systems, hydrogen fuel cell systems, and hybrid battery/inverter and hydrogen fuel cell systems, with hydrogen fuel cell systems being the thematic core [11] – [12].

2.1. Battery/Inverter Systems

Battery/inverter systems have become a popular choice for electric generators. They are quiet, environmentally friendly at the point of use and can generate electricity from stored RES, such as solar or wind energy.

Advantages of these systems include but are not limited to:

- quiet operation, does not cause acoustic pollution;
- environmentally friendly applications with no emissions;
- can be used safely in closed areas;
- can operate solely on RES;

- short start-up and shutdown times – consumption can be precisely controlled, reducing energy losses.
- However, at the same time, systems have some disadvantages:
- at a comparable power, much larger dimensions and mass (up to 3 times greater mass) than internal combustion engine powered electric generators;
- regular charging is required in a suitably prepared place – it is impossible to bring energy to any location;
- battery costs currently are over 400 EUR/kWh – significant costs in cases of higher energy consumption [13].

2.2. Hydrogen Fuel Cell Systems

Hydrogen fuel cell systems are the latest technology in the electric generator industry. They are quiet, environmentally friendly and can generate electricity using hydrogen of any origin.

The advantages of such systems are the following:

- they use hydrogen, which is RES and can be obtained at any place where there is access to water and energy [14] – [16];
- emissions in a form of water vapour do not cause pollution;
- quiet, i.e., do not cause acoustic pollution;
- safety operation in closed areas;
- short start-up and shut-down time – consumption can be accurately controlled, reducing energy losses;
- fast re-filling.

Disadvantages of hydrogen fuel cell systems include:

- it is not always possible to be charged AEG with green hydrogen, as well as to obtain green electricity through electrolysis;
- hydrogen produced from natural gas can be regarded only partially environmentally friendly;
- at a comparable power, much larger dimensions and mass (up to 2 times the mass) than internal combustion engine powered electric generators.

2.3. Hybrid Battery/Inverter and Hydrogen Fuel Cell Systems

Fuel cell systems and batteries can work together to provide more options for transportation and energy. Fuel cell systems are designed to improve the interaction between batteries and electric propulsions. While each system has its own advantages, combining battery and fuel cell technologies can help reduce overall CO_2 emissions and increase the use of RES without compromising the system's performance.

Obvious advantages of connecting the fuel cell to the batteries systems are as follows:

- high energy efficiency: fuel cells offer high energy conversion efficiency compared to conventional internal combustion engines, thereby reducing energy waste and increasing overall system efficiency;
- environmental benefits: fuel cells produce electricity through electrochemical reactions, resulting in reduced greenhouse gas emissions and air pollution compared to fossil fuel-based energy sources;
- range extension: integrating fuel cells with storage batteries can extend the range of mobile electrical systems, as fuel cells provide continuous power by generating electricity from a fuel source

(such as hydrogen) without the need for frequent recharging;
- fast refuelling: refuelling a fuel cell system can be faster than charging a battery because it involves refuelling rather than waiting for the battery to charge. This can be beneficial for time-sensitive applications such as electric vehicles.

Several disadvantages of such hybrid systems are as follows:
- cost: fuel cell systems are currently more expensive compared to traditional battery-based systems, mainly due to the high cost of fuel cell stacks and hydrogen infrastructure;
- hydrogen infrastructure: building a widespread hydrogen infrastructure for refuelling can be a major challenge, as it requires significant investment in hydrogen production, storage, transportation and distribution;
- fuel availability and storage: availability and storage of hydrogen can be problematic, as hydrogen requires special infrastructure and processing procedures due to its low energy density and high flammability;
- durability and lifespan: fuel cell systems may have limitations in terms of durability and lifespan, especially in mobile applications with varying operating conditions and frequent start-ups and shutdowns. Long-term reliability can be a concern.

3. A FUEL CELL BASED HYDROGEN GENERATOR SYSTEM

The hydrogen fuel cell electric generators have a great market potential locally, as there are currently approximately 5000 generators with a capacity of 100 kW in Latvia. It can be concluded that the advantages of hydrogen fuel cell powered generators compared to diesel generators are that they do not produce both CO_2 emissions and noise pollution. Using hydrogen fuel cells, the 100-kW generator can run for 24 hours on a single charge and saves up to 46 tons of CO_2 /year. CO_2 savings depend on how often it is used.

During the study, special attention was paid to technical characteristics of the mobile hydrogen generator mounted on a trailer. Uniform parameters of electricity supply (output) were defined as follows: 100 kW output power (electricity), amount of stored energy 800 kWh for electricity generation. Also, the following components were selected for creation of such mobile generator: trailer, 100 kW fuel cell, 48 kg hydrogen storage system, 5 kWh battery module, power control module.

A conceptual design of the hydrogen fuel cell electric generator is shown in Fig. 1.

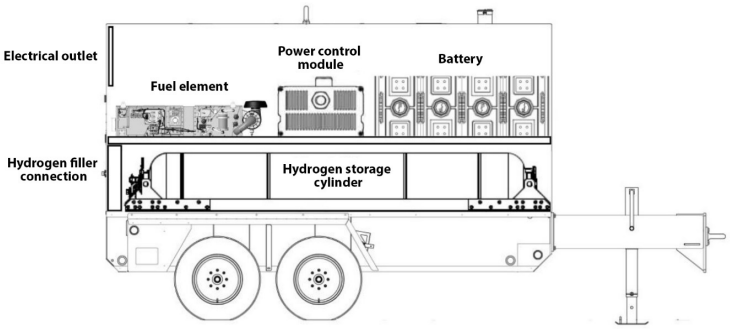

Fig. 1. A conceptual design of the hydrogen fuel cell electric generator.

A technical design of hydrogen fuel cell electric generator with the end panels can be seen in Fig. 2 and conceptual scheme of the hydrogen generator in Fig. 3.

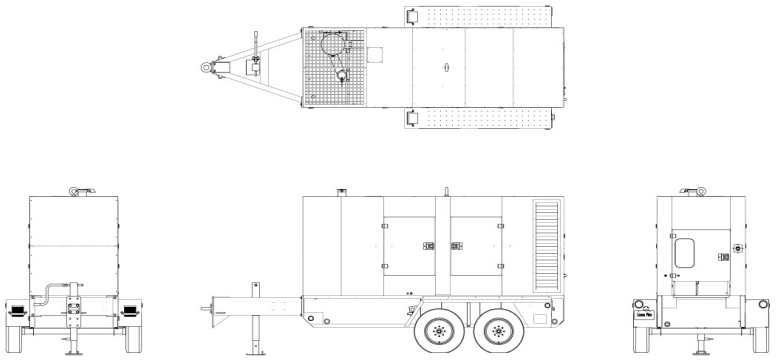

Fig. 2. An overview of the hydrogen generator with the end panels.

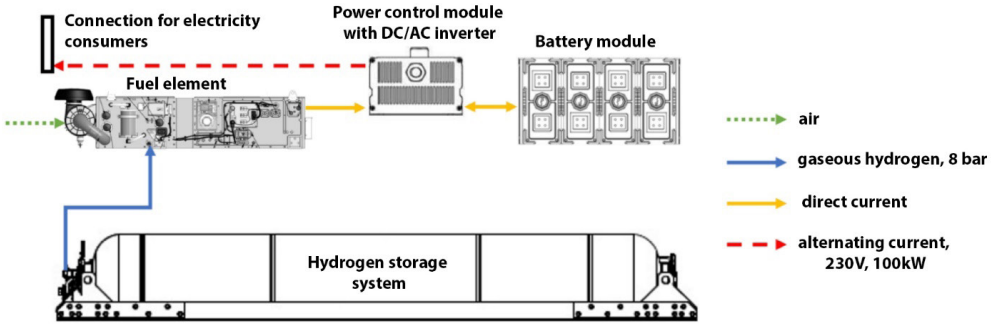

Fig. 3. A conceptual scheme of the hydrogen generator.

3.1. The Operational Principle of the System

The hydrogen storage system, with a capacity of 48 kg, provides the necessary amount of hydrogen for the generation of 800 kWh of electricity. The working pressure of the cylinder system is 350 bar. A direct current is generated by oxidizing hydrogen in a thermochemical process in a fuel cell. The direct current from the fuel cell is fed through the device control module after conversion in a DC/AC inverter as an alternating current to the consumer's connection contact. The control system module initiates the switching on of the fuel cell when the consumer is connected.

The following technical components are needed for the generator: trailer suitable for transportation on public roads, fuel cell, power 100 kW, hydrogen storage system, capacity of 48 kg and working pressure of 350 bar, elements of the gaseous hydrogen supply system, battery module, capacity of 5 kWh, power control module with integrated battery charge control module and DC/AC or direct current/alternating current inverter, consumer connections, metal constructions, their fastenings and connections,

electrical installation elements, including high-voltage and low-voltage wiring. All these components, except for the fuel cell and hydrogen storage system, can be considered standard components available in the market and can be separately acquired.

3.2. Selection of Hydrogen Storage System

For the selection of the hydrogen storage system, several potential suppliers of composite cylinder systems were inquired. Although the technical specification and drawings were sent only by the company "Worthington Cylinders GmbH", after conducting in-depth research on shared websites, it was concluded that equivalent composite cylinder hydrogen systems were offered by several manufacturers and such systems were considered a standard product in the automotive industry. Using information collected from suppliers, a standard hydrogen filling, storage and delivery system was designed as depicted in Fig. 4.

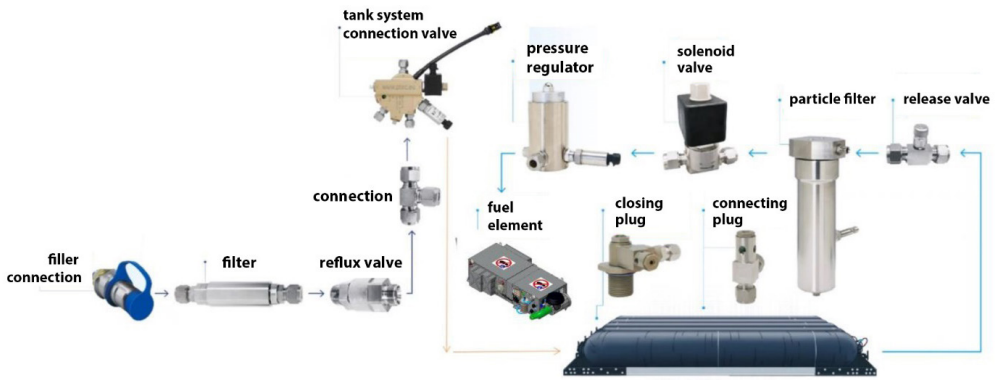

Fig. 4. A standard hydrogen filling, storage and delivery system.

Several potential suppliers who could offer a 100-kW power fuel element were approached for the selection of fuel cells. The technical specification was received from "Ballard Power Systems Europe" and "PowerCell Sweden AB". A comparison of the most important technical parameters of both systems is listed in Table 1.

Table 1. Comparison of the Most Important Technical Parameters of Ballard Power Systems Europe and PowerCell Sweden AB

Parameters	**Ballard Power Systems**	**PowerCell**
System power	100 kW	100 kW
Operating voltage	280–560 V	250–500 V
Work capacity	21–360 A	50–450 A
Weight	256 kg	212 kg
Hydrogen supply pressure	8 bar	8–12 bar
Working temperature	-30 - +50 °C	-30 - +45 °C
Efficiency ratio, max	57 %	55 %
Power control system	CANbus	CANbus
Operational duration	25 000 h	20 000 h
Defence class	IP54	IP54

Looking through the parameters, it was concluded that although no significant differences were present, it would be more appropriate to use "Ballard Power Systems Europe" fuel cell due to higher efficiency and duration of operation.

4. THE ECONOMIC EVALUATION

The use of electric generators of all kinds, including portable ones, is determined not only by technological but also economic parameters, which are closely related to technical ones. It is especially important to evaluate their cost, because users are professionals who need long-term economic benefits from the potential investment. Therefore, an economic evaluation was performed comparing internal combustion generators using petrol and diesel (systems of two different combustion processes) with battery/inverter system and hydrogen fuel cell/inverter systems.

The following unified electricity supply (output) parameters were defined for all system:

- 100 kW output power (electricity);
- 8-hour working day with an average workload of 80 %;
- regular use – 245 d/year;
- filling/transportation to and from the filling/refuelling location takes place outside working hours (it is included in expenses);
- for battery system – battery replacement after 1000 charging cycles (battery price 150 EUR/kWh).

The total amount of energy to be delivered, considering the above conditions, was calculated as follows:

$$E = 100\ kW * 8\ h * 245d * 0.8 = 156\,800\ kWh = 156.8\ MWh$$

The determined work modes show that each of the considered generator types must have 800 kWh of energy reserves available (8-hour working day with a load of 100 kW – max energy amount of 800 kWh). The average load is used to model the energy consumption of longer periods (monthly, yearly), but the daily consumption can also be used as the maximum in some cases, too.

4.1. Maintenance Cost Estimate

Maintenance cost estimates were done for all technologies under review. For internal combustion engine generators, they included refuelling, oil changes, filter changes and other regular activities, with average maintenance costs of about 100–200 EUR/MWh/year.

For battery/inverter system maintenance costs included battery replacement and inverter maintenance, with average maintenance costs of about 50–100 EUR/MWh/year.

In the case of hydrogen PEM fuel cell inverter system maintenance costs included electrolyte replacement and other activities. They brought expected average maintenance costs to about 50–75 EUR/MWh/year [17].

4.2. CAPEX and OPEX

OPEX represents operating expenses, and CAPEX represents capital expenditures. OPEX covers day-to-day operations, while CAPEX involves acquiring assets for long-term use. The main difference between OPEX and CAPEX is the duration of the benefits they generate. Operating expenses provide short-term benefits, whereas capital expenditures provide long-term benefits. Another significant difference is how expenses are recorded in financial statements. Operating expenses are recorded as expenses in the period they are incurred. Capital expenditures are recorded as assets on the balance sheet and are depreciated over their useful life [18]. In this comparison, OPEX and CAPEX differences stand out rather significantly.

CAPEX was calculated for acquisition of electric generators with electric power of 100 kW, and the outcome of this calculation is shown in Table 2.

Table 2. Acquisition of Electric Generators and Generator Systems (100 kW)

Technology	Acquisition costs (EUR)
Internal combustion engine (petrol)	20 000
Internal combustion engine (diesel)	25 000
Batteries/inverter	340 000 (400 EUR/kWh for battery and 20 000 EUR for inverter)
Hydrogen PEM fuel cells	200 000 (100 000 EUR for fuel cell, 20 000 EUR for investors, 10 000 EUR for power control unit and 70 000 EUR hydrogen balloons)

On the other hand, OPEX for different technologies mainly includes such options as fuel and its calorific value. For a comparison, it was necessary to recalculate the calorific value of petrol and diesel fuel from kWh/kg to kWh/l. For diesel, this conversion factor is 0.84, and for petrol it is 0.72. Fuel costs for 1 MWh electricity generation, considering the efficiency of various technologies and fuel prices, are summarised in Table 3. At the end of 2023, the retail prices of petrol and diesel fuel in Latvia were very similar – it was assumed to be 1.7 EUR/l.

Table 3. Fuel Costs for 1 MWh of Electricity Generation

	Heat capacity, kWh/kg	Fuel price, EUR/kg	Amount of fuel 1MWh/kg	Fuel cost, EUR/MWh, at 100 % efficiency
Gasoline	12.5	2.43	80	194.29
Diesel fuel	12.8	2.02	78.13	158.11
Electricity from the grid				150.00
Hydrogen	36	10.00	27.78	277.78

As shown in Table 4, evaluating the efficiency of each specific conversion technology (primary energy into electricity) significantly increases the cost of each technology for production of 1 MWh_e.

Table 4. Evaluation of Technology Efficiency (%) for Generation of 1 MWhe

	Conversion efficiency, %	Fuel costs, EUR/MWh, 100 % efficiency	Fuel costs, EUR/MWh, at the lowest efficiency of the given technology	Fuel costs, EUR/MWh, at the highest efficiency of the given technology
Internal combustion engine (petrol)	20–30	194.29	971.45	647.63
Internal combustion engine (diesel)	30–40	158.11	527.0333	395.285
Batteries/inverter	85–90	150.00	187.5	166.67
Hydrogen PEM fuel cells	40–70	277.78	694.45	396.83

Maintenance costs for 156.8 MWh energy production depend on the complexity of the technology, and the comparison of maintenance costs (EUR/MWh, EUR/year) is given in Table 5.

Table 5. The Comparison of Maintenance Costs (EUR/MWh, EUR/year)

Technology	Maintenance costs (EUR/MWh)	Maintenance costs (EUR/year)
Internal combustion engine (petrol)	100	15 680
Internal combustion engine (diesel)	200	31 360
Batteries/inverter	75	11 760
Hydrogen PEM fuel cells	75	11 760

Total operating costs, including maintenance costs, to produce 156.8 MWh of energy are summarised in Table 6.

Table 6. Total Operating Costs, Including Maintenance (EUR, EUR/year)

Technology	Fuel costs (EUR)	Maintenance costs (EUR/year)	Costs (EUR/year)
Internal combustion engine (petrol)	101 549	15 680	117 229
Internal combustion engine (diesel)	61 979	31 360	93 339
Batteries/inverter	26 133	11 760	37 893
Hydrogen PEM fuel cells	62 223	11 760	73 983

4.3. NPV Evaluation

To be able to compare economic viability of all generator technologies in a long run, the net present value (NPV) method was utilised with valuation period of 10 years – working life of professional equipment, as the chronological base. The following discount rates were used in the model – 5 %, 10 %, and 15 %.

Additional assumptions in the NPV model were chosen:

- after every 4 years (1000 charge and discharge cycles) the battery is changed;
- the battery system is transported daily 50 km to the charging point (transportation costs per day – fuel 10 EUR/day, wages and other costs – 40 EUR /day);

- the price of fossil fuels increases by 10 %/year;
- the price of hydrogen decreases by 10 % /year;
- the price of electricity decreases by 5 %/year;
- maintenance costs increase by 10 %/year.

Applying the NPV model, it was found that at low discount rates (5 % and less) the hydrogen fuel cell system was the most profitable. As the discount rate increases, the best solution is the battery/inverter system (see Figs. 5–7).

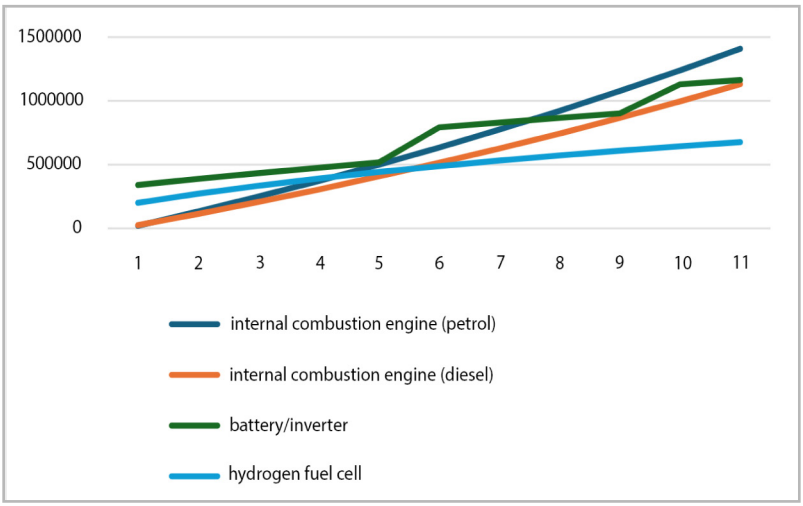

Fig. 5. NPV model with a 5 % discount rate.

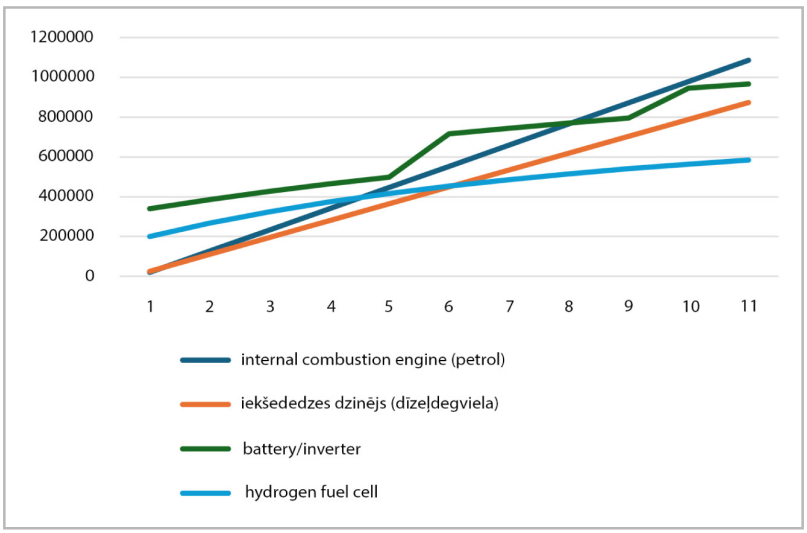

Fig. 6. NPV model with a 10 % discount rate.

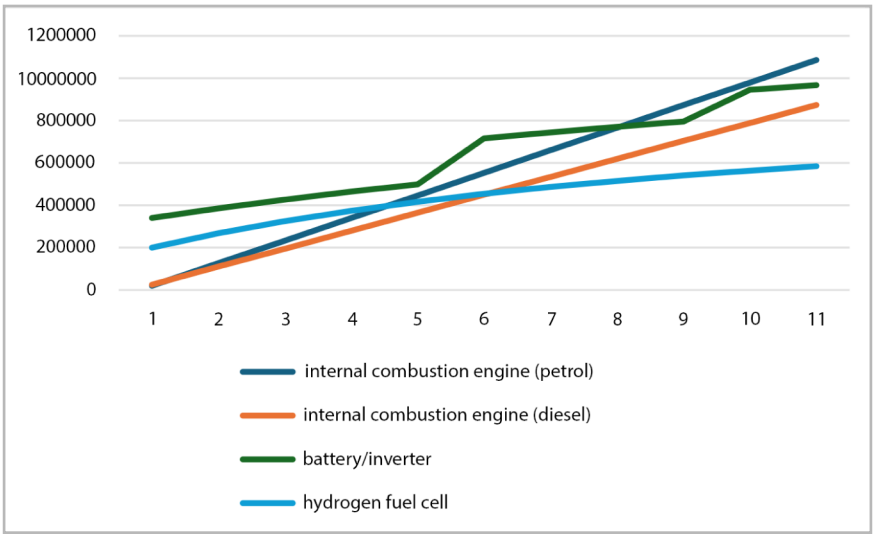

Fig. 7. NPV model with a 15 % discount rate.

5. CONCLUSIONS

- If only CAPEX is considered, internal combustion engine-powered autonomous generators are the cheapest. However, if also OPEX costs are taken into consideration, battery/inverter systems and hydrogen fuel cell systems may be cheaper in the long run.
- Battery/inverter systems are more expensive up front but can be cheaper in the long run than internal combustion engine-powered autonomous generators due to lower fuel costs.
- Hydrogen fuel cell systems are expensive at the initial stage but can be cheaper than internal combustion engine-powered generators in the long run because fuel costs are even lower than batteries/inverters. However, it is important to note that the cost of electricity is only one factor to consider when choosing a generator. Other important factors include system reliability, efficiency and overall cost effectiveness.
- The study confirms that the production of portable hydrogen generators is promising. They have the potential to find wide application both in the national economy and in the military sector, since the operation of the generator of such technology, compared to generators powered by internal combustion engines, ensures a significant reduction in noise levels and a reduction in CO_2 emissions.

ACKNOWLEDGEMENT

The research has been funded by project No.5.1.1.2.0/1/22/A/CFLA/001 “Design and Development of a Hydrogen Back-up Power Supply System”.

REFERENCES

1. Vasylyev, A., Vannoni, A. & Sorce, A. (2023). Best Practices for Electricity Generators and Energy Storage Optimal Dispatch Problems. *Journal of Engineering for Gas Turbines and Power, 146*, 1–13. 10.1115/1.4063529.
2. Dingbo Power. (2023). *The Difference Between Stationary Generators and Portable Generators*. Available at https://www.dieselgeneratortech.com/generator-sets/the-difference-between-stationary-generators-and-portable-generators.html
3. Woodstock Power Company. (n.d.*). Woodstock Power Company Web Series: Stationary Generators (What Type?).* Available at https://woodstockpower.com/blog/woodstock-power-company-web-series-stationary-generators-what-type/
4. PG&E. (2019). *What You Need to Know About Backup Generation.* Available at https://sonomacleanpower.org/uploads/documents/PGE-Backup-Generation-Fact-Sheet.pdf
5. Active Generator Rental. (n.d.). *Pros & Cons of Portable Generators (Why it's Best to Get Them)*. Available at https://activegenrental.com/blog/pros-and-cons-of-portable-generators/
6. Tom's Guide. (2022). *Should you Get a Home Generator? Here's the Pros and Cons.* Available at https://www.tomsguide.com/news/should-you-get-a-home-generator-heres-the-pros-and-cons
7. Wang, B., Liu, Q., Wang, L., Chen, Y., & Wang, J. (2023). A Review of the Port Carbon Emission Sources and Related Emission Reduction Technical Measures. *Environmental Pollution, 320,* 121000, https://doi.org/10.1016/j.envpol.2023.121000.
8. EiT. (n.d.). *A Practical Guide to Decarbonising Ports. Catalogue of Innovative Solutions*. Available at https://eit.europa.eu/sites/default/files/decarbonising_ports-catalogue_of_innovative_solutions_f.pdf
9. Colarossi, D., Lelow, G., & Principi, P. (2022). Local Energy Production Scenarios for Emissions Reduction of Pollutants in Small-Medium Ports. Transportation *Research Interdisciplinary Perspectives, 13*, 100554, https://doi.org/10.1016/j.trip.2022.100554.
10. Critter Guard. (2021). *4 Major Benefits of a Portable Generator.* Available at https://www.critterguard.org/blogs/articles/4-major-benefits-of-a-portable-generator
11. Zemite, L. Backurs, A., Starikovs, A., Laizans, A., Jansons, L., Vempere, L., … & Broks, A. (2023). A Comprehensive Overview of the Europen and Baltic Landscape for Hydrogen Applications and Innovations. *Latvian Journal of Physics and Technical Sciences, 60* (3), 33–53. doi: 10.2478/lpts-2023-0016
12. Jansons, L., Zemite, L., Zeltins, N., Geipele, I., & Backurs, A. (2023). Green and Sustainable Hydrogen in Emerging European Smart Energy Framework. Latvian Journal of Physics and Technical Sciences, 60 (1), 24–38. doi: 10.2478/lpts-2023-0003
13. Anker. (2023). *What is an Inverter Generator: Working Rule, Pros and Cons*. Available at https://www.anker.com/blogs/home-power-backup/what-is-an-inverter-generator-working-rule-pros-and-cons
14. Kleperis, J., Boss, D., Mezulis, A., Leniscenoks, P., Knoks, A., & Dimanta, I. (2021). Analysis of the Role of the Latvian Natural Gas Network for the Use of Future Energy Systems: Hydrogen from RES. Latvian Journal of Physics and Technical Sciences, 58 (3), 214–226. doi: 10.2478/lpts-2021-0027
15. Jansons, L., Zemite, L., Zeltins, N., Bode, I., Geipele, I., & Kiesners, K. (2022). The Green Hydrogen and the EU Gaseous Fuel Diversification Risks. Latvian Journal of Physics and Technical Sciences, 59 (4), 53–70. doi: 10.2478/lpts-2022-0033

16. Kobzars, V., Zemite, L., Jasevics, A., Kleperis, J., Dimanta, I., Knoks, A., & Leniscenoks, P. (2021). Appropriateness of hydrogen production in low-power hydropower plant. In *Proceeding of IEEE 62nd International Scientific Conference on Power and Electrical Engineering of Riga Technical University*, RTUCON 2021. doi: 10.1109/RTUCON53541.2021.9711687
17. Powermag. (n.d.) *How Much will Hydrogen-Based Power Cost?* Available at https://www.powermag.com/how-much-will-hydrogen-based-power-cost/
18. WEC.(2013).*WorldEnergyPerspective.Cost of Energy Technologies.* Available at https://www.worldenergy.org/assets/downloads/WEC_J1143_CostofTECHNOLOGIES_021013_WEB_Final.pdfelectricity con

sciendo

LATVIAN JOURNAL OF PHYSICS
AND TECHNICAL SCIENCES
2024, N 4

DOI: 10.2478/lpts-2024-0030

EXPERIMENTAL MEASUREMENT OF WORKING PARAMETERS OF CONICAL ELECTROMAGNETIC LEVITATION COILS

V. Silamikelis[1], J. Snikeris[1,2*], A. Apsitis[1], A. Pumpurs[1]

[1]Institute of Atomic Physics and Spectroscopy,
University of Latvia,
19 Raina Boulevard, Riga, LV-1586, LATVIA
[2]G. Liberts' Innovative Centre of Innovative Microscopy,
Daugavpils University,
1 Parades Str., Daugavpils, LV-5401, LATVIA
*e-mail: janis.snikeris@lu.lv

Electromagnetic levitation (EML) is a promising technique allowing to melt various materials, including refractive metals, while avoiding physical contact between the molten material and components of the melting system, thus avoiding contamination of the molten material. EML coils act both as a container and a heating source for a conductive sample placed within it. EML systems are difficult to optimize for specific tasks and computational simulations are often used to aid the process. Development of simulations of EML processes is an ongoing field of research. Obtaining precise experimental measurement data of EML processes is important for development and verification of computational simulations. This study aims to provide experimental data of simultaneous measurements for magnetic field, Joule heating and lift force in different conical EML coils with a counterturn.

Keywords: *Electromagnetic heating, electromagnetic levitation.*

1. INTRODUCTION

Application of Electromagnetic Levitation (EML) for melting of various materials, especially refractive metals, is a complicated technological challenge. Compared to other methods or alloy creation (arc melting and cold crucible furnace), EML melting provides natural separation between the molten material and the components of the melting system, which could act as a source of contamination for the molten

material. In addition to alloy creation, there have recently been successful attempts to directly grow crystals from the melt contained in EML conditions [1]. Unfortunately, EML methods are extremely difficult to apply in practice, since EML processes are extremely sensitive to the properties of the molten material, as well as the parameters and design of the melting device.

In the process of EML, high-frequency voltage is applied to an EML coil, consisting of one or more windings. Applied voltage induces high-frequency current in the windings, and the circular current produces high-frequency magnetic field within (and around) the EML coil. If a conductive sample is inserted into the EML coil, the magnetic field will induce eddy currents along the surface of the sample. These eddy currents generate heat in the sample and create the magnetic field in the opposite direction of the externally applied field, resulting in repulsive force in relation to the EML coil. If the sample is located above the EML coil, this repulsion (or lift) force counteracts the gravity force acting on the sample and enables stable levitation of the sample.

Computational methods are commonly used to adapt and optimize EML systems for their specific tasks [2]–[4]. In case of small sample sizes, the magnetic field in the EML coil can be used to estimate the heating [5] of the sample and the lift force [6] acting on the sample. 2D models are often used to estimate the EM field within EML coils [7]. However, recently it has been shown that true 3D models produce different results [8]. As the development of simulation models for EML systems is an ongoing field of research, high accuracy experimental measurement data of EML systems are important for reference and verification of those models.

EML coils with conical shape are commonly used for EML melting of metals [9]. A "counter-turn" (a winding or multiple windings placed in opposite direction), which is placed above the windings of the EML coil, can improve the stability of the sample placed in EML coil [10]. Recently, there has been an article describing simulated modelling data for conical EML coils with a counter-turn, including lift force for conical EML coils with varying conical angle [3]. Previously we have published papers describing a method for simultaneous measurement of the lift force, Joule heating and magnetic field acting on a conductive sample placed in different positions along the vertical axis, within an EML coil [11], [12]. In this paper, we aim to apply that measurement method to conical EML coils with varying angles and to compare the obtained data to the simulation results presented in the literature.

2. MATERIALS AND METHODS

Two EML coils were studied in this work (see Fig. 1). Both coils were made from copper tube (6 mm diameter). Tubes were hollow to enable water cooling during the operation of the EML coils. The EML coil with the narrower conical angle $\alpha=2.5\pi/32$ (see Fig. 1, inclusion) was denoted with "EML coil #1", and the coil with wider conical angle $\alpha=5\pi/32$ was denoted with "EML coil #2". The diameter d and position along vertical (z) axis for each winding of both EML coils is shown in Table 1. The z-positions of the windings were measured from the "front" side of the coil (opposite to the connectors) and the diameter of the windings was measured from the "sides" of

the coil (perpendicular to the front – connector side direction and the vertical axis). The z-axis was set to 0 at the centre of the bottom winding position.

The schematic of the experimental setup is presented in Fig. 2a. A high-frequency induction furnace (MXBAOHENG LH-25A) serves as a power source for an EML coil and worked under resonance conditions (current frequency depends on the shape of EML coil). A measurement probe (see Fig. 2b) moves through the EML coil, with 2 mm step size, in vertical direction via mechanical precision lifting platform with in-built scale for position measurement. The sample placed in the measurement probe was an Al sphere with 5 mm diameter, weighing 176.7 mg. To ensure frictionless measurement of the weight change of the sample (and measurement probe), a circular frame holding the measurement probe in vertical position atop a precision balance by binding threads was used as a stabilization device. The vertical component of the magnetic field around the sample was measured by a probe coil (diameter d_z = 6.5±0.25 mm, number of windings N_z = 3), which was positioned around the centre of the Al sample, in the horizontal plane. Probe coil was made from a copper wire with Teflon insulation. The body of the measurement probe was made from Teflon. Weight measurements were done with "Kern 440-33" precision balance. "Siglent SDS1104X-E" oscilloscope was used to measure the signal (frequency and RMS voltage) from the probe coil and the coil wound around one of the EML coil connectors, which served as a synchronization signal. The temperature of the sample was measured through a thermocouple attached to the bottom surface of the Al sample.

The measurements were performed in the following steps. After moving the measurement probe into position, the power source was turned on for 3 seconds. EML coil was powered only in short intervals to avoid melting of the sample and damaging the measurement probe. In the time when the EML coil was powered, the oscilloscope readings and measurement of the weight change of the probe were recorded at 2 seconds. As for the temperature measurement, the highest temperature reading reached during or shortly after powering the EML coil was recorded. After turning off the power source and recording the measurements, it was waited until the sample temperature reading fell back to ambient/room temperature. If the temperature of the sample at the end of the measurement was higher than 50 °C, liquid nitrogen was poured into the "cooling bath" on top of the measurement probe to accelerate the cooling process. The step distance for subsequent measurements was 2 mm, but every 5 steps (or every 10 mm) the measurements were repeated 5 times for the purpose of calculating uncertainty of the measurement. Uncertainties of the measurements were calculated at 95 % confidence interval. Also, measurements for both EML coils were repeated with and without the Al sample. In the measurement without the sample, only the magnetic field was measured. The lift force F was calculated as follows:

$$F = -\Delta P\, g, \tag{1}$$

where ΔP is the change of weight and g = 9.81 m/s^2. The amplitude of the magnetic flux along the vertical axis B_z was calculated as follows:

$$B_z = \frac{\sqrt{2}U_z}{2\pi N_z A_z f}, \tag{2}$$

where U_z is the RMS voltage on the probe coil, f is the current frequency on the probe

coil (and synchronization signal coil), N_z is the number of windings in the probe coil, and A_z is the area of the probe coil ($A = \pi d^2/4$).

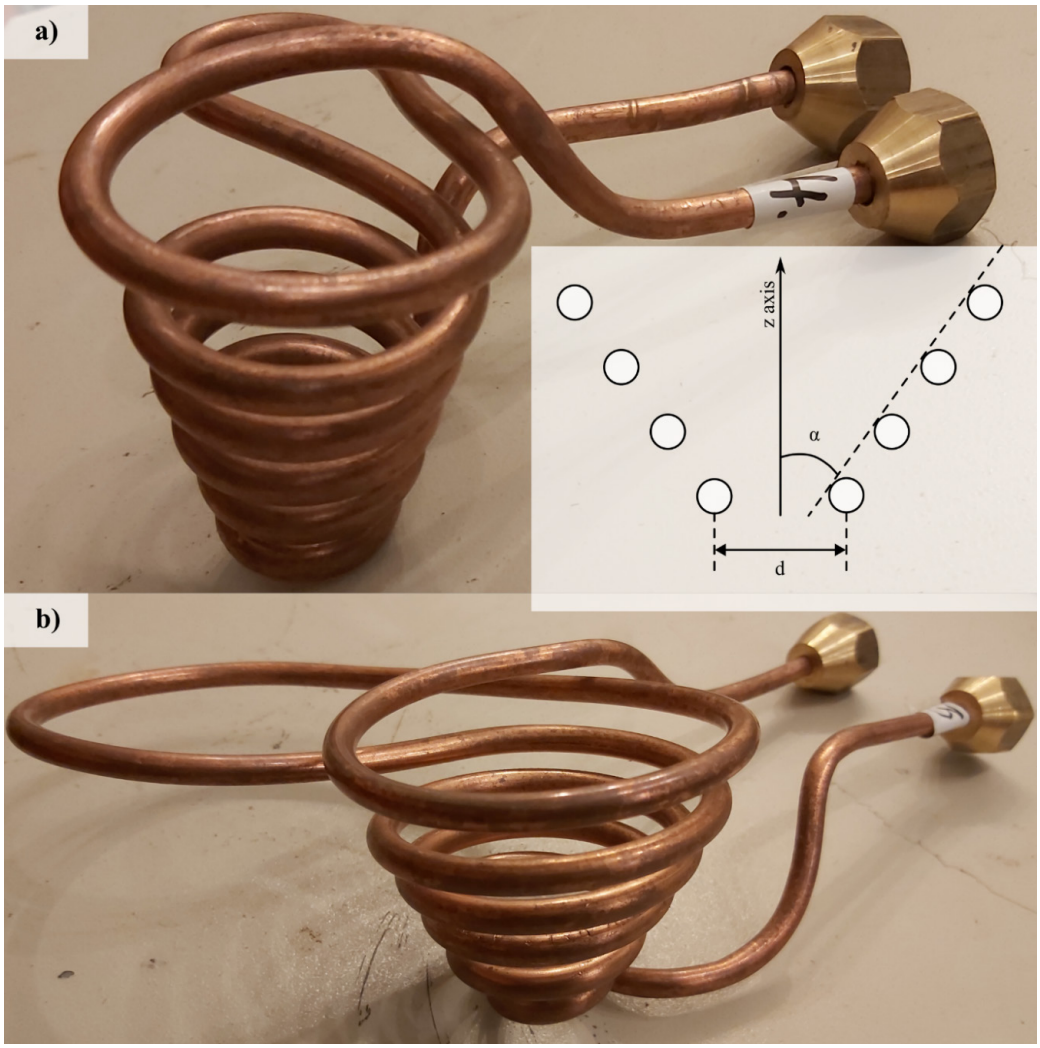

Fig. 1. Images of the EML coils. a) EML coil #1 (α=2.5π/32); b) EML coil #2 (α =5π/32); Inclusion – EML coil schematic with definition of coil winding diameter (d) and conical angle (α).

Table 1. Diameter and Position along z (vertical) Axis of the Windings of Both EML Coils

	EML coil #1 (α =2.5π/32)		EML coil #2 (α=5π/32)	
Winding No.	z-position [mm]	diameter d [mm]	z-position [mm]	diameter d [mm]
1	0 ± 0.5	22 ± 0.5	0 ± 0.5	22 ± 0.5
2	10 ± 0.5	27 ± 0.5	10 ± 0.5	33.7 ± 0.5
3	20 ± 0.5	32 ± 0.5	20 ± 0.5	43.4 ± 0.5
4	30 ± 0.5	37 ± 0.5	28 ± 0.5	54 ± 0.5
5	40 ± 0.5	42 ± 0.5	40 ± 0.5	64.7 ± 0.5
6 (counter-turn)	60 ± 0.5	52 ± 0.5	60 ± 0.5	86.4 ± 0.5

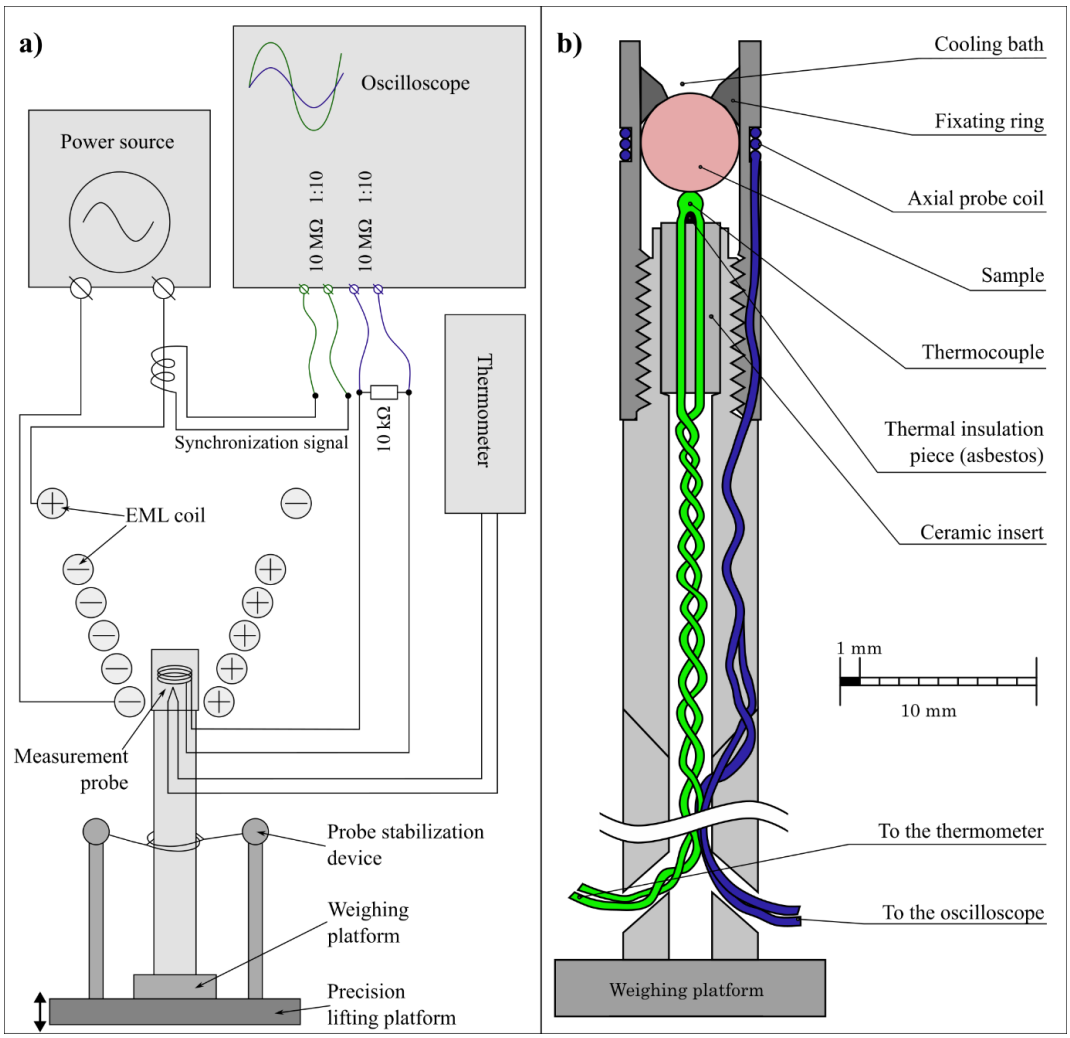

Fig. 2. a) Schematic of the experiment; b) Schematic of the measurement probe.

3. RESULTS AND DISCUSSION

The measurement results for EML coil #1 and EML coil #2 are presented in Fig. 3 and Fig. 4, respectively. In both cases, after inserting the Al sample in the probe, the magnetic field amplitude (at its peak value) is reduced by about 19 %. No significant change in resonance frequency of the EML coil was observed during the measurements. For both EML coils, the most intensive heating of the sample happens around the lower end of the second winding. This area corresponds to the highest intensity of the magnetic field and the point where the lift force changes direction. Regarding the lift force, stable levitation is possible in areas, where the lift force is positive with a negative derivative (lift force should increase, as the sample is moving down).

For EML coil #2, this area, where stable levitation is possible, is much wider (z val-

ues from 16 to 54 mm) compared to EML coil #1 (z values from 34 to 54 mm). The point of equilibrium for the Al sample was at 42 and 37 mm, for EML coils #1 and #2, respectively. It should be noted that for EML coil #2, the point of equilibrium for the Al sample is in an area with higher heating intensity compared to EML coil #1. This shows that EML coil #2 can be expected to be more efficient for the task of heating and melting the sample.

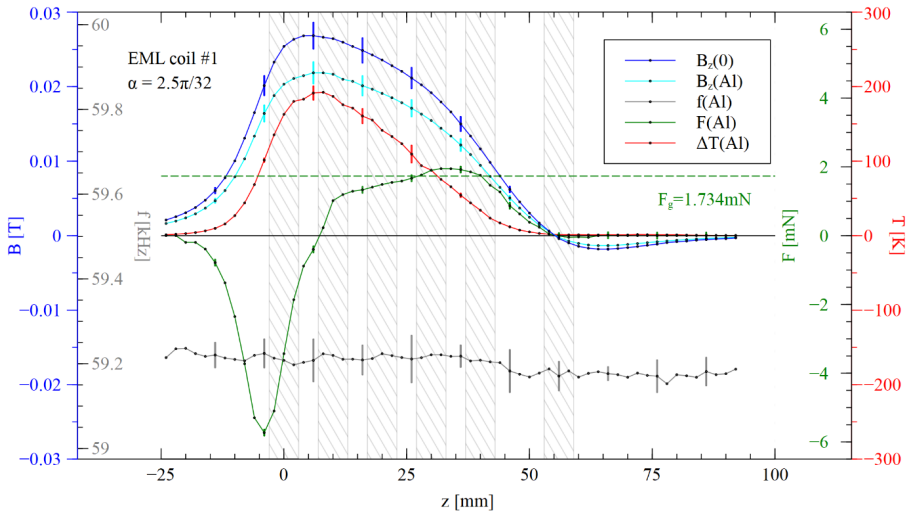

Fig. 3. Measurement results for the EML coil #1, including vertical component of magnetic field with ($B_z(0)$) and without ($B_z(Al)$) the sample, lift force acting on the sample (F(Al)), max temperature of the sample at the end of the measurement (ΔT(Al)), as well as the resonance frequency of the EML coil during the measurement (f(Al)). The grey background areas represent the position of EML coil windings. The green, horizontal, dotted line represents the weight of the sample.

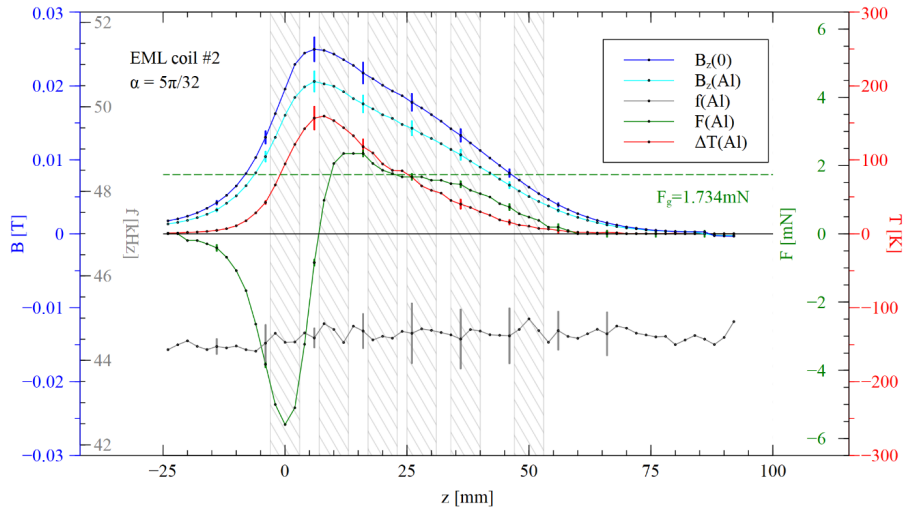

Fig. 4. Measurement results for the EML coil #2, including vertical component of magnetic field with ($B_z(0)$) and without ($B_z(Al)$) the sample, lift force acting on the sample (F(Al)), max temperature of the sample at the end of the measurement (ΔT(Al)), as well as the resonance frequency of the EML coil during the measurement (f(Al)). The grey background areas represent the position of EML coil windings. The green, horizontal, dotted line represents the weight of the sample.

Here we will attempt to graphically compare the experimental results of this study to the data available in the literature source [3]. However, first, we should discuss some caveats. Probably the most significant difference between our experiment and simulation described in the source is in the current flowing through the EML coil (850 A vs 100 A, respectively). Also, the current frequency in the simulations described in the source only went up to 35 kHz, while in our experiment it was in the range from 44 to 60 kHz. One last caveat is that the description of the EML coil geometry in the source is not exact and can be interpreted in different ways (the main problem being the total height of the coil (0.06 m) not matching the number of windings * (diameter of windings + distance between neighbouring windings) (6*(0.006+0.002) =0.048m)). It is possible that there are differences in the placement of the windings of EML coils along the vertical axis, which cause additional changes between the experimental and simulation graphs. It should also be noted that the data in the source [3] is presented as a difference between lift force and force of gravity. With that in mind, values presented in the source will be added (0.000176715 kg * 9.81 m/s^2) to add the gravity force.

A graph with comparison for the experiment and the simulation for a conical EML coil with an angle $\alpha=5\pi/32$ is shown in Fig. 5. The peak amplitude of the lift force appears to be similar for the experiment and the simulation at higher frequencies, despite different current amplitudes in EML coil. However, the position and shape of the peak is noticeably different. Also, we find it strange that simulation data appear to indicate a significant shift of lift force direction change position at a frequency of 5 kHz. Judging from the data presented in the simulation, the effect of the frequency change decreases at higher frequencies. If that is the case, the best we can currently do for comparing different coil geometries would be to use data with highest frequencies available (see Fig. 6). Both the experiment and the simulation show the trend of lift force peak position shifting downwards as the angle α is increased. However, the position where the lift force changes direction appears to be the same for different angles in the experiment, while in the simulated data that position significantly shifts downwards as the angle α is increased.

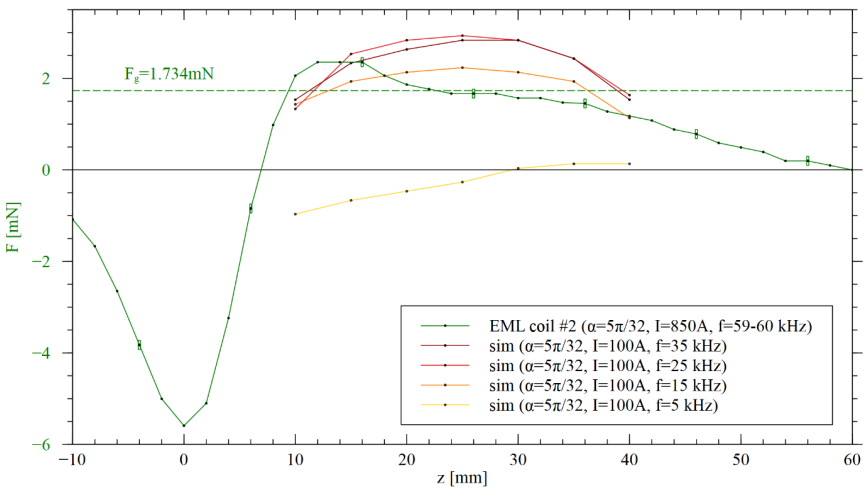

Fig. 5. Comparison between direct measurement and simulation data (as interpreted from data presented in [3]) for a conical EML coil with an angle $\alpha=5\pi/32$. The green, horizontal, dotted line represents the weight of the sample.

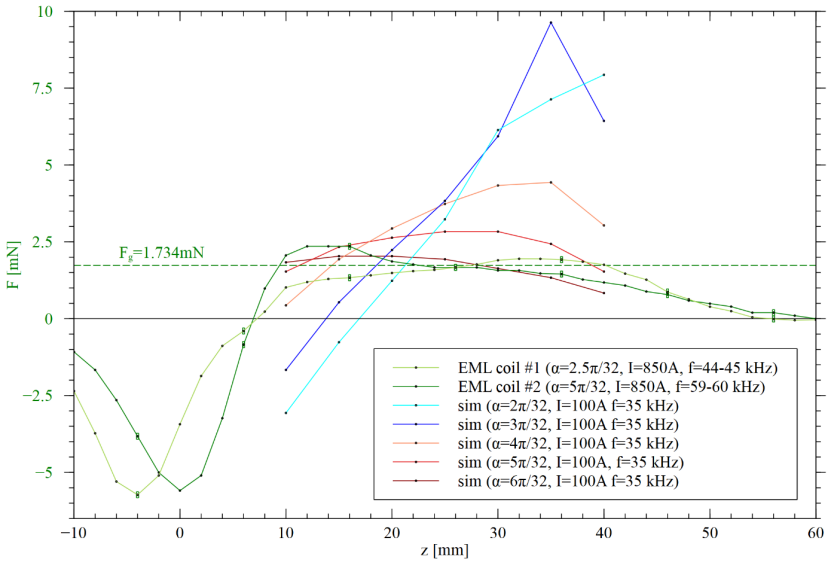

Fig. 6. Comparison between direct measurement and simulation data (as interpreted from data presented in [3]) for conical EML coils with different angles α, at high frequencies. The green, horizontal, dotted line represents the weight of the sample.

Differences in amplitude of the lift force could be easily explained by different current values in the EML coil, but differences in the shape of the curves (positions of peaks and crossing the horizontal axis) would require further investigation, preferably repeated experiment with matching current amplitude and frequency. Another potential reason for differences between simulated and measured lift force curves could be heating effects and related resistivity changes in the sample. The source defines the conductivity of the sample as a constant, but when Al sample heats up from 20 °C to 180 °C, its resistivity would be expected to go up from $2.65*10^{-8}$ Ω m to $4.46*10^{-8}$ Ω m.

4. CONCLUSION

EML is a promising technique for obtaining high purity alloys, as well as growing crystals. More sophisticated calculation and simulation methods are necessary for development and optimization of EML-based methods for different applications. High-quality experimental data can be useful for development and verification of simulation methods for EML processes. Our results provide precise and broad look at magnetic, thermal, and mechanic processes in conical EML coils. In future research, we plan to measure a wider variety of EML coil and sample geometries.

ACKNOWLEDGEMENTS

This research has been financed by the Institute of Atomic Physics and Spectroscopy of the University of Latvia within the project “Development of Next Generation

Technology for Ultra Purity Crystal Growth Based on MHD Semi Levitation" (Levitation, project No. 1.1.1.1/20/A/070) budget.

REFERENCES

1. Witteveen, J. P. (2021). *Containerless Metal Single-Crystal Growth via Electromagnetic Levitation.* PhD Thesis. Enschede: University of Twente.
2. Royer, Z. L., Tackes, C., LeSar R., & Napolitano, R. E. (2013). Coil Optimization for Electromagnetic Levitation Using a Genetic Like Algorithm. *Journal of Applied Physics, 113*, 214901.
3. Nycz, B., Malinski, Ł., & Przyłucki, R. (2021). Influence of Selected Model Parameters on the Electromagnetic Levitation Melting Efficiency. *Applied Sciences, 11*, 3827.
4. Nycz, B., Przyłucki, R., & Maliński, Ł. (2023). Comparison of characteristics for two selected inductors for levitation melting. In *Proceedings of the 14th International Conference on Measurement "Measurement 2023"*. Smolenice, Slovakia.
5. Husley, W. J. (1963). *The Design and Performance of Levitation Melting Coils.* Union Carbide Nuclear Co. Y-12 Plant, Oak Ridge, Tenn.
6. Fromm, E., & Jehn, H. (1965). Electromagnetic Forces and Power Absorption in Levitation Melting. *British Journal of Applied Physics, 16*, 653.
7. Okress, E. C., Wroughton, D. M., Comentez, G., Brace, P. H., & Kelly, J. C. R. (1952). Electromagnetic Levitation of Solid and Molten Metals. *Journal of Applied Physics, 23*, 545.
8. Witteveen, J. P., van Gastel, R., van Houselt, A., & Zandvliet, H. J. W. (2021). 3D Modeling of Electromagnetic Levitation Coils. *Current Applied Physics, 32*, 45–49.
9. Sassonker, I., & Kuperman, A. (2020). Electro-Mechanical Modeling of Electromagnetic Levitation Elting System Driven by a Series Resonant Inverter with Experimental Validation. *Energy Conversion and Management, 208*, 112578.
10. Priede, J., Baptiste, L. C. B., Gleijm, G., & van Westrum, J. A. F. M. S. (2006). *Apparatus and Method for Levitation of an Amount of Conductive Material.* World Patent WO2006021245A1, 2 March 2006.
11. Silamiķelis, V., Apsītis, A., Sniķeris, J., Pumpurs, A., & Biggs, S. (2023). Simultaneous measurement of the lifting force, joule heating and axial/radial components of EM field inside an electromagnetic levitation coil. In *Proceedings of the 14th International Conference on Measurement "Measurement 2023".* Smolenice, Slovakia.
12. Sniķeris, J., Apsītis, A., Pumpurs, A., Lācis, U., Kravchenko, S., & Silamiķelis, V. (2023). Experimental Observation of the Vertical Displacement between Heating and Levitation Regions in an Electromagnetic Levitation Coil. *J. Phys. D: Appl. Phys., 57*, 095002.

sciendo

LATVIAN JOURNAL OF PHYSICS
AND TECHNICAL SCIENCES
2024, N 4

DOI: 10.2478/lpts-2024-0031

COMPARATIVE ANALYSIS OF THERMAL CHARACTERISTICS: VIRGIN POLYACRYLONITRILE (PAN) VERSUS ELECTROSPUN PAN NANOFIBRE MATS

J. V. Sanchaniya

Institute of Mechanical and Biomedical Engineering,
Riga Technical University,
6B Kipsala Str., Riga, LV-1048, LATVIA
E-mail: jaymin.sanchaniya@rtu.lv

The utility of polymers in the fabrication of nanofibres via electrospinning is well established. Paramount to their application is understanding of their thermal properties, as these dictate not only their processability but also their mechanical robustness, stability under elevated temperatures, and suitability for intended applications. The electrospinning process, which involves heating polymers and subjecting them to high voltage, inherently modifies their thermal characteristics. This study attempts to elucidate these alterations, particularly by focusing on polyacrylonitrile (PAN) nanofibres. Employing techniques such as thermogravimetric analysis (TGA) and Differential Scanning Calorimetry (DSC), the study compares the thermal properties of electrospun PAN nanofibre mats with those of their virgin counterparts. The PAN nanofibres were synthesised by electrospinning the PAN polymer solution and collecting the resultant mat on a flat plate collector. For a comparative analysis, virgin PAN, from which nanofibres were derived, underwent identical thermal testing. The findings reveal a reduction in the glass transition temperature of PAN nanofibres by approximately 3–5 % compared to virgin PAN. In addition, a significant reduction in heat capacity of about 42 % was observed in the nanofibres. Additionally, the TGA results indicated solvent evaporation at approximately 110 °C. Therefore, this investigation sheds light on the nuanced alterations in the thermal characteristics of PAN nanofibre mats as a result of the electrospinning process, providing vital insights for their application in various thermal management scenarios.

Keywords*: Electrospinning, differential scanning calorimetry (DSC), nanofibres, PAN (polyacrylonitrile), thermogravimetric analysis (TGA).*

1. INTRODUCTION

Electrospinning emerges as a pivotal technique in the nanofibre fabrication landscape, particularly in the context of nanofibre applications [1]. This process enables the production of nanofibres with superior physical attributes. It involves subjecting a polymer solution or melt to a high voltage, engendering the formation of an electrically charged jet. This jet, under the influence of the electric field, travels towards a collector, where it solidifies into a fibrous mat or film. In particular, the electrospinning process is known to induce modifications in the thermal properties of the polymer, such as alterations in its melting point, glass transition temperature, and thermal conductivity [2].

Electrospun polyacrylonitrile (PAN) nanofibers are utilised in a wide range of applications, for example, air & water filtration [3]–[5], drug delivery [6]–[8], wound dressing [9], nanocomposite fabrication [10]–[12], antibacterial textiles [13]–[15] integrated with silica dioxide and succinite (Baltic amber), and the creation of protective clothing [16]. Given these applications, the nanofibres are often subjected to thermal stresses, underscoring the necessity to understand their thermal stability when exposed to heat.

Thermogravimetric analysis (TGA) is instrumental in this study as it measures the change in mass of a sample over time as a function of temperature, offering insights into physical phenomena such as phase transitions, which typically encompass transitions between solid, liquid, and gaseous states, as well as absorption, desorption, and chemical phenomena like thermal decomposition reactions. Complementarily, differential scanning calorimetry (DSC) is employed to ascertain the crystallisation and glass transition temperatures of the polymers.

The objective of this study is to perform a comparative analysis of the thermal characteristics of virgin PAN and PAN nanofibres. Using TGA and DSC analyses, a comprehensive understanding of how electrospinning influences the thermal properties of PAN is sought, thereby contributing valuable insights into the field of polymer science and nanotechnology.

2. MATERIALS AND METHODOLOGY

This study meticulously examines the thermal characteristics of virgin polyacrylonitrile (PAN) and electrospun PAN nanofibres that are produced as previously mentioned by the authors [11], [17], [18]. The materials used for the synthesis of these nanofibres comprised PAN powder and N, N-dimethylformamide (DMF). Specifically, polyacrylonitrile (average molecular weight: 150,000 (MW); CAS number: 25014-41-9) and N, N-dimethylformamide (ACS reagent quality, 99.8% purity; CAS number: 68-12-2) were procured from Sigma-Aldrich Chemicals, Merck KGaA, Darmstadt, Germany.

For thermogravimetric analysis (TGA), a TG 209 F1 Libra® thermomicrobalance (NETZSCH, Selb, Germany) was used. The samples, each weighing between 5 and 6 mg, were placed in crucibles of aluminium oxide (Al2O3). The temperature was gradually increased from 20 °C to 800 °C at a rate of 10 °C / min, in an inert nitrogen atmosphere with a flow rate of 30 ml / min.

Differential scanning calorimetry (DSC) was performed using a DSC 214 Polyma differential scanning calorimeter (NETZSCH, Selb, Germany), also under a nitrogen atmosphere with an identical flow rate. The DSC involved the precise placement of the virgin PAN powder and the PAN nanofibre mat in the crucible. The thermal cycle began with an initial heating from -50 °C to 150 °C, aimed at expelling impurities and moisture. This was followed by cooling to -50 °C and a subsequent reheating to 150 °C to determine the glass transition temperature. Each heating and cooling cycle was interspersed with an isothermal step.

The DSC protocol adhered to ASTM E1356 standards. The heating rate was maintained at 10 °C / min in a range of -50 °C to 150 °C, in accordance with methodologies previously described by the authors in [17]. To verify the weight of the samples, a KERN ABT 5NM laboratory scale (KERN&Sohn GmbH, Balingen, Germany) was used. This scale, with a maximum capacity of 100 g and a discreteness of 0.000001 g, bears the serial number WB22G0101 and was calibrated according to the certificate number B61-389-2023-03/1, dated 24 March 2023.

This methodology provides a comprehensive framework for assessing the thermal properties of both virgin and electrospun PAN, thereby facilitating a thorough comparative analysis.

3. RESULTS AND DISCUSSION

The thermal behaviour of virgin polyacrylonitrile (PAN) and PAN nanofibres was investigated using TGA and DSC.

The TGA curve for virgin PAN (Fig. 1) comprises a green graph representing mass loss as a function of temperature and a red graph depicting the first derivative, which aids in precise temperature determination. In particular, up to 289.5 °C, no significant mass loss was observed in the virgin PAN. The onset of degradation was marked at 291.6 °C. The total mass loss from 25 °C to 299.8 °C was 14.15 % and from 299.8 °C to 374.4 °C, it was 22.78 %. Subsequently, a mass loss of 19.70 % was recorded from 374.4 °C to 566.0 °C, followed by a loss of 3.65 % from 566.0 to 799.6 °C. At 800 °C, the residual mass was recorded as 39.42 %.

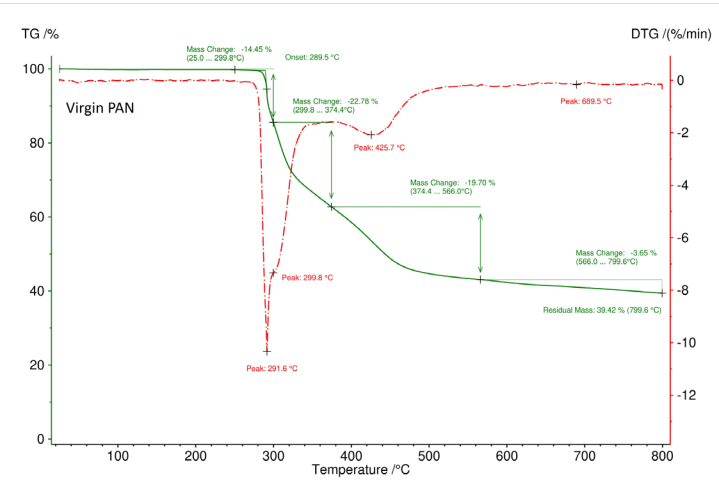

Fig. 1. TGA and DTG of virgin PAN.

The TGA curve of PAN nanofibres (Fig. 2) showed an initial mass loss at 110.6 °C, approximately 3.08 %, attributed to the evaporation of the solvent DMF. The total mass loss from 25.0 °C to 158.7 °C was 3.08 %, and from 158.7 °C to 297.6 °C it was 1.66 %. In the temperature range of 264.2 °C to 297.6 °C, the mass loss was 14.26 %. From 297.1 °C to 371.6 °C, the loss was around 22.96 %, and from 371.6 °C to 552.0 °C it was 20.23 %. In the range of 551.3 °C to 799.5 °C, the mass loss was 5.61 %, leaving a residual mass of 32.63 %.

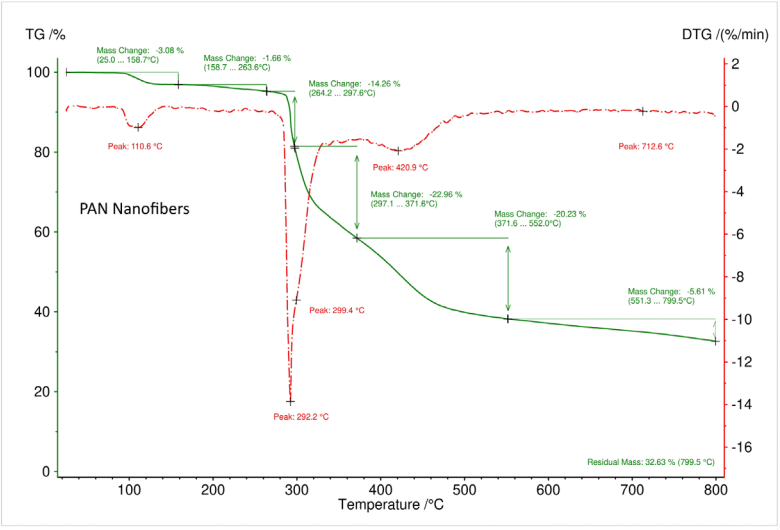

Fig. 2. TGA and DTG of PAN nanofibre mat.

During the first heating cycle in DSC (Fig. 3), virgin PAN absorbed 30.06 J / g, while PAN nanofibres absorbed 26.88 J/g. Two peaks were observed in the heat absorption profile, potentially due to solvent evaporation, corroborating the temperature range observed in the TGA graph of the PAN nanofibre mat (Fig. 2).

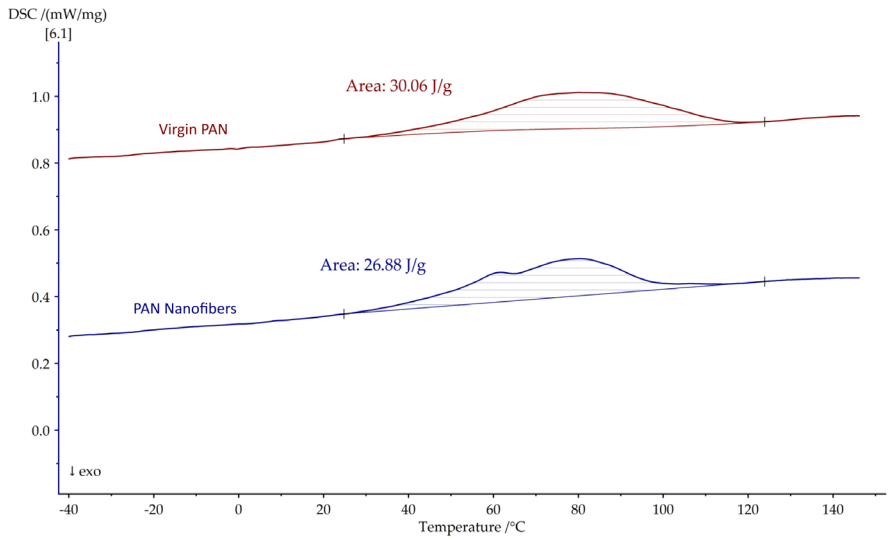

Fig. 3. The 1st heating cycle of virgin PAN vs PAN nanofibres in DSC.

In the first cooling cycle, represented in Fig. 4, the glass transition temperature for virgin PAN was observed at 97.9 °C, while for PAN nanofibres, it was 94.9 °C, indicating a reduction of approximately 3 %.

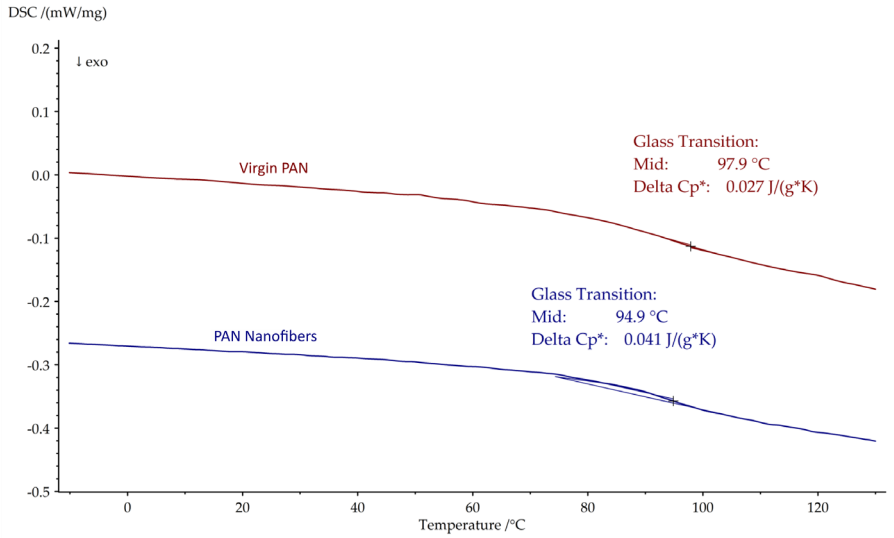

Fig. 4. The 1st cooling cycle of virgin PAN vs PAN nanofibres in DSC.

The second heating cycle of DSC (Fig. 5) revealed a glass transition temperature of 101.8 °C for virgin PAN and approximately 96.0 °C for PAN nanofibres, a reduction of about 5 %. The change in heat capacity (Delta Cp*) showed a notable difference: for virgin PAN, it was 0.202 J / (gK), while for the PAN nanofibres, it was 0.116 J/(gK), marking a reduction of 42 %.

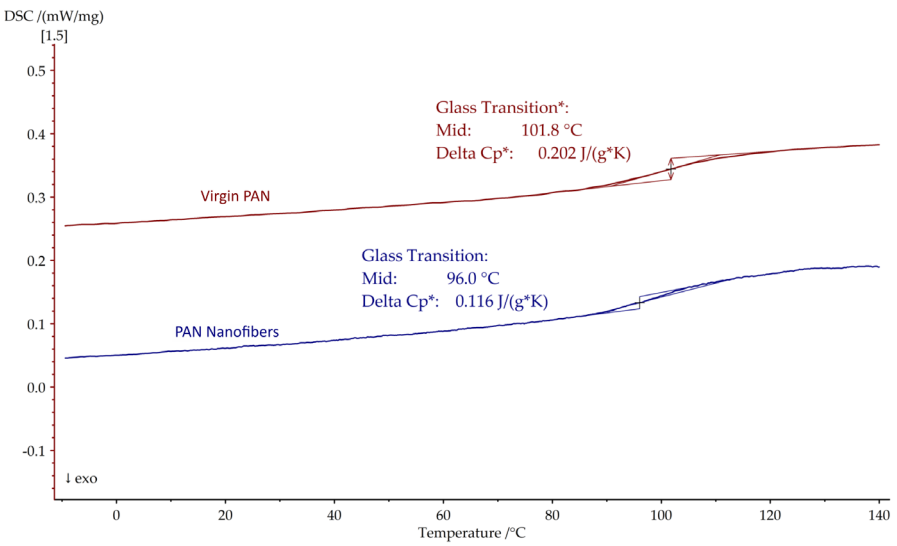

Fig. 5. The second heating cycle of virgin PAN vs PAN nanofibres in DSC.

These results collectively offer a comprehensive insight into the thermal characteristics of virgin PAN and PAN nanofibres, highlighting the impact of the electrospin-

ning process on their thermal stability and transition temperatures.

The comparative analysis of the thermal properties of virgin polyacrylonitrile (PAN) nanofibres and electrospun PAN nanofibres, as elucidated by TGA and DSC, reveals significant insights. The electrospinning process evidently impacts the thermal stability and transition temperatures of PAN. The increased glass transition temperature in the nanofibre mats, as compared to those of virgin PAN, suggests enhanced thermal stability, possibly attributable to the morphological changes induced by electrospinning. The observed decrease in melting temperature and the reduced heat capacity in nanofibres indicate alterations in the crystalline structure and thermal behaviour, which was observed in the case of polyamide nanofibres [19]. These changes have profound implications for the application of PAN nanofibres in areas that require thermal resilience. The early onset of solvent evaporation in nanofibres, as detected in TGA, further underscores the influence of processing methods on the properties of the materials. Overall, the findings underscore the necessity of considering these thermal characteristic variations when employing PAN nanofibres in practical applications, particularly those subjected to thermal stress.

4. CONCLUSIONS

This investigation has comprehensively analysed the thermal characteristics of virgin PAN and electrospun PAN nanofibres, using thermogravimetric analysis and Differential Scanning Calorimetry. The results indicate significant alterations in the thermal properties as a result of the electrospinning process. The glass transition temperature in the PAN nanofibres showed a reduction of approximately 3–5 % compared to virgin PAN, suggesting a decrease in thermal stability. The melting temperature and heat capacity also showed notable changes, with the heat capacity experiencing a 42 % reduction in the nanofibres. These variations in thermal properties, including the early onset of solvent evaporation in nanofibres, underscore the impact of electrospinning on the thermal behaviour. These findings are vital for applications where PAN nanofibres are exposed to thermal conditions, informing material selection and processing techniques in industries such as filtration, drug delivery, and protective clothing.

ACKNOWLEDGEMENTS

The research/publication has been supported by the Doctoral Grant programme of Riga Technical University.

REFERENCES

1. Trabelsi, M., Mamun, A., Klocker, M., Brockhagen, B., Kinzel, F., Kapanadze, D., & Sabantina, L. (2021). Polyacrylonitrile (PAN) Nanofiber Mats for Mushroom Mycelium Growth Investigations and Formation of Mycelium-Reinforced Nanocomposites. *J. Eng. Fiber. Fabr.*, *16*. doi: 10.1177/15589250211037982.

2. Xue, J., Wu, T., Dai, Y., & Xia, Y. (2019). Electrospinning and Electrospun Nanofibers: Methods, Materials, and Applications. *Chemical Reviews*, *119* (8), 5298–5415. doi: 10.1021/acs.chemrev.8b00593.
3. Liao, Y., Loh, C. H., Tian, M., Wang, R., & Fane, A. G. (2018). Progress in Electrospun Polymeric Nanofibrous Membranes for Water Treatment: Fabrication, Modification and Applications. *Prog. Polym. Sci.*, *77*, 69–94. doi: 10.1016/j.progpolymsci.2017.10.003.
4. Zhou, Y., Liu, Y., Zhang, M., Feng, Z., Yu, D. G., & Wang, K. (2022). Electrospun Nanofiber Membranes for Air Filtration: A Review. *Nanomaterials*, *12* (7). doi: 10.3390/nano12071077.
5. Zhang, W., He, Z., Han, Y., Jiang, Q., Zhan, C., Zhang, K., … & Zhang, R. (2020). Structural Design and Environmental Applications of Electrospun Nanofibers. *Compos. Part A Appl. Sci. Manuf.*, *137*, 106009. doi: 10.1016/j.compositesa.2020.106009.
6. Liang, D., Hsiao, B. S., & Chu, B. (2007). Functional Electrospun Nanofibrous Scaffolds for Biomedical Applications. *Adv. Drug Deliv. Rev.*, *59* (14), 1392–1412. doi: 10.1016/j.addr.2007.04.021.
7. Arun, A., Malrautu, P., Laha, A., & Ramakrishna, S. (2021). Gelatin Nanofibers in Drug Delivery Systems and Tissue Engineering. *Eng. Sci.*, *16*, 71–81. doi: 10.30919/es8d527.
8. Duan, X., Chen, H. L., & Guo, C. (2022). Polymeric Nanofibers for Drug Delivery Applications: A Recent Review. *J. Mater. Sci. Mater. Med.*, *33* (12). doi: 10.1007/s10856-022-06700-4.
9. Vargas, E. A. T., do Vale Baracho, N. C., de Brito, J., & de Queiroz, A. A. A. (2010). Hyperbranched polyglycerol electrospun nanofibers for wound dressing applications. *Acta Biomater.*, *6* (3), 1069–1078. doi: 10.1016/j.actbio.2009.09.018.
10. Sanchaniya, J. V., Lasenko, I., Vijayan, V., Smogor, H., Gobins, V., Kobeissi, A., & Goljandin, D. (2024). A Novel Method to Enhance the Mechanical Properties of Polyacrylonitrile Nanofiber Mats: An Experimental and Numerical Investigation. *Polymers, 16* (7), 992. https://doi.org/10.3390/polym16070992.
11. Sanchaniya, J. V., Lasenko, I., Kanukuntla, S. P., Mannodi, A., Viluma-Gudmona, A., & Gobins, V. (2023). Preparation and Characterization of Non-Crimping Laminated Textile Composites Reinforced with Electrospun Nanofibers. *Nanomaterials*, *13* (13), 1949. doi: 10.3390/nano13131949.
12. Sanchaniya, J. V., Kanukuntla, S. P., & Senyurt, K. B. (2023). Fabrication and Mechanical Properties of Polymer Composte Nanofiber Mats. *Eng. Rural Dev.*, 85–90. doi: 10.22616/ERDev.2023.22.TF014.
13. Grauda, D., Butkauskas, D., Vyšniauskienė, R., Rančelienė, V., Krasņevska, N., Miķelsone, A., … & Ļašenko, I. (2023). Establishment of Biotesting System to Study Features of Innovative Multifunctional Biotextile. *Proc. Latv. Acad. Sci. Sect. B Nat. Exact, Appl. Sci.*, *77* (3–4), 86–192. doi: 10.2478/prolas-2023-0026.
14. Asfand, N., & Daukantiene, V. (2023). Study of the Tensile and Bending Stiffness Behavior of Antistatic and Antibacterial Knitted Fabrics. *Fibres Text. East. Eur.*, *31* (3), 1–9. doi: 10.2478/ftee-2023-0026.
15. Sanchaniya, J.-V., Kanukuntla, S.-P., Modappathi, P., & Macanovskis, A. (2022). Mechanical Behaviour Numerical Investigation of Composite Structure, Consisting of Polymeric Nanocomposite Mat and Textile. *21st Int. Sci. Conf. Eng. Rural Dev. Proc.*, *21*, 720–726. doi: 10.22616/erdev.2022.21.tf225.
16. Gorji, M., Bagherzadeh, R., & Fashandi, H. (2017). 21 - Electrospun Nanofibers in Protective Clothing. *Woodhead Publishing Series in Textiles, Electrospun Nanofibers*, 571–598. doi: 10.1016/B978-0-08-100907-9.00021-0.
17. Sanchaniya, J. V., Lasenko, I., Kanukuntala, S. P., Smogor, H.,Viluma-Gudmona, A., Krasnikovs, A., … & Gobins, V. (2023). Mechanical and Thermal Characteristics of Annealed-Oriented PAN Nanofibers. *Polymers (Basel)*, *15* (15), 3287. doi: doi.org/10.3390/polym15153287.

18. Sanchaniya, J. V., Lasenko, I., Gobins, V., & Kobeissi, A. (2024). A Finite Element Method for Determining the Mechanical Properties of Electrospun Nanofibrous Mats. *Polym.*, *16* (6), 852. doi: 10.3390/polym16060852.

19. Kanukuntla, S., Sanchaniya, J., & Beresnevics, V. (2023). Comparative DSC Analysis of Virgin and Nanofiber Mats of PA6. *Engineering for Rural Development, 6*, 539–543. doi: 10.22616/ERDev.2023.22.TF113.